IJBBE International Journal of
Biophotonics & Biomedical Engineering Vol. 4, No. 1, Spring-Summer, 2024

Review Article

Recent advances in ISFET-based biosensors for the detection of biomarkers: History, principles, gate structure and applications

Seyed Saman Nemati [a], Gholamreza Dehghan [b*], Yaser Abdi [b], Sohrab Ahmadi-Kandjani [c,d]

a Department of Biology, Faculty of Natural Sciences, University of Tabriz, 51666−16471 Tabriz, Iran
b Nanophysics Research Laboratory, Department of Physics, University of Tehran, 1439955961 Tehran, Iran
c Research Institute for Applied Physics and Astronomy (RIAPA), University of Tabriz, Tabriz, Iran
d Faculty of Physics, University of Tabriz, Tabriz, 51663-165, Iran

***Corresponding Author Email: gdehghan@tabrizu.ac.ir**

DOI: 10.71498/ijbbe.2024.976364

ABSTRACT

Received: Jun. 2, 2024, Revised: Aug. 6, 2024, Accepted: Nov. 28, 2024, Available Online: Jan. 5, 2025

Using ion-sensitive field effect transistor (ISFET) sensors is one of the most prominent signal detection and measurement methods for various analytes and biomarkers. Here the history of the ISFET sensors and their general operations are reviewed. Because of the extreme importance of gate performance and structure in sensitivity, price, reusability, durability, and stability of ISFET sensors, the gate materials and structures have been the subject of many studies. In addition, the importance of gate materials in ISFET sensor readout methods is reviewed here. The applications of ISFET as super biosensors with high sensitivity, easy manufacturing methods, sufficient stability, and cost-effectiveness in measuring ions, DNA, biomarkers, and analytes based on enzyme activity, are highlighted. Finally, the importance and advantage of using ISFET sensors with bioactive nanomaterial layers are emphasized, and future studies of these sensors, based on our point of view, are discussed.

KEYWORDS

ISFET sensor; Gate materials; Biosensor; Enzymatic ISFET assay.

ABTS	2, 2-azino-bis 3-ethylbenzothiazoline-6-sulphonic acid
ABTES	3-aminopropyltriethoxysilane
AChE	Acetylcholinesterase
BSA	Bovine serum albumin
API	Active pharmaceutical ingredients
Cpy	Chlorpyrifos
CMOS	Complementary metal-oxide semiconductor
CVCC	Constant-Voltage, Constant-Current
C-PPy	Carboxylated polypyrrole
DG	Double-gate
DG-CNT-ISFET	Dual-gate carbon nanotube ISFET
DNA	Deoxyribonucleic acid

EG-ISFET	Extended-gate ISFET
ENFET	Enzyme based ISFETs
FET	Field effect transistor
F-rGO	Fluorinated-reduced graphene oxide
I_{DS}	Drain-source current
ITO	Indium tin oxide
ISFET	Ion-sensitive field effect transistor
IUPAC	International Union of Pure and Applied Chemistry
GFET	Graphene field effect transistors
HLA	Human leukocyte antigen
HRP	Horseradish peroxidase
JFET	Junction FET
JF-ED-TFET	Junction-free tunneling field-effect-based biosensor
MHC	Major histocompatibility complex
MESFET	Metal-semiconductor FET
MOSFET	Metal- oxide-semiconductor FET
MICA	MHC associated with class I related chain A
LAMP	Loop-mediated isothermal amplification
LOD	Limit of detection
PBSE	1-pyrenebutanoic acid succinimidyl ester
rCV-N	Recombinant cyanovirin-N
SOI-DG ISFET	Silicon-on-insulator dual-gate ISFET
Si NW	Silicon nanowire
SGGT	Solution-gated graphene transistors
V_{DS}	Drain-source voltage
UT	Ultrathin body

I. INTRODUCTION

Ultra-sensitive biosensors equipped with nanotechnology have the potential for early and accurate medical and genetic diagnosis. With the development of different sensory methods, academic researchers have become interested in this topic. Precision biosensing tools and test strips are improving and transitioning from optical and/or electrochemical to electronic technologies [1, 2]. Thus, those interested in biosensors must investigate the structure, performance, and recent applications of electronic-based biosensors because they have the potential to become one of the main sensor technologies for medical diagnosis applications.

According to the International Union of Pure and Applied Chemistry (IUPAC) definition, biosensors use specific biochemical reactions mediated by the immune system, isolated enzymes, tissues, whole cells, or organelles to detect chemical compounds by optical, electrical or thermal signals [3]. Thus, biosensors are analytical tools for monitoring biological dynamics, interactions, and activities [4]. A biosensor consists of three main parts, including a bio-detection element, a transducer, and a signal processing unit. Biomolecules cause changes in physical quantities such as charge, photon, or mass, and the transducer senses these changes converting them into electrical signals, voltage or current. Ultimately, to determine the sensing results, the signals are amplified and analyzed.

According to different output signals, the traditional methods of monitoring the electrochemical reactions are divided into optical [5-7] and classical three-electrode systems [8]. The optical method is based on light changes during electrochemical reactions (Fig. **1**) [9-11]. One of the disadvantages of this method is the need for a complex, expensive, and large device to achieve high sensitivity [12]. In contrast, the classical three-electrode system has advantages such as high sensitivity and low production cost (Fig. **1**). However, the mass production of a three-electrode system and its integration into other systems is challenging due to the lack of a common production standard [13]. To overcome this challenge, the ion-sensitive field-effect transistor (ISFET) was developed in 1970 [14].

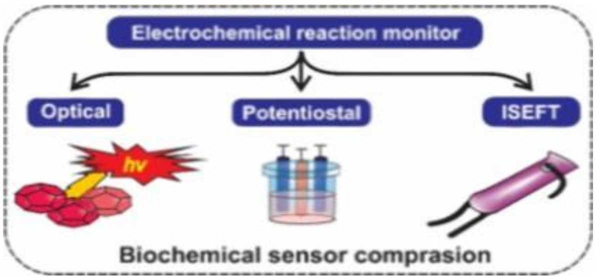

Fig. 1 Classification of conventional electrochemical sensors.

In biosensing mechanisms, an interesting approach, namely field effect transistor (FET)-based biosensor was considered a reliable approach. In addition, due to the rapid development of solid-state technologies there are many options to move forward. Most biomolecules carry electrostatic charges and bioactivities involving changes in electrical potential. Thus, FET-based biosensors are a suitable option for fast and ultra-sensitive detection of biomarkers [15]. ISFET biosensors are FET-type biosensors, which measure ions concentration in solutions. In the ISFET the solution is used as the gate electrode and the other parts follow the conventional FET devices. The change in concentration of an ion such as H^+ accordingly changes the current through the FET. ISFET biosensors are extremely sensitive and have the advantage of good scalability, intrinsic amplification, acid-alkali resistance, water repellent, impact resistant, fast real-time detection, direct electrical readout, and lower power requirements compared to other electrochemical and optical sensing devices. Furthermore, they are superior to cyclic process voltmeters with simple direct electrical readout and complementary metal-oxide semiconductor (CMOS) compatibility [16-18].

The use of ISFETs in DNA sensing has been specifically discussed in the review articles [19, 20]. ISFET applications in medicine have also been reviewed [21]. In the review article by *Cao et al.*, many topics of ISFET and its applications in biosensors have been covered, but the materials used in the gate terminal structure have not been investigated specifically [13]. Therefore, in this review, first, a brief history of ISFET sensor performance in general is presented and the manufacturing and improvement of ISFET sensor performance is discussed. Then, there is more focus on the materials and gate structure of ISFET sensors as their most sensitive and key part. Also, readout methods of ISFET sensors and their application as biosensors will be discussed. So, the main purpose of this review, in addition to reviewing recent research, is to create a proper background of the entire ISFET structure and performance, focusing more on the biosensing application of ISFET.

II. HISTORY OF ISFET SENSORS

The ISFET sensors consist of a sensing element and a transducer. All stages of development and improvement of ISFET devices and their sensing applications are presented in

Table 1. In recent decades the progress in the use of ISFET as sensors have been impressive and have become the favorite biosensors for biochemists. Advances have been made to the extent that a multifunctional sensor could be used to measure several analytes [22]. A schematic of sensors with multiplex functions is shown in **Error! Reference source not found.**

TABLE 1. TIMELINE OF PROGRESS IN THE CONSTRUCTION AND OPTIMIZATION OF ISFET BIOSENSORS

	Advanced process in ISFET	**Year**	**Ref.**
1	ISFET originated from FET[a].	1925	[23]
2	Suggesting different types of FET depending on the type of gate structure (such as JEFT[b] and MESFET[c]).	1952	[24]
3	Using a semiconductor process, the MOSFET[d] uses a metal-semiconductor junction to replace the p-n junction of the JFET for easier fabrication and higher operating speed.	1960	[25]
4	Despite the low speed and ease of damage, the MOSFET was used as a low-cost signal converter with easy fabrication on a large scale.	1962	[26]
5	Quantitative detection of Na^+ with source-drain current output (I_{DS}) as the first ISFET sensor with direct oxide-solution contact by removing the metal gate structure MOS.	1970	[14]
6	Replacing metal oxides in MOSFET with an aqueous solution in ISFET.	1972	[27]
7	Using an ISFET with a gate made of noble metal as a gas sensor.	1975	[28]
8	Application of ISFET to identify penicillin biomolecules through enzymatic reactions.	1980	[29]
9	Placement of sensing films instead of metals in the structure of MOS and its explanation by the *Bousse* site dissociation model.	1983	[30]
10	Optimizing the size of the sensors by making a miniaturized urea biosensor using an enzyme on the ISFET gate.	1984	[31]
11	Improving the anti-interference performance of ISFT-based biosensors for simultaneous detection of urea and glucose	1985	[32]
12	Detection with acceptable sensitivity of H^+, by the structure of ISFET containing different sensitive films (such as Ta_2O_5, Si_3N_4, Al_2O_3) on the insulating oxide layer.	1987	[33]
13	Detection of urea in human blood serum using GATE enzymatic modification in ISFET.	1995	[34]
14	ISFET sensor development is based on clinical applications focused on the detection of antibodies, glucose, DNA, and cells.	2001	[35]

a Field effect transistor; b, junction FET; c, Metal-semiconductor FET; d, Metal- oxide-semiconductor FET.

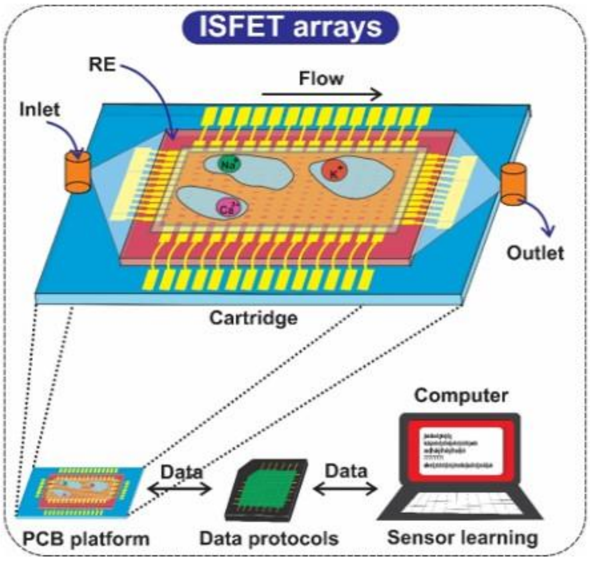

Fig. **2** Schematic of the ISFET arrays application for multiple detections.

III. PRINCIPLES OF ISFET SENSORS ACTION

The ISFET results from replacing the gate electrode with a solution, a chemically sensitive membrane, and a reference electrode in a conventional metal oxide silicon field effect transistor (MOSFET) (Figure 3A-C). The channel resistance in ISFET depends on the electric field perpendicular to the current direction (same as MOSFET). Charges in solution are held on the top of an insulating ion-sensitive membrane. The dependence of the surface potential on the charge concentration is explained by the well-known site-binding theory [36].

Anisotropic ion accumulation occurs at the interface between an electrochemically active surface and a liquid electrolyte (Figure 3D). Due to the differences in the amount and charge, an electric double layer will be formed by the ions near the surface, and a diffuse layer of external charges will result between the neutral volume of the solution and the Helmholtz planes, according to the Gouy – Chapman theory [37]. When SiO2 is used as an insulator, the surface of the gate oxide contains activated –OH, which is in electrochemical equilibrium with the ions in the solution (OH- and H+). Hydroxyl groups are protonated or deprotonated on the gate oxide surface. As a result, due to the contact of the gate oxide with the aqueous solution the change in pH causes a change in the potential of the SiO2 surface. Signal transmission is considered a function of the ionization state of the SiOH groups of the amphoteric surface [38]:

$$SiOH \leftrightarrow SiO^- + H^+$$

$$SiOH + H^+ \leftrightarrow SiOH_2^+$$

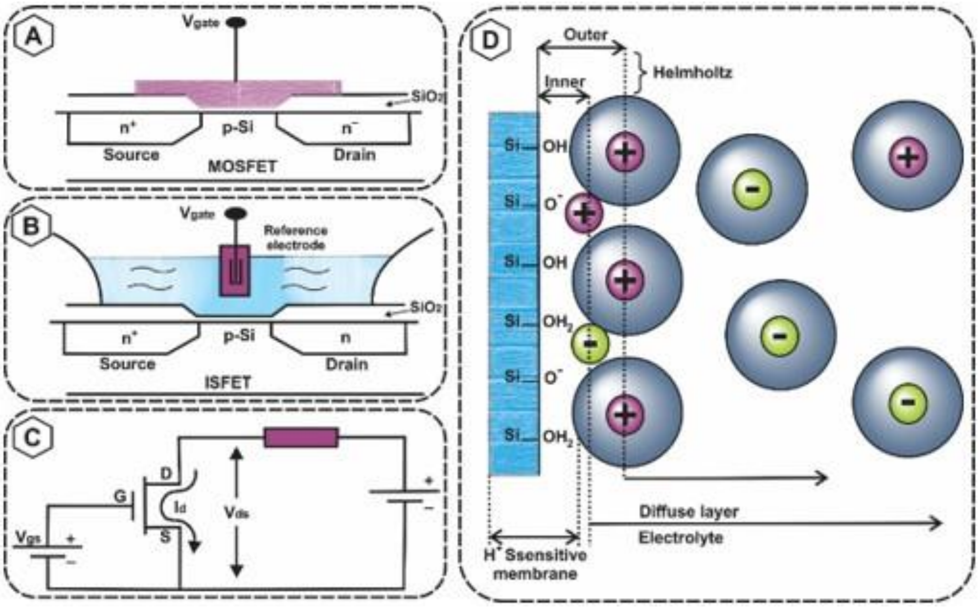

Fig. **3** (A) Basic structure of metal-oxide-semiconductor field effect transistor (MOSFET); (B) Basic structure of ion-sensitive field effect transistor (ISFET); (C) Simple circuit of an ISFET sensing system; and (D) Electrical double layer adjacent to the SiO2 surface.

The selectivity and chemical sensitivity of the ISFET sensors depend on the insulating properties of the insulator and/or electrolyte interface. In this regard, oxide coating minerals such as SiO2, Si3N4, Al2O3, or Ta2O5 can be used to obtain the desired pH response [39] (Table 2).

TABLE 2. EXAMPLES OF PH SENSOR SPECIFICATIONS.

Sensitive layer	**pH range**	**Sensitivity (mV/pH)**
Ta_2O_5	2 – 12	56 – 58
Si_3N_4	2 – 12	53 – 55
Al_2O_3	2 – 12	54 – 56

The protonation/deprotonation of the gate is controlled by the pH in the gate region [40]. Sensor responses are according to Nernst's law (59.2 mV/pH). The response of an ion-selective electrode is given by:

$$E = E_0 + \left(\frac{RT}{zF}\right) \ln[i]$$

where E is measured potential (V); E0 is characteristic constant for the ion-selective/external electrode system; T is temperature (K); R is gas constant; F is Faraday's constant; [i] is molar concentration of free unmixed ionic species; and z is the signed ionic charge [41].

IV. GATE MATERIALS IN ISFET SENSORS

The ISFET sensor’s gate material is a sensitive layer in direct contact with the target solution, forming the gate dielectric/insulator layer. In ISFET sensors, the control of the drain-source current is done through the gate potential generated at the interface between the sensor membrane and the solution. In choosing the right gate material for ISFET sensors, which is stable and performs well, more attention should be given to the high energy band gap, more connection sites for modification, and high dielectric properties [42]. To measure mineral ions, sensitive membranes are deposited on the gate layer, and other macromolecules are detected by adding a specific amount of antibody/enzyme/RNA to a specific reaction. The change in the analyte concentration is reflected by the change in the proton concentration of the environment [43].

After replacing the metal gate in the MOSFET with an aqueous solution to construct an ISFET sensor, various materials have been used in the construction of the ISFET gate [27]. Oxides have always played the role of coloring [44, 45]. The oxides are based on the effect of H+ released from the solution’s dynamic in the pH of the well, which changes the surface potential of the oxide layer as well as the potential between the gate and the base of the underlying field effect. Apart from oxides, other materials act as selective membranes for ions, which are explained in Table 3. Due to the importance of the gate material in ISFET sensor’s function, they will be further discussed and the latest developments in the field will be reviewed next.

TABLE 3. DIFFERENT MATERIALS AS GATE-SENSITIVE LAYERS.

	Thin film
SiO_2	Single-layer SiO_2 stacked with other thin layers, such as $SiO_2/HfO_2/Al_2O_3$, has improved performance [46]. First, $Al/SiO_2/Si$ layers were used as hepatitis B antigen sensors [47].

Ta_2O_5	In 1981, Ta_2O_5 was one of the most suitable materials known as a gate layer for pH sensing [47]. In 1989, the first gate Ta_2O_5 ISFET sensor with a differential amplifier was built. The output of one amplifier was amplified with a Ta_2O_5/SiO_2 ISFET gate, while the output of the other amplifier was amplified with a $SiO_xN_y/Si_3N_4/SiO_2$ ISFET gate. [47]. In this system, an external reference electrode was not required.
Nitrides	Nitride is used to measure many biomarkers. For example, in addition to being watertight, Si_3N_4 has excellent chemical stability for sensing H^+. With an ion-sensitive layer on top of the Si_3N_4 gate in the ISFET, it measures a variety of biomarkers [13]. Indium Nitride (InN) has enabled the high sensitivity of pH measurement. Accumulation of surface electrons in InN results in a large ion-induced surface potential to drive current in the ultrathin conducting channel, and as a result, sufficient gate bias in the electrolyte modulates the electron density in the ultrathin conducting channel, and the ratio of current changes increases significantly [48]. Gallium nitride (GaN) is engineered with the advantage of a wide energy gap through anisotropy design. It has high conductivity at zero discharge valve voltage and thus high sensitivity [49].
Al_2O_3	Al_2O_3 was first used in 1979 as a chemically stable assay in pH measurement [50]. In contrast to commercial FETs, in the case of this Al_2O_3 ISFET, the pH sensitivity for small sensing areas (about 0.1 mm^2), is not affected and thus the analysis of integrated samples is possible [51]. Other Al-based materials have also been used as ISFET gates, such as aluminum metal and aluminum nitride [52, 53].
Other oxides	Zinc oxide (ZnO), hafnium oxide (HfO_2), palladium oxide (PdO), and many composite oxides are attractive ion-sensitive membranes. ZnO can achieve a wide range of pH sensing with linear response, and the HfO_2 gate deposited by ALD can minimize the oxygen vacancies to reduce the bound ions on the sensor film surface. Indium-gallium-zinc-oxide thin film for n-type gate material and pH sensing membrane simultaneously provided a flexible sensor based on an oxide film prepared with a temperature sensor for real-time measurements to provide an integrated and flexible personalized bioelectronic pathway [54]. Indium zinc oxide ($InZn_xO_y$) can be used to measure pH [55].
Polymers	Polymer/organic gates broaden the variety of target analytes with ISFET sensors, such as modifying polyaniline protonated with dinonylnaphthalene sulfonic acid (PANI/DNNSA) as gate material for an ISFET polyethyleneimine sensor [56].
Two-dimensional materials	
Graphene	Graphene has higher carrier mobility than silicon at room temperature and more electron mobility with temperature change [57]. Due to its high sensitivity to surface charge and strong interaction with ionic adsorbates, it can act as an excellent material for electron-proton conversions. It has been used in the detection of Na^+, Co^{2+}, Al^{3+}, and others in ISFET sensors [43].
MoS_2	In 2011, a transistor was made with a molybdenum sulfide (MoS_2, 0.65 nm thick) sheet [58]. ISFET with MoS_2 gate has been used to measure glucose [59], hydrogen peroxide [60], heavy metal ions [61], and proteins [60].
Black phosphorus	Black phosphorus is a layered semiconductor with high carrier mobility and controllable bandgap for the design of nanoscale transistors for the detection of nitrogen dioxide gas, heavy metal ions, and immune proteins [62-64].
Metal carbides, nitrides, and carbonitrides	Two-dimensional carbonitrides, transition metal carbides and nitrides (Mxenes) are graphene-like structures composed of transition metal carbides, nitrides, or carbonitrides that have high conductivity and much low resistance. They have been used in biosensors

	since 2011 [65]. For example, they have been used to detect dopamine [66], metal ions [67, 68], and COVID-19 [69].
Other nanostructures	
Si nanowires	Si nanowire-based ISFETs with a high surface-to-volume ratio increase the threshold voltage and gate capacitance, resulting in excellent ion-sensing properties [70].
Carbon nanotubes	By placing carbon nanotubes along the channel, the electrical properties of the devices are significantly improved [71].
Others	Nanostructured materials with high surface-to-volume ratios have been used to actuate ISFET sensors for protein sensing [72]. ISFET sensors based on zinc oxide nanorods have been used for glucose monitoring [73], pH testing [74], and DNA detection [75]. Vanadium pentoxide (V_2O_5) nanorods have also been used to fabricate ISFET sensors [76].

A. *Recent gate materials used in ISFET sensors.*

In the study of Phanabamrung et al., Si3N4 was used as the gate covering layer of ISFET to design a sensor based on the antibody-antigen connection of the major histocompatibility complex (MHC) associated with class I related chain A (MICA), and also human leukocyte (HLA). The detection linear range for MICA and HLA was 5.17–40 and 1.98–40 µg/mL, respectively, which indicates the device's good performance. Thus, in this study, the use of Si3N4 for the gate layer was very suitable with high modification [77]. In a recent study, Kim et al. made an initiative to measure two ions, Na+ and K+, by means of an electrode. They designed the reference electrode based on reduced fluorinated graphene oxide, and used indium tin oxide (ITO) as a thin gate layer. Using this sensor, they detected Na+ and K+ ions in human urine with high sensitivity [78]. Also, in another interesting study Hyun and Cho used a K+ selective membrane on a thin layer of amorphous indium gallium zinc oxide coplanar gate to measure K+ concentration. This ISFET-based sensor had excellent selectivity. The results of K+ including the solution and the solution containing other ions (in the absence of K+) were completely different [79].

Megat Hasnan et al. used poly (3,4-ethylene dioxythiophene): poly (styrene sulfonate) composite thin layer with Ti2CTX MXenes layered including bovine serum albumin, and graphene oxide, in an ISFET gate structure for chlorpyrifos detection. This composite layer had higher sensitivity for chlorpyrifos compared to thin films without MXene [80]. This study showed the importance of the correct thin film selection and the gate material used in an ISFET biosensor.

Graphene, as a two-dimensional material consisting only of carbon atoms in a hexagonal structure, has always been a good candidate for sensors [81-83]. In this regard, Alves et al. used a graphene-based ISFET biosensor to measure an antiviral protein inhibiting HIV, recombinant cyanovirin-N (rCV-N). They used the linker 1-pyrene butanoic acid succinimidyl ester (PBSE) to immobilize the antibody on the graphene gate electrode, through the primary and secondary amine groups of the antibody. This biosensor detected rCV-N in the range of 0.01 to 10 ng/ml and the detection limit was 0.45 pg/ml. The easy fixation of the linker on the electrode surface, the stability, and the reusability of this sensor were attributed to the graphene used in the gate terminal [84].

The importance of the ISFET sensors' gate materials, in addition to laboratory research, has also been considered in simulation-based studies. To improve the sensitivity of the ISFET-based sensor, Prakash et al. used Ta2O3, SiO2, Al2O3, and HfO2, in the role of the ISFET gate by COMSOL simulation, and the ISFET with Ta2O3 gate had the highest sensitivity [85].

V. READOUT METHODS

The requirement for higher precision and greater integration of the front circuit and signal readout methods have led to a revolution in the design and application of biosensors based on ISFET. Measurement methods are classified into two types, single and differential measurements. In a single ISFET sensor measurement, two readout methods are involved to achieve continuous encoding. The simplest readout system for the reference electrode is the feedback mode. In this case, the ISFET sensor current is constant, and the pH of the solution changes the voltage feedback to the reference [41]. However, its inadequacy with the conventional reference electrode was the reason for replacing the feedback mode with the current mode. This technique is now widely used in front-end ISFET sensor configurations, including constant current readout (CCR), constant voltage readout, and current mode readout.

The Constant-Voltage, Constant-Current (CVCC) circuit depends on the constant source-drain voltage (VDS) and current identifiers. In the CVCC circuit, by loading a constant voltage between the source and drain of the ISFET, the change in pH is reflected in the changes in the source voltage [86] (Figure 4A). In addition, more pixel architectures have been proposed. The readout unit for the ISFET sensor array consists of three transistors and a single ISFET device: transistor P1 acts as the load by providing constant current, and transfer gate P3/N1 acts as the readout for each pixel [87] (Figure 4B). Another notable method is time-to-pH readout where the C0 capacitor is charged before detection and discharged during pH measurement. In this method, the discharge time depends on the drain-source current of the MN0 transistor, and therefore, on the pH of the solution. The N1 voltage depends on the pH, followed by the conversion of time to voltage, and its value is calculated by turning off the S0 switch after a certain period [43] (Figure 4C).

The differential measurements in the ISFET sensors' signal readout reduces the common-mode signal, noise, and drift [86]. Figure 4D shows the ISFET sensor differential readout system including an ISFET amplifier and a differential amplifier. In the study by Wong et al. a reference ISFET sensor was immersed in solutions of a specified value, and the output signal of the difference between the two ISFET amplifiers was represented by the output signal. The pH of the desired analyte was then calculated, and the shift that occurred in both ISFET sensors was removed in the readout signal. The use of an ideal reference electrode is essential because the differential sensor allows for the elimination of the common-mode voltage between the two sensors, noise reduction, minimizing drift effects and temperature differences [86]. Also, other innovations have been made in this type of reading method for ISFET biosensors [43].

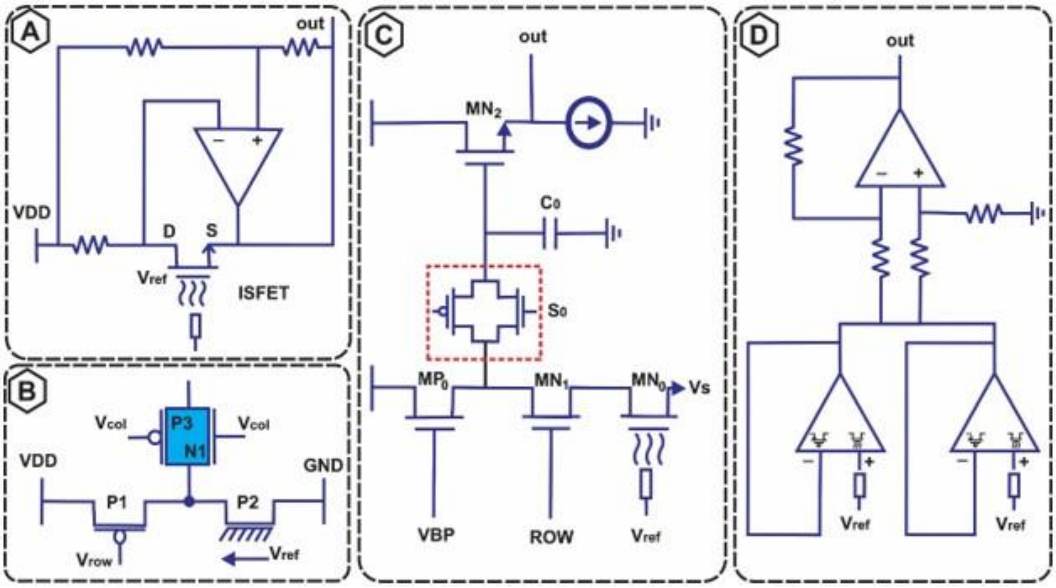

Fig. **4** ISFET sensors readout methods; (A) Source-drain follower circuit; (B) Standard pixel readout; (C) Time-to-pH voltage readout system; and (D) Differential amplifier readout system.

VI. BIOSENSING APPLICATIONS

The intrinsic properties of the gate materials account for the strong response of the ISFET sensors to certain ions. In addition, the interactions between the ISFET gate and biomolecules affect the electrical output of the ISFET. Therefore, ISFET-based sensors are used to detect biomolecules and ions [88]. In Table 4, some recent research in the field of using ISFET biosensors are given. Recent advances in ISFET biosensing are presented in more detail in the following sections.

TABLE 4. SOME RECENT STUDIES OF BIOSENSORS BASED ON ISFET.

Transistor	Research topic	Ref.
ISFET	Real-time detection of integrated RNA in men with prostate cancer.	[89]
ISFET	Detection of antibodies against HLA[a] and MICA[b].	[77]
F[c]-rGO RE-ISFE	Using F-rGO RE in ISFET structure to detect potassium and sodium ions in urine.	[78]
JF-ED-TFET[d]	Simulation of a JF-ED-TFET for label-free biosensing applications.	[90]
FET	Development of a biosensor platform based on IGZO planar thin film gate coplanar transistor for selective detection of K^+.	[79]
ISFET	Sensitive and fast detection of SARS-CoV-2, without Debye length limitation.	[91]
Si NW[e]-FET	Application of Si NW-FET biosensor with graded channel gate for label-free biomolecule detection.	[92]
DG[f]- ISFETs	Application of DG- ISFETs for continuous pH measurement with gate layer capacitance beyond Nernst.	[93]
ISFET	Using a 3x2 differential ISFET integrated pixel array for pH measurement.	[94]

a, Human leukocyte antigen; b, Major histocompatibility complex associated with class I; c, Fluorinated; d, Junction-free tunneling field-effect-based biosensor; e, Silicon nanowire; and f, Double-gate

A. *Ions*

For the first time in 1970 Piet Bergveld used ISFET sensors with a SiO2 gate to detect Cl- and Na+ around nerves [14]. He replaced the classic MOSFET metal gate ISFET with a hybrid ion/electrolyte/RE selective film module and used the resulting device for ion sensing. After this study, the ISFET ion sensor received the scientific community attention. Since then, the ISFET ion sensors have been introduced to the public for performance studies.

ISFET is commonly used for pH sensing. Grasta et al. used ISFET to detect the presence of chloride ions in sweat [95]. This study was done to diagnose cystic fibrosis. They used empirical reality modeling. Gate oxides (HfO2) in a chemical reaction with electrolyte solution, anions (Cl-) directly react with hydroxyl groups and replace surface protons. The Cl- detection limit of the designed device was 4 µmol/m3. They also investigated the effect of oxide width on device performance. In Figure 5, HfO2 is considered as an insulator, and the changes in the dependence of the drain-source current (IDS) on the drain-source voltage (VDS) depend on the four values of dHfO2. In addition to pH sensing (Table 5), ISFET sensers sense various ions such as Na+ [78], Cu2+ [96], and K+ [97], by using different sensitive membranes loaded on modified channel materials and gates. Ions are critical analytes in healthcare and medicine. For example, in a recent study by Annabella la et al., they used a NaCl measuring ISFET device with HfO2 to diagnose and analyze cystic fibrosis. The selective polyvinyl chloride membrane increased the sensibility of the ISFET to other ions [98].

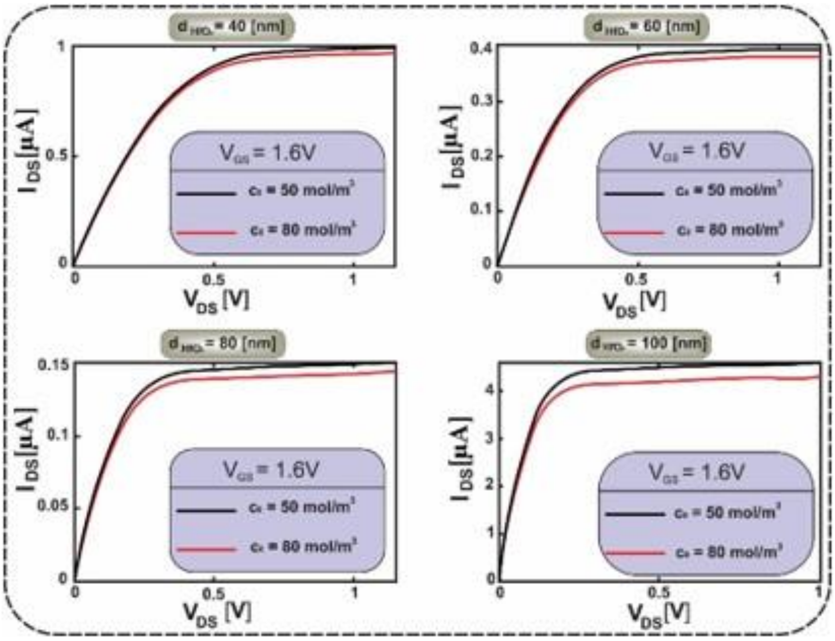

Fig. **2** Investigating the effect of HfO_2 thickness on drain-source current (I_{DS}) versus drain-source voltage (V_{DS}) for two different amounts of Cl^- [95].

TABLE 5. AN OVERVIEW OF SOME STUDIES CONDUCTED IN THE FIELD OF PH DETECTION WITH ISFET SENSORS.

Basis	Target	Linear range	Year	Ref.
Al_2O_3 ISFET	pH detection	1 – 12	2004	[99]
pH-ISFETs	potato glycoalkaloids analysis	-	2005	[100]
pH-MFGFET	pH detection	1 – 13	2008	[101]
SOI-DG[a] ISFETs	pH detection	3 – 11	2013	[102]
Si_3N_4/SiO_2 ISFET	pH detection	2 – 12	2013	[103]
DG-CNT-ISFET[b]	pH detection	5 – 9	2019	[104]
In_2O_3 nano gate ISFET	pH detection to determine the concentration of biomolecules	6 – 10	2020	[105]
UT[c] and TiO_2 gate ISFET	pH detection	1 – 12	2020	[106]
SiO_2/Ta_2O_5 EG-ISFET[d]	pH detection	3 – 10	2020	[107]
Si NW DG[e]-ISFET	pH detection	~3 – 10	2021	[108]
ISFET	pH detection	5 – 11	2022	[109]

a, Silicon-on-insulator dual-gate; b, Dual-gate carbon nanotube ISFET; c, Ultrathin body; d, Extended-gate ISFET; and e, Silicon nanowire dual gate.

B. *DNA*

In accordance with the great importance of accurate detection of nucleic acids in the design and discovery of drugs, diagnosis of various types of cancers and genetic diseases, optical, magnetic, electrochemical, and enzyme assay methods have been developed [110]. The advantage of these methods is high sensitivity and low detection limits, but they have shortcomings such as being expensive and large measuring instruments, complex measuring circuits, harmful labels, and time-consuming preparations [111]. To resolve this problem, the ISFET method is an excellent candidate. Currently, ISFET-based DNA sensing is performed with two mechanisms:

- Enzymatic reactions based on DNA polymerase, which lead to the production of H+ and affect the surface charge distribution of the ISFET gate.
- The other is based on DNA strand hybridization leading to the generation of negative charges that affect the surface charge distribution of the ISFET gate and causes a change in the electrical output of the ISFET [112].

ISFET DNA sensors have high sensitivity, fast detection, low detection limit, high sensitivity, a simple manufacturing process, low cost, and good characteristics. Therefore, many research groups have become interested in their use (Table 6). Based on the advantages, many studies on ISFET-based DNA sensors have been developed in recent years. For example, Mahdavi et al. used 3-aminopropyltriethoxysilane (APTES) to silanize the ISFET gate and immobilize DNA probes on the gate, to make a sensitive DNA sensor. The steps and patterns of the expected data in different stages of the experiment are shown in Figure 6. The sensors were tested during fabrication with 0-5 voltages for both the drain source and the voltage electrode. The reference electrode was Ag/AgCl. Steps 1-7 represented the possible loads for each stage of their experiment and the expected changes in the source-drain current were plotted. DNA hybridization was done in step 5 and the changes in current were proportional to it. This sensor produced an output signal of about 500 mV in the presence of a DNA solution at a concentration of 10 pM. The limit of detection (LOD) of DNA can be 1 fM and the corresponding DNA sensitivity is 50 µV/fM [113].

TABLE 6. SOME CASES OF ISFET-BASED SENSORS IN DNA DETECTION.

Basis	Aim	LOD (µM)	Linear range (µM)	Year	Ref.
CMOS-ISFET[a]	Real-time DNA hybridization	0.2	-	2016	[114]
DG-NR-ISFET[b]	CorDNA[c]	5×10^{-5}	$10 \times 10^{-3} – 1$	2018	[115]
CMOS-ISFET	DNA molecules	1×10^{-5}	$1 \times 10^{-12} – 1$	2020	[116]
EGFET[d]	Cor DNA molecules	1×10^{-2}	$1 \times 10^{-3} – 1$	2020	[117]
CMOS-ISFET	Direct DNA hybridization	1×10^{-5}	$1 \times 10^{-5} – 1 \times 10^{-3}$	2020	[118]

a, Complementary metal-oxide semiconductor-ISFET; b, Dual-gate nanoribbon-based ISFET; c, Cordyceps sinensis's DNA; and d, Extended-Gate FET.

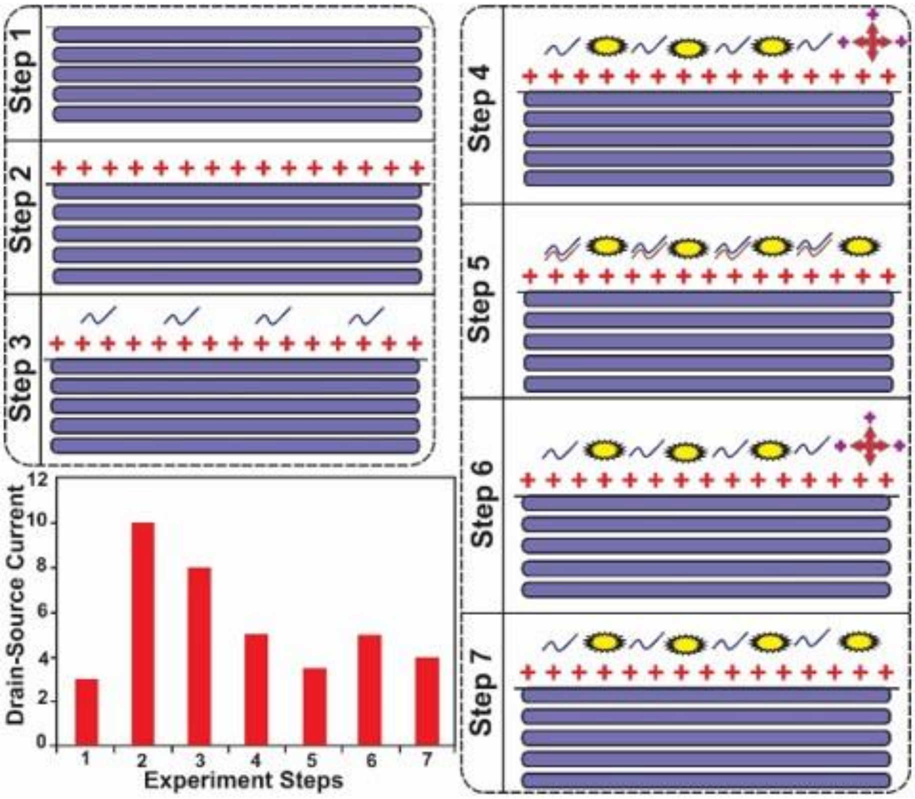

Fig. **6** Test steps pattern and expected data in different test steps. Positive charges are due to APTES entering the surface. The yellow shape of sodium dodecyl sulfate (SDS) is negatively charged, and the red crosses are EDTA molecules [113].

The generation of pyrophosphates during DNA amplification lowers the pH, and this property has been used for silicon based ISFET sensors for DNA detection. However, graphenes are very suitable because of their surface-to-volume ratio. Graphene (π-π bonds) is used for non-covalent stabilization of single-stranded DNA primers because it does not absorb double-stranded DNA. In this regard, Ganguli et al. used Bst polymerase (in silico designed homolog of Bacillus stearothermophilus DNA Polymerase I) in a loop-mediated isothermal amplification (LAMP) reaction in the presence of target-specific primers and crumpled graphene field effect transistors (GFET) to detect amplification by primer reduction assay. They were able to detect the end point of the amplification reaction with initial concentrations of only 8 × 10-21 M of E. coli DNA [119]. ISFET goes beyond the detection of nucleic acids and by entering DNA sequencing technology, it provides important data for gene detection and gene therapy. ISFET sensors are also designed to detect DNA base pairing, which can be useful in DNA sequencing systems [120].

C. *Enzyme-based sensors*

Enzyme-based ISFET sensors are achieved by immobilizing enzymes on the gate surface of ISFET to detect enzyme substrates [121]. As a result of enzymatic reactions, the charge distribution on the gate surface changes, which can be detected by the electrical output. Accordingly, enzyme-based ISFET sensors (ENFETs) have been used to detect many biological analytes such as glucose, penicillin, cholesterol, urea, and dopamine [122]. Due to the choice of the small size of ISFET sensors, high adaptability, fast response of enzymatic reactions, high sensitivity and the need for small sample volume have made ENFET sensors very popular.

Bhatt et al. developed an acetylcholinesterase (AChE) biosensor based on an electrolyte carbon nanotube field effect transistor. The enzyme was immobilized on a flat gold gate electrode with a linker using 3-mercaptopropionic acid. They used least-squares curve fitting and obtained a sensitivity of 5.7 μA/decade. The real-time response was in the concentration range of 1 × 10-12 − 1× 10-3 M (constantly applied biases (VDS) = −0.2 V and (VGS) = −0.8 V) (Figure 8A). This test gave a proportional response to different analyte concentrations, while it was not sensitive to glycine and serine interferences (Figure 8B). This sensor had a high capability in real samples, and as a result it was very resistant and flexible [123]. In general, the design of ISFET sensors based on cholinesterases is of significant interest to researchers.

TABLE 7. SOME STUDIES ON THE APPLICATION OF CHOLINESTERASES IN FET BIOSENSORS.

Transistor	Gate enzyme	Detection substance	LOD (μM)	Linear range (μM)	Year	Ref.
SGGT[a]	AChE[b]	Organophosphorus pesticide	0.01	0.3 – 3	2021	[124]
ISFET	AChE	Indole alkaloids	0.5 μg/ml	2 – 15 μg/ml	2022	[125]
rGO[c] FET	AChE	ACh[d]	2.3	5 – 1000	2020	[126]
rGO FET	AChE	ACh	1 μM	1 – 1 × 10^4	2018	[127]
ISFET	Butyryl cholinesterase	Glycoalkaloids	-	0.03 – 5	2006	[128]

a, solution-gated graphene transistor; b, Acetylcholinesterase; c, Reduced-graphene-oxide; and d, Acetylcholine.

Providing portable sensors requires high flexibility and a flexible substrate. In this regard, Kwak et al. developed a chemical vapor deposition-grown graphene-based FET for glucose sensing. Chemical vapor deposition-grown graphene was functionalized with glucose oxidase enzyme linker molecules. The graphene-based FET sensor had bipolar transmission characteristics. By measuring the Dirac point shift and drain-source differential current, the developed FET sensor detected glucose levels in the range of 3.3 to 10.9 mM. This corresponds to the reference range of medical examinations, and the sensor was very flexible [129]. In another study, Wang et al. developed a FET-based glucose sensor with a bimetallic nickel-copper metal-organic framework (Ni/Cu-MOFs) as its channel layers. They used glutaraldehyde as a linker to immobilize glucose oxidase. The synergistic effect of Ni and Cu ions in MOFs caused the appropriate field effect on glucose. This sensor showed a linear relationship in the range of 1 - 2 × 104 µM, a lower detection limit of 0.51 µM, and a sensitivity of 26.05 µAcm-2mM-1. This sensor had high specificity, reasonable short-term stability, excellent repeatability, and fast response time [130]. In a study based on the glucose oxidase-like activity of nanozymes, Farahmandpour et al. recently developed a non-enzymatic FET sensor for glucose detection. They synthesized CuO hollow spheres decorated with reduced graphene oxide (rGO). These synthesized nanostructured hollow microspheres (rGO/CuO-NHS) were immobilized on a flexible PET substrate between interdigitated electrodes as the channel of a back gate transistor. The high surface-to-volume ratio of the nanostructured shell and the selective porous hollow spheres of CuO along with the high conductivity of rGO became the cause of glucose oxidation with a low detection limit of 1 nM and sensitivity of 600 µA µM−1. In addition, the flexible glucose sensor had high reproducibility (Figure 8C), repeatability (Figure 8D), and good stability (Figure 8E) [131]. Table 8 lists some studies on the use of enzymes for glucose detection.

TABLE 8. SOME CASES OF GLUCOSE OXIDASE /GLUCOSE OXIDASE MIMICS-BASED FET BIOSENSORS.

Transistor	**Gate enzyme**	**LOD (µM)**	**Linear range (µM)**	**Year**	**Ref.**
FET	Ag NPs as an enzyme mimic	-	0.1 – 0.25	2020	[132]
ZnO/CuO-NHS^a FET	Glucose oxidase	0.03	-	2023	[133]
MoS_2 FET	Glucose oxidase	0.3	0.3 – 3 × 10^4	2018	[59]
EGFET	Glucose oxidase	0.001 mg/mL	0.1 – 1 mg/mL	2020	[134]
Silk fibroin-encapsulated graphene FET	Glucose oxidase	100	100 – 1 × 10^4	2014	[121]
rGO/C-PPy NT FET^b		0.001	0.001 – 100	2015	[135]
EGFET	Ga_2O_3 as an enzyme mimic	20	-	2022	[136]

FET	Polyaniline/glucose oxidase	-	$0 – 9 \times 10^3$	2004	[137]
FET	CPPN[d] - Glucose oxidase	500	$2 \times 10^3 – 2 \times 10^4$	2008	[138]
FET	Glucose oxidase	100	$< 1 \times 10^4$	2010	[139]
ISFET	PSW[e]	3.2×10^{-5}	$10^{-4} – 10^{+3}$	2011	[140]
ISFET	Glucose oxidase	25	$50 – 1.8 \times 10^3$	2004	[141]

a nanostructure hollow spheres; b, Extended gate FET; c, Reduced graphene oxide-carboxylated polypyrrole nanotube FET; d, Carboxylated polypyrrole nanotube; and e, Polysilicon wire.

Peroxidases are used as a secondary reaction during assays of various enzymatic processes such as oxidation and immunoassays. Use of ISFET sensors instead of expensive spectrophotometric methods is a suitable option. For example, Tomari et al. used the signal accumulation of an ion-sensitive field effect transistor (SA-ISFET) sensor to measure sarcosine, lactic acid, uric acid and glucose, and detect Escherichia coli (using a peroxidase-labeled antibody) [142]. In another study, Mariia et al. used horseradish peroxidase (HRP) as a label to determine the interaction between thrombin and its aptamer on the surface of ISFET. The complementary sDNA probe containing HRP was replaced by the immobilized aptamer (sDNA) with thrombin, and the HRP activity was assayed. This biosensor detected thrombin with a low detection limit of 7 × 10-7 M [143]. Table 19 lists some studies based on peroxidases in FET sensors.

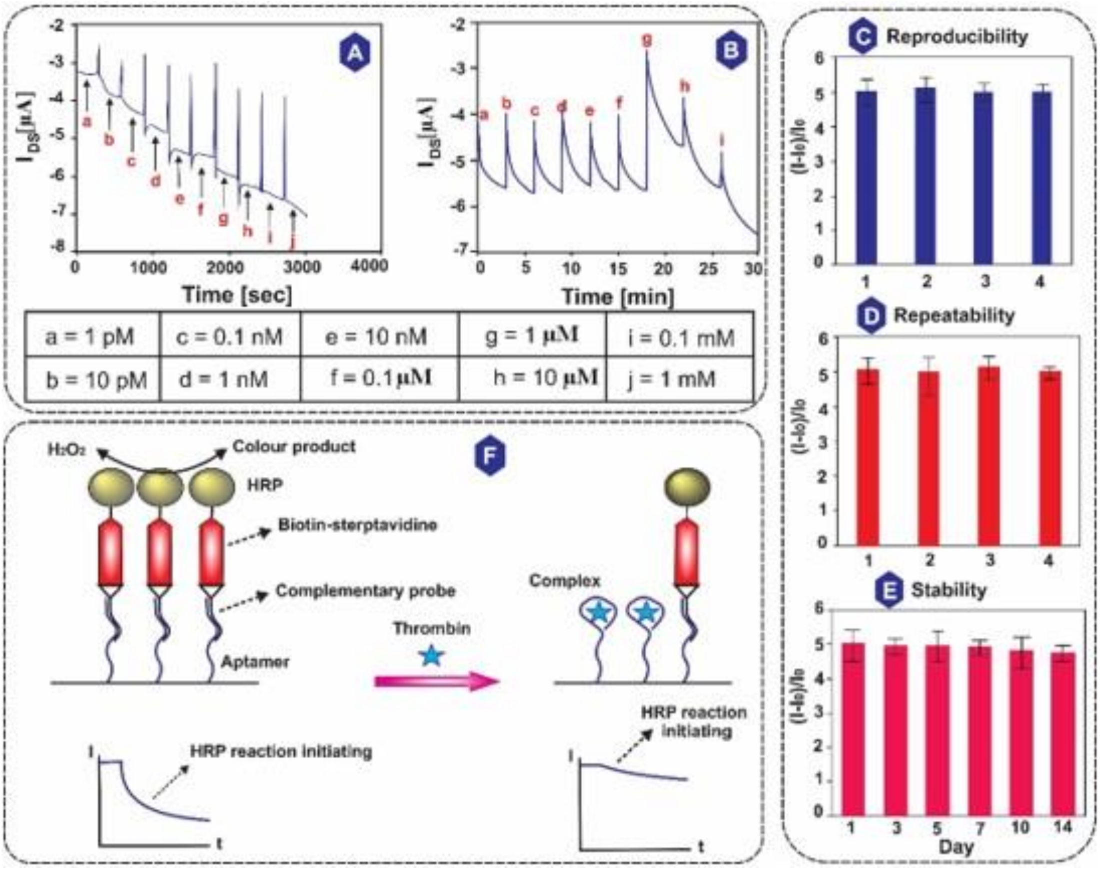

Fig. **7** Real-time sensor response of different acetylcholine concentrations. (D) Selectivity of the sensor for acetylcholine in the presence of serine and glycine (description in text) [123]; (C) Reproducibility for 4 glucose samples with a concentration of 5 nM glucose for the sensor; (D) Repeatability for different sensors with the same manufacturing method in the presence of 5 nM glucose; (E) stability test of the sensor that retained 93% of its activity after 14 days [131]; and (F) Schematic of thrombin displacement and identification [143].

TABLE 9. SOME STUDIES ON THE APPLICATION OF FET SENSORS BASED ON PEROXIDASE ENZYMES/ PEROXIDASE MIMICS.

Transistor	Enzyme	Substrate	LOD (μM)	Linear range (μM)	Year	Ref.
ISFET	HRP[a]	H_2O_2	0.5	Up to thousands	۱۹۹۴	[144]
ISFET	β′-glucosidase, mandelonitrile lyase and HRP	Amygdalin	-	100 – 300	1998	[145]
PVPy[b]-ISFET	HRP	Cyanide	-	0.1 – 10	1998	[146]
ISFET	HRP, glucose oxidase, and urease	Glucose Ascorbic acids Citric acids	-	$10^3 – 10^4$ $250 – 2 \times 10^3$ 0.1 – 10	1998	[147]
ISFET	Peroxidase	Herbicide simazine	1.25 ng ml^{-1}	5–175 ng ml^{-1}	2000	[148]

GFET[c]	HRP, glucose oxidase	Glucose	0.2	$1 – 10^4$	2021	[149]
rGO FET	MoS_2	Releasing H_2O_2 from cancer cell	10^{-6}	-	2019	[60]

a, Horseradish peroxidase; b, Poly(4-vinylpyridine-co-styrene); and c, Graphene field-effect transistor.

Other enzymes are also used in the design of FET-based sensors. For example, Abdul Barik et al. in 2014 used a cholesterol oxidase-potassium-doped CNT-FET to detect cholesterol. The type P-graphene was the electrochemical as a substrate on the ITO glass, and used the N-type graphene sediment. ZrO2 in the channel area played a gate insulation role. The K/PPy/CNT composite formed the sensor layer at the top of the ZrO2 layer. They moved cholesterol oxidase on the K/PPy/CNT membrane with physical absorption techniques. The linear diagnosis range was 0.5 to 20 mM. The sensitivity of this FET was ~ 400 µA/mM/mm2 (R ~ 0.998). This sensor had Michaelis-Menten constant (Km) and the detection limit of 2.5 and 1.4 mM, respectively. Another notable point was the very low interference of glucose, urea, and uric acid in the results [150] (please see more examples in Table 10).

Although the use of nanozymes in FET-based biosensors has not yet reached maturity, significant number of studies have been performed. MXenes are two-dimensional materials with hydrophilicity, high conductivity, and high surface area, and thus are attractive for the design of biosensors. In this regard, Hasnsn et al. used Ti2CTX MXene structures in an ion-sensitive field effect transistor (ISFET) to detect chlorpyrifos (Cpy). The use of a thin layer composite poly (3,4-ethylene dioxythiophene)-poly (styrene sulfonate) layer with layered pieces of Ti2CTX MXenes with graphene oxide and bovine serum albumin (BSA) resulted in the reduction of the minimum electrical threshold voltage Cpy by -0.1 V (the voltage of using TiO2 which is -1.5 V). Considering the potential of Ti2CTx MXene-BSA two-dimensional composite, the detection of CPY with an enzyme-free sensor was available [80].

TABLE 10. APPLICATION OF OTHER ENZYMES IN THE DESIGN OF ISFET BIOSENSORS.

Transistor	**Enzyme**	**Substrate**	**LOD (µM)**	**Linear range (µM)**	**Year**	**Ref.**
ISFET	Creatinine deiminase/ urease	Ammonia	20	20 – 1000	2005	[151]
ISFET	Creatinine deiminase	Ammonia	10	0 – 5000	1998	[152]
ISFET	Creatinine amidohydrolase	API[a]	-	-	2016	[153]
CNT[b]-ISFET	Laccase	ABTS[c]	3	up to 300	2020	[154]
SGGT[d]	Lactate oxidase	lactic acid	0.3	3 – 300	2019	[155]
ISFET	Carbapenemase	Imipenem	0.1	-	2021	[156]
CNT-ISFET	Cholesterol oxidase	Cholesterol	230	$500 – 25 \times 10^3$	2021	[157]
EGFET	Uricase	Uric acid	0.082 mg/dL	2 – 7 mg/dL	2021	[158]

FET	Tyrosinase	Dopamine	0.003	1 – 120	2021	[159]
ISFET	DNA aptamer / alkaline phosphatase	COVID-19 spike proteins	100 copies/µL in 10 min	-	2023	[91]
EGFET	Uricase	Uric acid	-	1-30 mg/dL	2021	[160]
ISFET	Alkaline phosphatase	Interleukin-5	~1 ng/mL	1 pg/mL - 10 ng/mL	2015	[161]

a, Active pharmaceutical ingredients; b, Carbon nanotube; c, 2, 2-azino-bis 3-ethylbenzothiazoline-6-sulphonic acid; and d, Solution-gated graphene transistors.

D. *Antigen-antibody detection*

Antigen-related immune detection is very important for the diagnosis and prevention of diseases such as immune diseases, tuberculosis, and various types of cancer. The main advantage of ISFET is the very little work potential and neutrality in the antigen-antibody interactions [13]. Many studies have been done on the reusability and sensitivity of these sensors. The multi-layered gateway structure is the most used strategy to improve sensitivity. For example, Kutova et al. have developed a multilayer gate from CeO2/SiO2 for ultrasensitive C protein antigen. The sensor was very practical in PBS and human serum to predict inflammation in vivo and diagnose acute diseases [162]. Another important point is to build an ISFET gate with different structures. In this regard, Lee et al. improved performance for antigen diagnosis from hepatitis B levels based on the structure of two gates with an excellent detection limit of 22.5 fg/ml [47]. In addition, the use of nanomaterials on the ISFET gate to increase sensitivity due to the high surface-to-volume ratio can be promising. For example, Kuznetsov et al. used nanoribbons to detect prostate-specific antigens with a limit of detection of 0.4 pg/ml [163]. Finally, it is noteworthy that researchers have not neglected the reusability of the ISFET-based antigen-antibody interaction sensors. Research has been conducted to produce reusable ISFET-based sensors [164].

VII. CONCLUSION AND PERSPECTIVE

The design and improvement of biosensors have always been attractive and extensive research has been conducted in this field. In this regard, ISFET sensors have also been constantly improved. Here we reviewed the working principles and methods of gate operation in ISFET-based biosensors in various studies. ISFETs are excellent sensors for biomolecules such as proteins, DNA, ions, bioanalyses, and biomarkers due to their high sensitivity, reusability, real-time detections, waterproof properties, and all-solids. Of course, these advantages do not mean the maturity of the manufacturing process, use, and commercial development of ISFET-based biosensors, and our perspective is mentioned below.

Debye screening at high concentrations of ionic solutions (protecting analytes from contacting the gate) has slowed the development of ISFET biosensors. Analytes smaller and comparable to Debye are not detected due to the high ionic strength at a distance smaller than λ, at the electrolyte-gate interface, especially for small molecule analytes whose size is comparable and smaller than Debye. To overcome this drawback, probes can be used for connection or nanoparticles in different forms and shapes can be used as the sensor immobilized layer.

One of the important current issues is the use of multiple measurement techniques in one sensor. For this purpose, multiple ISFET sensors can be incorporated into one chip.

However, the miniaturization process as well as the number of wires required for switching on and off will be large. In this case the sensors must work in shifts, and will be expensive in terms of integration cost. However, it is possible to use the light-receiving address system for ISFET. Efforts should also be made to increase the number of analytes measured in an ISFET.

As with the classical behavior of MOSFET sensors, increasing the thickness decreases the sensitivity of the device. The use of an ISFET device for the detection of other biomarkers in readily available biological fluids, consistent with medical applications, is still nascent. Therefore, more efforts should be made to miniaturize more ISFET sensors. Of course, it should be noted that by reducing the thickness of layers and downsizing, the durability and stability of the device is not affected.

One of the problems in the construction and design of most biosensors is the low stability of immobilized biomolecules on the substrate. ISFET sensors are no exception to this rule. In this regard, we predict that in the future research in this field should focus more on the use of nanozymes and nanostructures in the construction and development of ISFET sensors. This will not only provide more stability, but also resolve all the deficiencies in the early generations of ISFET sensors.

REFERENCES

[1] A. Shinde, K. Illath, U. Kasiviswanathan, S. Nagabooshanam, P. Gupta, K. Dey, et al. “Recent Advances of Biosensor-Integrated Organ-on-a-Chip Technologies for Diagnostics and Therapeutics,” Analytical Chemistry, vol. 95, pp. 3121-3146, 2023.

[2] F. Ghasemi and A. Salimi, “Advances in 2D Based Field Effect Transistors as Biosensing Platforms: From Principle to Biomedical Applications,” Microchemical Journal, vol.187 pp.108432, 2023.

[3] K.S. Singh, P. Gupta, M. Rajoriya, N. Kumari, and A. Muskan, “Study of Tunnel Field Effect Transistors for Biosensing Applications: A Review,” International Conference on Computing, Communication, and Intelligent Systems (ICCCIS): IEEE, vol. 144, pp. 1-5, 2022.

[4] R. Jalili, A. Khataee, M-R. Rashidi, and A. Razmjou, “Detection of penicillin G residues in milk based on dual-emission carbon dots and molecularly imprinted polymers,” Food chemistry, vol. 314, pp. 126172, 2020.

[5] R. Shiwaku, H. Matsui, K. Nagamine, M. Uematsu, T. Mano, and Y .Maruyama, et al, “A printed organic amplification system for wearable potentiometric electrochemical sensors,” Scientific reports, vol. 8, pp. 3922 (1-8), 2018.

[6] M. Adampourezare, G. Dehghan, M. Hasanzadeh, and M-AH. Feizi, “Application of lateral flow and microfluidic bio-assay and biosensing towards identification of DNA-methylation and cancer detection: Recent progress and challenges in biomedicine,” Biomedicine & Pharmacotherapy, vol. 141, pp. 111845, 2021.

[7] H. Sohrabi, MR. Majidi, O. Arbabzadeh, P. Khaaki, S. Pourmohammad, A. Khataee, et al, “Recent advances in the highly sensitive determination of zearalenone residues in water and environmental resources with electrochemical biosensors,” Environmental Research, vol. 204, pp. 112082, 2022.

[8] T. Kuno, K. Niitsu, and K. Nakazato, “Amperometric electrochemical sensor array for on-chip simultaneous imaging,” Japanese Journal of Applied Physics, vol.53, pp. 04EL1, 2014.

[9] P. Bertoncello and R.J. Forster, “Nanostructured materials for electrochemiluminescence (ECL)-based detection methods: recent advances and future perspectives,” Biosensors and Bioelectronics, vol. 24, pp. 3191-3200, 2009.

[10] S. Rashtbari, G. Dehghan, S. Khataee, M. Amini, and A. Khataee, “Dual enzymes-mimic activity of nanolayered manganese-calcium oxide for fluorometric determination of metformin," Chemosphere, vol. 291, pp. 133063, 2022.

[11] S. Rashtbari, G. Dehghan, and M. Amini, "An ultrasensitive label-free colorimetric biosensor for the detection of glucose based on glucose oxidase-like activity of nanolayered manganese-calcium oxide," Analytica chimica acta, vol. 1110, pp. 98-108, 2020.

[12] B.A. Prabowo, A. Purwidyantri, and K-C. Liu, "Surface plasmon resonance optical sensor: A review on light source technology," Biosensors, vol. 8, pp. 1-28, 2018.

[13] S. Cao, P. Sun, G. Xiao, Q. Tang, X. Sun, H. Zhao, Sh. Zhao, H. Lu, and Z. Yue, "ISFET-based sensors for (bio) chemical applications: A review," Electrochemical Science Advances, vol. 3, pp e2100207 (1-25), 2022.

[14] P. Bergveld, "Development of an ion-sensitive solid-state device for neurophysiological measurements," IEEE Transactions on biomedical engineering, vol. 17, pp .70-71, 1970.

[15] Y. Su, W. Hsu, and CT. Lin, "Review field effect transistor biosensing: devices and clinical applications," ECS J Solid State Sci Technol, vol.7, pp. Q3196 (1-7), 2018.

[16] W-S. Kao, Y-W. Hung, and C-H. Lin, "Solid-State Sensor Chip Produced with Single Laser Engraving for Urine Acidity and Total Dissolved Ion Detections," ECS Journal of Solid State Science and Technology, vol. 9, pp. 115016, 2020.

[17] JT. Smith, SS. Shah, M. Goryll, JR. Stowell, and DR. Allee, "Flexible ISFET biosensor using IGZO metal oxide TFTs and an ITO sensing layer," IEEE Sensors Journal, Vol. 14, pp. 937-938, 2013.

[18] T. Wadhera, D. Kakkar, G. Wadhwa, and B. Raj, "Recent advances and progress in development of the field effect transistor biosensor: A review," Journal of Electronic Materials, vol. 48, pp. 7635-7646, 2019.

[19] AM. Dinar, AM. Zain, and F. Salehuddin, "Utilizing of CMOS ISFET sensors in DNA applications detection: A systematic review," Jour Adv Res Dyn Control Syst. Vol. 10, pp. 569-583, 2018.

[20] L. Keeble, N. Moser, J. Rodriguez-Manzano, and P. Georgiou, "ISFET-based sensing and electric field actuation of DNA for on-chip detection: A review," IEEE Sensors Journal, vol. 20, pp. 11044-11065, 2020.

[21] Y-C. Syu, W-E. Hsu, and C-T. Lin, "Field-effect transistor biosensing: Devices and clinical applications," ECS Journal of Solid State Science and Technology, vol. 7, pp. Q3196, 2018.

[22] M. Wróblewska, "Miniaturized multiplexed bipotentiostat for field-effect transistor based biosensing: Katedra," Biotechnologii Medycznej, 2023.

[23] JE. Lilienfeld and O. Heil, Transistor efek–medan. System.800:000.

[24] W. Shockley, "A unipolar field-effect transistor," Proceedings of the IRE. Vol. 40, pp. 1365-1376, 1952.

[25] D. Kahng, "Silicon-silicon dioxide field induced surface devices," IRE Solid State Device Res Conf1960.

[26] Jr LC. Clark and C. Lyons, "Electrode systems for continuous monitoring in cardiovascular surgery," Annals of the New York Academy of sciences, vol. 102, pp. 29-45, 1962.

[27] P. Bergveld, "Development, operation, and application of the ion-sensitive field-effect transistor as a tool for electrophysiology," IEEE Transactions on Biomedical Engineering, vol. , pp. 342-351, 1972.

[28] K. Lundström, M. Shivaraman, and C. Svensson. "A hydrogen-sensitive Pd-gate MOS transistor," Journal of Applied Physics, vol.46, pp. 3876-3881, 1975.

[29] S. Caras and J. Janata. "Field effect transistor sensitive to penicillin," Analytical chemistry, vol. 52, pp. 1935-1937, 1980.

[30] L. Bousse, De. Rooij NF, and P. Bergveld, "Operation of chemically sensitive field-effect sensors as a function of the insulator-electrolyte interface," IEEE Transactions on Electron Devices, vol. 30, pp. 1263-1270, 1983.

[31] J-i. Anzai, T. KUSANO, T. OSA, H. NAKAJIMA, T. MATSUO, “Urea sensor based on ion sensitive field effect transistor coated with cross-linked urease-albumin membrane,” Bunseki Kagaku, vol. 33, pp. E131-E136, 1984.

[32] Y. Miyahara, T. Moriizumi, and K. Ichimura, “Integrated enzyme FETs for simultaneous detections of urea and glucose,” Sensors and Actuators, vol. 7, pp. 1-10, 1985.

[33] BH. van der Schoot and P. Bergveld, “ISFET based enzyme sensors,” Biosensors, vol. 3, pp. 161-86, 1987.

[34] O. Boubriak, A. Soldatkin, N. Starodub, A. Sandrovsky, and A. El'skaya, “Determination of urea in blood serum by a urease biosensor based on an ion-sensitive field-effect transistor,” Sensors and Actuators B: Chemical, vol. 27, pp. 429-431, 1995.

[35] PB. Luppa, LJ. Sokoll, and DW. Chan, “Immunosensors—principles and applications to clinical chemistry,” Clinica chimica acta, vol. 314, pp. 1-26, 2001.

[36] DE. Yates, S. Levine, and TW. Healy, “Site-binding model of the electrical double layer at the oxide/water interface,” Journal of the Chemical Society, Faraday Transactions 1: Physical Chemistry in Condensed Phases, vol.70, pp. 1807-1818, 1974.

[37] AJ. Bard, LR Faulkner electrochemical methods, W iley, New York. 1980.

[38] A. Van den Berg, P. Bergveld, D. Reinhoudt, and E. Sudhölter, “Sensitivity control of ISFETs by chemical surface modification,” Sensors and Actuators, vol. 8, pp. 129-148, 1985.

[39] M. Yuqing, G. Jianguo, and C. Jianrong, “Ion sensitive field effect transducer-based biosensors,” Biotechnology advances, vol. 21, pp. 527-534, 2003.

[40] A. Simonis, T. Krings, H. Lüth, J. Wang, and MJ. Schöning, “A hybrid thin-film pH sensor with integrated thick-film reference,” Sensors, vol. 1, pp. 183-192, 2001.

[41] P. Bergveld, “Thirty years of ISFETOLOGY: What happened in the past 30 years and what may happen in the next 30 years,” Sensors and Actuators B: Chemical, vol. 88, pp. 1-20, 2003.

[42] R. Datar and G. Bacher, “Influence of Gate Material, Geometry, and Temperature on ISFET Performance in pH Sensing Applications,” Silicon, vol. 1, pp. 1-13, 2023.

[43] X. Ma, R. Peng, W. Mao, Y. Lin, and H. Yu, “Recent advances in ion-sensitive field-effect transistors for biosensing applications,” Electrochemical Science Advances, vol. , pp. e2100163, 2022.

[44] S. Honda, M. Shiomi, T. Yamaguchi, Y. Fujita, T. Arie, S. Akita, et al. “Detachable Flexible ISFET-Based pH Sensor Array with a Flexible Connector,” Advanced Electronic Materials, vol. 6, pp. 2000583, 2020.

[45] J. Zhang, M. Rupakula, F. Bellando, E. Garcia Cordero, J. Longo, F. Wildhaber, et al. “Sweat biomarker sensor incorporating picowatt, three-dimensional extended metal gate ion sensitive field effect transistors,” Acs Sensors, vol. 4, pp. 2039-2047, 2019.

[46] H-J. Jang and W-J. Cho, “High performance silicon-on-insulator based ion-sensitive field-effect transistor using high-k stacked oxide sensing membrane,” Applied Physics Letters, vol. 99, pp. 043703, 2011.

[47] I-K. Lee, M. Jeun, H-J. Jang, W-J. Cho, and K. Lee, “A self-amplified transistor immunosensor under dual gate operation: highly sensitive detection of hepatitis B surface antigen,” Nanoscale, vol. 7, pp. 16789-16797, 2015.

[48] Y-H. Chang, Y-S. Lu, Y-L. Hong, S. Gwo, JA. Yeh, “Highly sensitive pH sensing using an indium nitride ion-sensitive field-effect transistor,” IEEE Sensors Journal, vol. 11, pp. 1157-1161, 2010.

[49] M. Myers, FLM. Khir, A. Podolska, GA. Umana-Membreno, B. Nener, M. Baker, et al. “Nitrate ion detection using AlGaN/GaN heterostructure-based devices without a reference electrode,” Sensors and Actuators B: Chemical, vol. 181, pp. 301-305, 2013.

[50] H. Abe, M. Esashi, and T. Matsuo, “ISFET's using inorganic gate thin films. IEEE Transactions on Electron Devices,” vol. 26, pp. 1939-1944, 1979.

[51] J. Kwon, B-H. Lee, S-Y. Kim, J-Y. Park, H. Bae, Y-K. Choi, et al. “Nanoscale FET-based transduction toward sensitive extended-gate biosensors,” ACS sensors, vol. 4, pp. 1724-1729, 2019.

[52] R. Chaudhary, A. Sharma, S. Sinha, J. Yadav, R. Sharma, R. Mukhiya, et al. “Fabrication and characterisation of Al gate n-metal–oxide–semiconductor field-effect transistor, on-chip fabricated with silicon nitride ion-sensitive field-effect transistor,” IET Computers & Digital Techniques, vol. 10, pp. 268-272, 2016.

[53] P. Firek, M. Wáskiewicz, B. Stonio, and J. Szmidt, “Properties of AlN thin films deposited by means of magnetron sputtering for ISFET applications,” Materials Science-Poland, vol. 33, pp. 669-676, 2015.

[54] S. Nakata, T. Arie, S. Akita, K. Takei, “Wearable, flexible, and multifunctional healthcare device with an ISFET chemical sensor for simultaneous sweat pH and skin temperature monitoring,” ACS sensors, vol. 2, pp. 443-448, 2017.

[55] K. Singh, J-L. Her, B-S. Lou, S-T. Pang, and T-M. Pan, “An extended-gate FET-based pH sensor with an InZn x O y membrane fabricated on a flexible polyimide substrate at room temperature,” IEEE Electron Device Letters, vol. 40, pp. 804-807, 2019.

[56] Q. Zhang, HS. Majumdar, M. Kaisti, A. Prabhu, A. Ivaska, R. Österbacka, et al. “Surface functionalization of ion-sensitive floating-gate field-effect transistors with organic electronics,” IEEE Transactions on Electron Devices, vol. 62, pp. 1291-1298, 2015.

[57] L. Chen, H. Yu, J. Zhong, J. Wu, and W. Su, “Graphene based hybrid/composite for electron field emission: a review,” Journal of Alloys and Compounds, vol. 749, pp. 60-84, 2018.

[58] B. Radisavljevic, A. Radenovic, J. Brivio, V. Giacometti, and A. Kis, “Single-layer MoS2 transistors,” Nature nanotechnology, vol. 6, pp. 147-150, 2011.

[59] J. Shan, J. Li, X. Chu, M. Xu, F. Jin, X. Wang, et al. “High sensitivity glucose detection at extremely low concentrations using a MoS 2-based field-effect transistor,” RSC advances, vol. 8, pp. 7942-7948, 2018.

[60] C. Zheng, X. Jin, Y. Li, J. Mei, Y. Sun, M. Xiao, et al. “Sensitive molybdenum disulfide based field effect transistor sensor for real-time monitoring of hydrogen peroxide,” Scientific Reports, vol.9, pp. 759, 2019.

[61] G. Zhou, J. Chang, H. Pu, K. Shi, S. Mao, X. Sui, et al. “Ultrasensitive mercury ion detection using DNA-functionalized molybdenum disulfide nanosheet/gold nanoparticle hybrid field-effect transistor device,” Acs Sensors, vol.1, pp. 295-302, 2016.

[62] J. Chang, H. Pu, SA. Wells, K. Shi, X. Guo, G. Zhou, et al. “Semi-quantitative design of black phosphorous field-effect transistor sensors for heavy metal ion detection in aqueous media,” Molecular Systems Design & Engineering, vol.4, pp. 491-502, 2019.

[63] Y. Chen, R. Ren, H. Pu, J. Chang, S. Mao, and J. Chen, “Field-effect transistor biosensors with two-dimensional black phosphorus nanosheets,” Biosensors and Bioelectronics, vol. 89, pp. 505-510, 2017.

[64] S. Kim, G. Lee, and J. Kim, “Chemical doping effects of gas molecules on black phosphorus field-effect transistors,” ECS Journal of Solid State Science and Technology, vol. 7, pp. Q3065, 2018.

[65] X. Li, Y. Lu, and Q. Liu, “Electrochemical and optical biosensors based on multifunctional MXene nanoplatforms: Progress and prospects, Talanta, vol. 235, pp. 122726, 2021.

[66] B. Xu, M. Zhu, W. Zhang, X. Zhen, Z. Pei, Q. Xue, et al. “Ultrathin MXene-micropattern-based field-effect transistor for probing neural activity,” Advanced Materials, vol.28, pp. 3333-3339, 2016.

[67] S. Hao, C. Liu, X. Chen, B. Zong, X. Wei, Q. Li, et al. “Ti3C2Tx MXene sensor for rapid Hg2+ analysis in high salinity environment," Journal of Hazardous Materials, vol. 418, pp.126301, 2021.

[68] C. Liu, S. Hao, X. Chen, B. Zong, and S. Mao, "High Anti-Interference Ti3C2T x MXene Field-Effect-Transistor-Based Alkali Indicator," ACS applied materials & interfaces, vol. 12, pp. 32970 (1-8), 2020.

[69] Y. Li, Z. Peng, NJ. Holl, MR. Hassan, JM. Pappas, C. Wei, et al. "MXene–graphene field-effect transistor sensing of influenza virus and SARS-CoV-2, ACS omega, vol.6, pp. 6643-6653, 2021.

[70] S. Kim, T. Rim, K. Kim, U. Lee, E. Baek, H. Lee, et al. "Silicon nanowire ion sensitive field effect transistor with integrated Ag/AgCl electrode: pH sensing and noise characteristics," Analyst, vol. 136, pp. 5012-5016, 2011.

[71] Z. Dong and UC. Wejinya, "Chalamalasetty SNS. Development of CNT-ISFET based pH sensing system using atomic force microscopy," Sensors and Actuators A: Physical, vol. 173, pp. 293-301, 2012.

[72] S. Ma, X. Li, Y-K. Lee, and A. Zhang, "Direct label-free protein detection in high ionic strength solution and human plasma using dual-gate nanoribbon-based ion-sensitive field-effect transistor biosensor," Biosensors and Bioelectronics, vol. 117, pp. 276-282, 2018.

[73] C-T. Lee and Y-S. Chiu, "Photoelectrochemical passivated ZnO-based nanorod structured glucose biosensors using gate-recessed AlGaN/GaN ion-sensitive field-effect-transistors," Sensors and Actuators B: Chemical, vol. 210, pp. 756-761, 2015.

[74] S-J. Young, L-T. Lai, and W-L. Tang, "Improving the performance of pH sensors with one-dimensional ZnO nanostructures," IEEE Sensors Journal, vol. 19, pp. 10972(1-6), 2019.

[75] M. Hajmirzaheydarali, M. Akbari, A. Shahsafi, S. Soleimani-Amiri, M. Sadeghipari, S. Mohajerzadeh, et al. "Ultrahigh sensitivity DNA detection using nanorods incorporated ISFETs," IEEE Electron Device Letters, vol. 37, pp. 663-666, 2016.

[76] N. Abd-Alghafour, NM. Ahmed, Z. Hassan, and MA. Almessiere, "Hydrothermal synthesis and structural properties of V2O5 Nanoflowers at low temperatures," Journal of Physics: Conference Series, Vol. 1083, pp. 012036, 2018.

[77] T.Z.M.M.M. Min, S. Phanabamrung, W. Chaisriratanakul, A. Pankiew, A. Srisuwan, K. Chauyrod, et al. "Biosensors Based on Ion-Sensitive Field-Effect Transistors for HLA and MICA Antibody Detection in Kidney Transplantation," Molecules, vol.27, pp. 6697, 2022.

[78] DH. Kim, HS. Cho, J.H. Kim, DA. Jo, HG. Oh, BK. Jang, et al. "The integration of reference electrode for ISFET ion sensors using fluorothiophenol-treated RGO," Biosensors, vol.13, pp. 89, 2023.

[79] T-H. Hyun and W-J. Cho, "High-Performance Potassium-Selective Biosensor Platform Based on Resistive Coupling of a-IGZO Coplanar-Gate Thin-Film Transistor," International Journal of Molecular Sciences, vol. 24, pp. 6164, 2023.

[80] MM. Hasnan, G. Lim, N. Nayan, C. Soon, AA. Halim, M. Ahmad, et al. "The investigation of chlorpyrifos (Cpy) detection of PEDOT: PSS-MXene (Ti2CT X)-BSA-GO composite using P-ISFET reduction method," Polymer Bulletin, vol. 80, pp. 1243-1264, 2023.

[81] AA. Noroozi and Y. Abdi, "A graphene/Si Schottky diode for the highly sensitive detection of protein," RSC advances, vol.9, pp. 19613-19619, 2019.

[82] A. Ghadakchi and Y. Abdi, "Reduced graphene oxide/silicon nanowire heterojunction for high sensitivity and broadband photodetector," IEEE Sensors Letters, vol. 3, pp. 1-4, 2019.

[83] A. Şenocak, E. Korkmaz, A. Khataee, and E. Demirbas, "A facile and synergetic strategy for electrochemical sensing of rutin antioxidant by Ce–Cr doped magnetite@ rGO," Materials Chemistry and Physics, vol. 275, pp. 125298, 2022.

[84] PR. de Almeida, AM. Murad, LP. Silva, EL. Rech, and ES. Alves, "Development of a Graphene-Based Biosensor for

Detecting Recombinant Cyanovirin-N," Biosensors, vol. 10, pp. 206, 2020.

[85] MD. Prakash, BG. Nelam, S. Ahmadsaidulu, A. Navaneetha, and AK. Panigrahy, "Performance analysis of ion-sensitive field effect transistor with various oxide materials for biomedical applications," Silicon, vol.1, pp. 1-11, 2021.

[86] N. Moser, TS. Lande, C. Toumazou, and P. Georgiou, "ISFETs in CMOS and emergent trends in instrumentation: A review," IEEE Sensors Journal, vol. 16, pp. 6496-6514, 2016.

[87] B. Nemeth, MS. Piechocinski, and DR. Cumming, "High-resolution real-time ion-camera system using a CMOS-based chemical sensor array for proton imaging," Sensors and Actuators B: Chemical, vol. 171, pp. 747-752, 2012.

[88] V. Pachauri and S. Ingebrandt, "Biologically sensitive field-effect transistors: from ISFETs to NanoFETs," Essays in biochemistry, vol. 60, pp. 81-90, 2016.

[89] J. Broomfield, M. Kalofonou, T. Pataillot-Meakin, SM. Powell, RC. Fernandes, N. Moser, et al. "Detection of YAP1 and AR-V7 mRNA for Prostate Cancer prognosis using an ISFET Lab-On-Chip platform," ACS sensors, vol. 7, pp. 3389-3398, 2022.

[90] MK. Bind and K. Nigam, "Sensitivity analysis of junction free electrostatically doped tunnel-FET based biosensor," Silicon, vol. 1, pp. 1-13, 2022.

[91] A. Nukazuka, S. Asai, K. Hayakawa, K. Nakagawa, M. Kanazashi, H. Kakizoe, et al. "Electrical biosensing system utilizing ion-producing enzymes conjugated with aptamers for the sensing of severe acute respiratory syndrome coronavirus 2," Sensing and Bio-Sensing Research, vol. , pp. 100549, 2023.

[92] V. Dhandapani and B. Raj, "Design and Performance Assessment of Graded Channel Gate-All-Around Silicon Nanowire FET for Biosensing Applications, Silicon, vol. , pp. 1-8, 2023.

[93] Y. Kim and W-J. Cho, "Self-sensitivity amplifiable dual-gate ion-sensitive field-effect transistor based on high-k engineered dielectric layer," Japanese Journal of Applied Physics. 2023.

[94] V. Prathap and AH. Titus, "ISFET Pixel Array with selectable sensitivity and bulk-based offset-drift nullification capability for reduction of non-ideality effects," IEEE Sensors Journal. 2023.

[95] A. la Grasta, M. De Carlo, A. Di Nisio, F. Dell'Olio and VM. Passaro, "Potentiometric Chloride Ion Biosensor for Cystic Fibrosis Diagnosis and Management: Modeling and Design," Sensors, vol. 23, pp. 2491, 2023.

[96] O. Synhaivska, Y. Mermoud, M. Baghernejad, I. Alshanski, M. Hurevich, S. Yitzchaik, et al. "Detection of Cu2+ ions with GGH peptide realized with Si-nanoribbon ISFET," Sensors, vol. 19, pp. 4022, 2019.

[97] I. Fakih, A. Centeno, A. Zurutuza, B. Ghaddab, M. Siaj, and T. Szkopek, "High resolution potassium sensing with large-area graphene field-effect transistors," Sensors and Actuators B: Chemical, vol. 291, pp. 89-95, 2019.

[98] A. la Grasta, M. De Carlo, F. Dell'Olio, and VM. Passaro, "Modelling and Design of an ISFET-Based NaCl Sensor for Cystic Fibrosis Diagnosis and Management," Proceedings of SIE 2022: 53rd Annual Meeting of the Italian Electronics Society: Springer, vol. , pp. 117-121, 2023.

[99] RA. Rani and O. Sidek, "ISFET pH sensor characterization: towards biosensor microchip application," IEEE Region 10 Conference TENCON, Vol. 500, pp. 660-663, 2004.

[100] AP. Soldatkin, VN. Arkhypova, SV. Dzyadevych, V. Anna, J-M. Gravoueille, N. Jaffrezic-Renault, et al. "Analysis of the potato glycoalkaloids by using of enzyme biosensor based on pH-ISFETs," Talanta, vol.66, pp. 28-33, 2005.

[101] D. Zhu, Y. Sun, and Z. Shi, "Research of CMOS biosensor IC for extracellular electrophysiological signal recording and pH value measuring," 2008 9th International Conference on Solid-State and Integrated-Circuit Technology: IEEE, vol. , pp. 2557-60, 2008.

[102] T-E. Bae, H-J. Jang, S-W. Lee, and W-J. Cho, “Enhanced sensing properties by dual-gate ion-sensitive field-effect transistor using the solution-processed Al2O3 sensing membranes,” Japanese Journal of Applied Physics, vol. 52, pp. 06GK3, 2013.

[103] HJ. Chen and C-Y. Chen, “Ion-sensitive field-effect transistors with periodic-groove channels fabricated using nanoimprint lithography,” IEEE electron device letters, vol.34, pp. 541-543, 2013.

[104] JC. Dutta, HR. Thakur, and G. Keshwani, “High-Performance Dual-Gate Carbon Nanotube Ion-Sensitive Field Effect Transistor With High-$\kappa $ Top Gate and Low-$\kappa $ Bottom Gate Dielectrics,” IEEE Sensors Journal, vol. 19, pp. 5692-5699, 2019.

[105] Y. Wang, M. Yang, and C. Wu, “Design and implementation of a pH sensor for micro solution based on nanostructured ion-sensitive field-effect transistor,” Sensors, vol. 20, pp. 6921, 2020.

[106] A. Zain, AM. Dinar, F. Salehuddin, H. Hazura, A. Hanim, S. Idris, et al. “Beyond Nernst Sensitivity of Ion Sensitive Field Effect Transistor based on Ultra-Thin Body Box FDSOI,” Journal of Physics: Conference Series, Vol. 1502, pp. 012048, 2020.

[107] Jeon J-H, Cho W-J. “High-performance extended-gate ion-sensitive field-effect transistors with multi-gate structure for transparent, flexible, and wearable biosensors,” Science and Technology of Advanced Materials. Vol. 21, pp. 371-378, 2020.

[108] Cho S-K, Cho W-J. “Ultra-high sensitivity pH-sensors using silicon nanowire channel dual-gate field-effect transistors fabricated by electrospun polyvinylpyrrolidone nanofibers pattern template transfer,” Sensors and Actuators B: Chemical. Vol. 326, pp.128835, 2021.

[109] BS. Emmanuel, “Analysis of output characteristics of ion sensitive field effect transistor based biosensor for measurement of pH in biochemical solutions,” Global Journal of Engineering and Technology Advances. Vol. 11, pp. 087-095, 2022.

[110] Vu C-A, Chen W-Y. “Field-effect transistor biosensors for biomedical applications: recent advances and future prospects,” Sensors. Vol. 19, pp. 4214, 2019.

[111] B. Veigas, E. Fortunato, and PV. Baptista. “Field effect sensors for nucleic acid detection: recent advances and future perspectives,” Sensors. Vol. 15, pp.10380-10398, 2015.

[112] Lee C-S, Kim SK, and Kim M. “Ion-sensitive field-effect transistor for biological sensing,” Sensors. Vol. 9, pp. 7111-7131, 2009.

[113] M. Mahdavi, A. Samaeian, M. Hajmirzaheydarali, M. Shahmohammadi, S. Mohajerzadeh, and M. Malboobi, “Label-free detection of DNA hybridization using a porous poly-Si ion-sensitive field effect transistor,” RSC advances. Vol. 4, pp. 36854-36863, 2014.

[114] Xu G, Abbott J, and Ham D. “Optimization of CMOS-ISFET-based biomolecular sensing: analysis and demonstration in DNA detection,” IEEE Transactions on Electron Devices. Vol. 63, pp. 3249-3256, 2016.

[115] Ma S, Lee Y-K, Zhang A, and Li X. “Label-free detection of Cordyceps sinensis using dual-gate nanoribbon-based ion-sensitive field-effect transistor biosensor,” Sensors and Actuators B: Chemical. Vol. 264, pp. 344-352, 2018.

[116] Chang C-F, and Lu MS-C, “CMOS ion sensitive field effect transistors for highly sensitive detection of DNA hybridization,” IEEE Sensors Journal. Vol. 20, pp. 8930-8937, 2020.

[117] Xu Y, Tavakkoli H, Xu J, and Lee Y-K. A. “Low-drift Extended-Gate Field Effect Transistor (EGFET) with Differential Amplifier for Cordyceps Sinensis DNA Detection Optimized by g m/I D Theory,” 2020 IEEE 15th International Conference on Nano/Micro Engineered and Molecular System (NEMS): IEEE, pp. 398-401, 2020.

[118] Lee C, Chen Y-W, and Lu MS-C. “CMOS biosensors for the detection of DNA hybridization in high ionic-strength solutions,” IEEE Sensors Journal. Vol. 21, pp. 4135-4142, 2020.

[119] A. Ganguli, V. Faramarzi, A. Mostafa, MT. Hwang, S. You, and R. Bashir. “High sensitivity graphene field effect transistor-based detection of DNA amplification,” Advanced Functional Materials. Vol. 30, pp. 2001031, 2020.

[120] P. Sun, Y. Cong, M. Xu, H. Si, D. Zhao, and D. Wu, “An ISFET microarray sensor system for detecting the DNA base pairing,” Micromachines. Vol. 12, pp. 731, 2021.

[121] X. You and JJ. Pak, “Graphene-based field effect transistor enzymatic glucose biosensor using silk protein for enzyme immobilization and device substrate,” Sensors and Actuators B: Chemical. Vol. 202, pp. 1357-1365, 2014.

[122] L. Sarcina, E. Macchia, A. Tricase, C. Scandurra, A. Imbriano, F. Torricelli, et al. “Enzyme based field effect transistor: State-of-the-art and future perspectives,” Electrochemical Science Advances. pp. e2100216, 2022 .

[123] Bhatt VD, Joshi S, Becherer M, and Lugli P. “Flexible, low-cost sensor based on electrolyte gated carbon nanotube field effect transistor for organo-phosphate detection,” Sensors. Vol. 17, pp. 1147, 2017.

[124] Wang R, Wang Y, Qu H, and Zheng L. “An Acetylcholinesterase-Functionalized Biosensor for Sensitive Detection of Organophosphorus Pesticides Based on Solution-Gated Graphene Transistors,” ACS Agricultural Science & Technology. Vol. 1, pp. 372-378, 2021.

[125] Arkhypova V, Soldatkin O, Mozhylevska L, Konvalyuk I, Kunakh V, and Dzyadevych S. “Enzyme biosensor based on pH-sensitive field-effect transistors for assessment of total indole alkaloids content in tissue culture of Rauwolfia serpentine,” Electrochemical Science Advances. Vol. 2, pp. e2100152, 2022.

[126] Fenoy GE, Marmisollé WA, Azzaroni O, and Knoll W. “Acetylcholine biosensor based on the electrochemical functionalization of graphene field-effect transistors,” Biosensors and Bioelectronics. Vol. 148, pp. 111796, 2020.

[127] Chae M-S, Yoo YK, Kim J, Kim TG, and Hwang KS. “Graphene-based enzyme-modified field-effect transistor biosensor for monitoring drug effects in Alzheimer’s disease treatment,” Sensors and Actuators B: Chemical. Vol. 272, pp. 448-458, 2018.

[128] Korpan YI, Raushel FM, Nazarenko EA, Soldatkin AP, Jaffrezic-Renault N, and Martelet C. “Sensitivity and specificity improvement of an ion sensitive field effect transistors-based biosensor for potato glycoalkaloids detection,” Journal of agricultural and food chemistry. Vol. 54, pp. 707-712, 2006.

[129] Kwak YH, Choi DS, Kim YN, Kim H, Yoon DH, Ahn S-S, et al. “Flexible glucose sensor using CVD-grown graphene-based field effect transistor,” Biosensors and Bioelectronics. Vol. 37, pp. 82-87, 2012.

[130] Wang B, Luo Y, Gao L, Liu B, and Duan G. “High-performance field-effect transistor glucose biosensors based on bimetallic Ni/Cu metal-organic frameworks,” Biosensors and Bioelectronics. Vol. 171, pp. 112736, 2021.

[131] Farahmandpour M, Haghshenas H, and Kordrostami Z. “Blood glucose sensing by back gated transistor strips sensitized by CuO hollow spheres and rGO,” Scientific Reports, Vol. 12, pp. 21872, 2022.

[132] Archana R, Sreeja B, Nagarajan K, Radha S, BalajiBhargav P, Balaji C, et al. “Development of highly sensitive Ag NPs decorated graphene FET sensor for detection of glucose concentration,” Journal of Inorganic and Organometallic Polymers and Materials. Vol. 30, pp. 3818-3825, 2020.

[133] M. Farahmandpour, Z. Kordrostami, M. Rajabzadeh, and R. Khalifeh, “Flexible Bio-Electronic Hybrid Metal-Oxide Channel FET as a Glucose Sensor,” IEEE Transactions on NanoBioscience. 2023.

[134] K. Koike, T. Sasaki, K. Hiraki, K. Ike, Y. Hirofuji, and M. Yano. "Characteristics of an extended gate field-effect transistor for glucose sensing using an enzyme-containing silk fibroin membrane as the bio-chemical component," Biosensors. Vol. 10, pp. 57, 2020.

[135] JW. Park, C. Lee, and J. Jang, "High-performance field-effect transistor-type glucose biosensor based on nanohybrids of carboxylated polypyrrole nanotube wrapped graphene sheet transducer," Sensors and Actuators B: Chemical. Vol. 208, pp. 532-537, 2015.

[136] Das M, Chakraborty T, Lin CY, Lin R-M, and Kao CH. "Screen-printed Ga2O3 thin film derived from liquid metal employed in highly sensitive pH and non-enzymatic glucose recognition," Materials Chemistry and Physics. Vol. 278, pp.125652, 2022.

[137] Forzani ES, Zhang H, Nagahara LA, Amlani I, Tsui R, and Tao N. "A conducting polymer nanojunction sensor for glucose detection," Nano Letters. Vol. 4, pp. 1785-1788, 2004.

[138] H. Yoon, S. Ko, and J. Jang, "Field-effect-transistor sensor based on enzyme-functionalized polypyrrole nanotubes for glucose detection," The Journal of Physical Chemistry B. vol. 112, pp. 9992-9997, 2008.

[139] Huang Y, Dong X, Shi Y, Li CM, Li L-J, and Chen P. "Nanoelectronic biosensors based on CVD grown graphene," Nanoscale. Vol. 2, pp. 1485-1488, 2010.

[140] Wu Y-L, Hsu P-Y, and Lin J-J. "Polysilicon wire glucose sensor highly immune to interference," Biosensors and Bioelectronics. Vol. 26, pp. 2281-2286, 2011.

[141] Luo X-L, Xu J-J, Zhao W, Chen H-Y. Glucose biosensor based on ENFET doped with SiO2 nanoparticles. Sensors and Actuators B: Chemical. Vol. 97, pp. 249-255, 2004.

[142] Tomari N, Sasamoto K, Sakai H, Tani T, Yamamoto Y, and Nishiya Y. "New enzymatic assays based on the combination of signal accumulation type of ion sensitive field effect transistor (SA-ISFET) with horseradish peroxidase," Analytical biochemistry. Vol. 584, pp. 113353, 2019.

[143] MS. Andrianova, VP. Grudtsov, NV. Komarova, EV. Kuznetsov, and AE. Kuznetsov, "ISFET-based aptasensor for thrombin detection using horseradish peroxidase," Procedia engineering. Vol. 174, pp. 1084-1092, 2017.

[144] AA. Shul'ga and TD. Gibson, "An alternative microbiosensor for hydrogen peroxide based on an enzyme field effect transistor with a fast response," Analytica chimica acta. Vol. 296, pp. 163-170, 1994.

[145] V. Volotovsky and N. Kim, "Multienzyme inhibition biosensor for amygdalin measurement," Electroanalysis: An International Journal Devoted to Fundamental and Practical Aspects of Electroanalysis. Vol. 10, pp. 512-514, 1998.

[146] V. Volotovsky and N. Kim. "Cyanide determination by an ISFET-based peroxidase biosensor," Biosensors and Bioelectronics. Vol. 13, pp. 1029-1033, 1998.

[147] V. Volotovsky and N. Kim, "Determination of glucose, ascorbic and citric acids by two-ISFET multienzyme sensor," Sensors and Actuators B: Chemical. Vol. 49, pp. 253-257, 1998.

[148] Starodub N, Dzantiev B, Starodub V, and Zherdev A. "Immunosensor for the determination of the herbicide simazine based on an ion-selective field-effect transistor," Analytica Chimica Acta. Vol. 424, pp. 37-43, 2000.

[149] Z. Wang, H. Yu, and Z. Zhao, "Silk fibroin hydrogel encapsulated graphene filed-effect transistors as enzyme-based biosensors," Microchemical Journal. Vol. 169, pp. 106585, 2021.

[150] MA. Barik, MK. Sarma, C. Sarkar, and JC. Dutta, "Highly sensitive potassium-doped polypyrrole/carbon nanotube-based enzyme field effect transistor (ENFET) for cholesterol detection," Applied biochemistry and biotechnology. Vol. 174, pp. 1104-1114, 2014.

[151] H. Suzuki and Y. Matsugi, "Integrated microfluidic system for the simultaneous determination of ammonia, creatinine, and urea," Sensors and Actuators B: Chemical. Vol. 108, pp. 700-707, 2005.

[152] M. Jurkiewicz, S. Alegret, J. Almirall, M. Garcia, E. Fabregas, "Development of a biparametric bioanalyser for creatinine and urea," Validation of the determination of biochemical parameters associated with hemodialysis. Analyst. Vol. 123, pp. 1321-1327, 1998.

[153] Wesoły M, Cetó X, Del Valle M, Ciosek P, and Wróblewski W. "Quantitative analysis of active pharmaceutical ingredients (APIs) using a potentiometric electronic tongue in a SIA flow system," Electroanalysis. Vol. 28, pp. 626-632, 2016.

[154] Ebrahimi S, Nataj ZE, Khodaverdian S, Khamsavi A, Abdi Y, and Khajeh K. "An ion-sensitive field-effect transistor biosensor based on SWCNT and aligned MWCNTs for detection of ABTS," IEEE Sensors Journal. Vol. 20, pp. 14590-14597, 2020.

[155] Bi Y, Ye L, Mao Y, Wang L, Qu H, Liu J, et al. "Porous carbon supported nanoceria derived from one step in situ pyrolysis of Jerusalem artichoke stalk for functionalization of solution-gated graphene transistors for real-time detection of lactic acid from cancer cell metabolism," Biosensors and Bioelectronics. Vol. 140, pp. 111271, 2019.

[156] Kotsakis SD, Miliotis G, Tzelepi E, Tzouvelekis LS, and Miriagou V. "Detection of carbapenemase producing enterobacteria using an ion sensitive field effect transistor sensor," Scientific Reports. Vol. 11, pp. 1-14, 2021.

[157] G. Keshwani, JC. Dutta, "CNT based high-κ dielectric Ion Sensitive Field Effect Transistor Based Cholesterol Biosensor," Current Trends in Biotechnology and Pharmacy. Vol. 15, pp. 182-188, 2021.

[158] P-Y. Kuo, Y-Y. Chen, W-H. Lai, and C-H. Chang, "An extended-gate field-effect transistor applied to resistive divider integrated with the readout circuit using 180nm CMOS process for uric acid detection," IEEE Sensors Journal. Vol. 21, pp. 20229-20238, 2021.

[159] Liu N, Xiang X, Fu L, Cao Q, Huang R, Liu H, et al. "Regenerative field effect transistor biosensor for in vivo monitoring of dopamine in fish brains," Biosensors and Bioelectronics. Vol. 188, pp. 113340, 2021.

[160] T-M. Pan and C-H. Lin, "High Performance NiOx Extended-Gate Field-Effect Transistor Biosensor for Detection of Uric Acid," Journal of The Electrochemical Society. Vol. 168, pp. 017511, 2021.

[161] Jang H-J, Ahn J, Kim M-G, Shin Y-B, Jeun M, Cho W-J, et al. "Electrical signaling of enzyme-linked immunosorbent assays with an ion-sensitive field-effect transistor," Biosensors and Bioelectronics. Vol. 64, pp. 318-323, 2015.

[162] O. Kutova, M. Dusheiko, NI. Klyui, and VA. Skryshevsky, "C-reactive protein detection based on ISFET structure with gate dielectric SiO2-CeO2," Microelectronic Engineering. Vol. 215, pp. 110993, 2019.

[163] AE. Kuznetsov, NV. Komarova, EV. Kuznetsov, MS. Andrianova, VP. Grudtsov, EN. Rybachek, et al. "Integration of a field effect transistor-based aptasensor under a hydrophobic membrane for bioelectronic nose applications," Biosensors and Bioelectronics. Vol. 129, pp. 29-35, 2019.

[164] R. Campos, J. Borme, and JR. Guerreiro, Jr G. Machado,MFt. Cerqueira, DY. Petrovykh, et al. "Attomolar label-free detection of DNA hybridization with electrolyte-gated graphene field-effect transistors," ACS sensors. Vol. 4, pp. 286-293, 2019.

THIS PAGE IS INTENTIONALLY LEFT BLANK.

IJBBE International Journal of Biophotonics & Biomedical Engineering Vol. 4, No. 1, Spring-Summer, 2024

Research Article

Simulation-based Optimization of Chemotherapeutic Drug Dosage: An Agent-based Q-learning Approach

H. Sadrian [a], P. Vafadoost [a], A. Hajipour [a] and H. Rokhsati [b]

---

a Biomedical Engineering Department, Electrical and Computer Faculty, Hakim Sabzevari University, Sabzevar, Iran
b Department of Computer, Control and Management Engineering, Sapienza University of Rome, Italy

---

***Corresponding Author Email: peymanvafadoost@gmail.com**

DOI: 10.71498/ijbbe.2024.1127216

ABSTRACT

Received: Jul. 26, 2024, Revised: Sep. 20, 2024, Accepted: Oct. 8, 2024, Available Online: Jan. 19, 2025

Cancer is indeed a growing concern worldwide for human health and existence, with its prevalence and impact on individuals and society increasing. The main objective of this article is to control and optimize drug dosage in order to prevent the uncontrollable growth of cancer cells and also restore the patient's immune cells to normal levels at the end of the training process, in such a way that the disease can be controlled in the early days of treatment. Reinforcement learning methods are widely applied in many domains nowadays and have attracted researchers' interest in conducting studies in this field. Therefore, in this article, specifically we also use the Q-learning method, one of the most famous model-free reinforcement learning methods, as well as the four-state nonlinear dynamic model called depillis, to simulate and design the proposed controller. The proposed controller's performance was evaluated in the presence of noise in three stages (training, simulation, and both stages simultaneously) as well as in the presence of uncertainty in one of the parameters of the depillis model. In a state of uncertainty, a combination therapy of chemotherapy and immunotherapy has been suggested as a treatment approach. Results indicate the significant impact of the proposed controller in determining the optimal drug dosage, improved accuracy, reduced side effects, and faster convergence compared to previous studies.

KEYWORD

Cancer, Control, Reinforcement Learning, Q-Learning.

I. INTRODUCTION

Cancer is recognized as one of the biggest threats and growing concerns worldwide, with various types of it being characterized by a phenomenon called cellular state change with the loss of control over cell division and proliferation. However, cancer is an abnormal, irregular, uncontrolled, and deadly growth of cells in the body's tissues, leading to the formation of a mass called a tumor. The American Cancer Society (ACS) collects the latest information and reports each year on the incidence, mortality, and outcomes of cancer in collaboration with two centers called the Central Cancer Registry and the National

Center for Health Statistics [1]. According to the World Health Organization (WHO), the projected data from 2030 to 2040 is concerning. It suggests that around 11.2 to 13.4 million individuals may die from this illness by 2030, and by 2040, approximately 27.5 million people will be affected by it [2]. The treatment plan and amount of medication given depend on the tumor stage (the stage of the tumor refers to how advanced it is and whether it has spread to other parts of the body), patient's weight, immunity level (white blood cell count), any existing illnesses, organ function, drug interactions, and the patient's age [3]. Based on these factors, the healthcare provider will determine the most appropriate treatment plan, which may include surgery, radiation therapy, chemotherapy, targeted therapy, immunotherapy, or a combination of these approaches. The dosage and type of medication given will also depend on these factors. It is important for the healthcare team to assess these factors and create an individualized treatment plan for each patient to optimize their chances of successful treatment while considering their specific circumstances. Given the severity of cancer, any method that improves the effectiveness of treatment, leading to decreased harm to organs and lower rates of morbidity, is highly sought after.

Implementing reinforcement learning techniques can help mitigate complications and address time constraints associated with administering chemotherapy in cancer treatment [4].

Chemotherapy is a crucial component of cancer treatment, but it is not without its challenges. In addition to targeting cancer cells, chemotherapy can also affect healthy cells, leading to various side effects such as fatigue, nausea, hair loss, and a weakened immune system. Furthermore, there may be limitations in terms of the duration and frequency of chemotherapy sessions, as well as the tolerance level of patients to the treatment. Despite these complexities and drawbacks, chemotherapy remains a valuable therapeutic tool in the fight against cancer, often used in conjunction with other treatments to achieve the best possible outcomes for patients [5]. Control theory, a branch of mathematics and engineering that deals with the behavior of dynamical systems, has recently been proposed as a potential tool to improve the efficacy of cancer chemotherapy [6].

In the modern world, mathematical models play a crucial role in understanding and optimizing cancer treatment strategies. These models help researchers and clinicians simulate the complex dynamics of tumor growth, drug interactions, and treatment response, allowing for personalized and precise approaches to therapy. By incorporating data-driven mathematical simulations, healthcare professionals can tailor cancer treatments to individual patients, predict outcomes, optimize drug dosages, and explore novel therapeutic interventions. Overall, mathematical modeling has revolutionized the field of cancer treatment by providing valuable insights and guiding decision-making processes to improve patient outcomes and quality of care [7,8]. A cancer dynamics model needs to take into consideration the growth of the tumor, the response of the immune system to the tumor growth, and the impact of chemotherapy on immune cells, normal cells, and tumor growth [3]. In summary, utilizing mathematical models to control and optimize chemotherapy drug dosage enables precision medicine, predicts drug response, optimizes treatment schedules, reduces trial and error, and enhances safety and efficacy in cancer therapy.

Reinforcement learning has shown promise in the field of chemotherapy drug control and optimization. Chemotherapy treatment often involves dosing medications at specific intervals and monitoring the patient's response to determine the effectiveness of the treatment. This process can be complex and time-consuming, requiring constant adjustments to ensure the patient is receiving the right dosage and that side effects are managed effectively.

Reinforcement learning algorithms can be used to optimize chemotherapy drug control by learning from past treatment outcomes and adjusting dosages in real time based on patient response. These algorithms can also take into account individual patient characteristics, such as age, weight, and genetic factors, to tailor treatment plans to each patient's unique needs.

By using reinforcement learning in chemotherapy drug control, healthcare providers can potentially improve treatment outcomes, reduce side effects, and optimize drug dosages more efficiently. This can result in better patient outcomes, reduced healthcare costs, and a more personalized approach to cancer treatment. The study shows promising results in optimizing drug dosing for cancer chemotherapy treatment using RL, which could potentially improve patient outcomes and reduce side effects.

Modeling and controlling the growth of cancer cells as well as determining the optimal drug dosage in cancer patients are challenging and complex subjects in the field of cancer.

In [3, 9, 10, 11, 12] and [13] predominantly reinforcement learning methods have been used for cancer control and treatment. Specifically, in [3] Padmanabhan and her colleagues have suggested a closed-loop controller based on reinforcement learning in their work. They utilize Q-learning with a four-state mathematical model for cancer chemotherapy, which includes immune cells, normal cells, tumor cells, and drug concentration. The simulation of three disease ranges shows that the injected drug dose effectively eliminates the tumor. One notable advantage of their method is that it does not require a system model to create a controller. In another study by Padmanaban and colleagues [13], mentioned in Chapter 9 of the book "Control Applications for Biomedical Engineering Systems" [14], researchers have focused on investigating reinforcement learning-based control of drug dosing with applications in anesthesia and cancer treatment. The main goal is to determine and control the intravenous dosage of the anesthetic drug using a reinforcement learning algorithm called Q-learning. The drug used in this study is propofol for patients in the ICU, which is regulated by the Q-learning algorithm. The study demonstrated the efficacy of the Q-learning algorithm in regulating the dosage of propofol for patients undergoing treatment. The authors demonstrate the effectiveness of the proposed approach through simulations and experiments, showing promising results in terms of improved treatment outcomes and reduced drug toxicity. In [9], researchers have proposed an optimal switching control strategy for drug therapy process in cancer chemotherapy. The proposed control algorithm dynamically adjusts the dosage and type of drugs administered based on real-time patient response data, tumor progression, and toxicity levels. The objective of the switching control is to maximize the therapeutic benefits by targeting the tumor cells while minimizing the detrimental effects on healthy tissues. A mathematical model of the tumor growth dynamics and drug pharmacokinetics is developed to simulate the patient's response to the treatment. The control algorithm incorporates a multi-objective optimization framework to simultaneously consider the trade-offs between tumor regression, toxicity reduction, and drug resistance. Simulation results demonstrate that the optimal switching control strategy outperforms traditional fixed-dose protocols in terms of tumor suppression and patient survival rates.

In [10], researchers have proposed a novel approach to optimizing dose-finding strategies using integral reinforcement learning. The aim is to develop a control algorithm that can adaptively adjust drug dosages based on patient responses to maximize efficacy while minimizing side effects. In particular, the use of integral reinforcement learning allows the algorithm to incorporate past experiences and account for the long-term effects of drug dosing decisions. This helps in fine-tuning the dosing strategy over time to achieve the best possible outcomes for patients. In [11], a novel approach for controlling tumor growth under anti-angiogenic therapy using reinforcement learning algorithms (RL) has been proposed. Anti-angiogenic therapy is a promising strategy for cancer treatment that aims to inhibit the growth of blood vessels that supply nutrients to tumors. However, this therapy is often plagued by the development of resistance and rebound effects, leading to tumor regrowth. Overall, this study highlights the potential of using reinforcement learning techniques to optimize cancer treatment strategies and improve outcomes for patients undergoing anti-angiogenic therapy. In [12] authors have presented a supervised offline reinforcement learning approach for personalizing chemotherapy regimens for cancer patients. Offline reinforcement learning is a machine learning technique that allows for the optimization of treatment strategies based on historical data without the need for real-time feedback. First, a Markov Decision Process (MDP) framework is constructed for modeling the chemotherapy treatment process. The state space of the MDP includes patient and tumor characteristics, while the action space represents the chemotherapy drugs and doses that can be administered. The reward function captures the efficacy and toxicity of the treatment, with the goal of maximizing the former while minimizing the latter. Next, a deep Q-network (DQN) was trained using a dataset of historical patient records and treatment outcomes. The DQN learns to predict the optimal chemotherapy regimen for a given patient based on their individual characteristics and tumor type. By leveraging the rich information contained in the dataset, the model is able to generalize well to new patients and make personalized treatment recommendations. Overall, this study showcases the promise of supervised offline reinforcement learning for personalizing chemotherapy treatment decisions.

Melanoma is a type of skin cancer that can be challenging to treat due to its aggressive nature and tendency to spread rapidly. Traditional cancer therapies often have toxic side effects that can be detrimental to patient health. In [15], Noori et al introduced the use of an eligibility traces algorithm to determine the optimal dose for controlling the population of cancer cells in melanoma patients. The eligibility traces algorithm is a reinforcement learning technique that allows for efficient learning from past experiences by assigning credit to actions that lead to positive outcomes. By applying this algorithm to the problem of determining the optimal dosage for cancer treatment, aim to identify a treatment regimen that maximizes anti-cancer effects while minimizing the occurrence of side effects.

In [16], the authors also presented a novel approach to controlling cancer cells in a nonlinear model of melanoma by incorporating the uncertainty factor using the Q-learning algorithm under the Case-Based Reasoning (CBR) policy. The use of CBR policy allows us to make decisions based on past experiences and cases, enabling us to leverage the knowledge gained from previous treatments and outcomes to improve our current control strategies. By combining the Q-learning algorithm with the CBR policy, we can develop a robust and adaptive approach to controlling cancer cells in a nonlinear model of melanoma.

Fuzzy logic is used to model the uncertainty and imprecision in the feedback signals from the tumor growth dynamics. The fuzzy logic controller provides a flexible and adaptive strategy for adjusting the chemotherapy drug dose based on the tumor's current state. Based on this, authors in [17] have proposed a new feedback control strategy for regulating tumor growth by limiting the maximum dose of chemotherapy using fuzzy logic. The proposed control system uses reinforcement learning to learn the optimal dose of chemotherapy drug to administer at each time step based on feedback from the tumor growth dynamics. The system is designed to minimize tumor growth while also limiting the maximum dose of chemotherapy drugs to prevent harmful side effects on the patient.

There are many reasons to use reinforcement learning methods, some of which include:

1. Flexibility: Reinforcement learning methods can be applied to a wide variety of tasks and environments, making them flexible and adaptable for different scenarios.

2. Ability to learn from interactions: Reinforcement learning algorithms learn from trial and error by interacting with an

environment, enabling them to improve performance over time through experience.

3. Autonomous decision-making: Reinforcement learning methods enable machines to make autonomous decisions without the need for explicit programming, allowing them to adapt to changing conditions and learn from their mistakes.

4. Handling complex, dynamic environments: Reinforcement learning methods are well-suited for addressing problems in complex, dynamic environments where traditional algorithms may struggle, such as in robotics, autonomous driving, and game playing.

5. Scalability: Reinforcement learning algorithms can be scaled up to handle large amounts of data and complex tasks, making them suitable for real-world applications in fields like healthcare, finance, and transportation.

6. Continuous learning: Reinforcement learning algorithms can continuously learn and adapt to new information and changing conditions, allowing them to improve performance over time.

7. Model-free learning: Reinforcement learning methods do not require explicit models of the environment, making them suitable for situations where the underlying dynamics are unknown or difficult to model accurately.

Reinforcement learning can be used in the application of cancer chemotherapy drug dosage to optimize treatment outcomes and minimize side effects for patients. In this scenario, the chemotherapy dosage would be considered as the action taken by the system, and the outcome of the treatment, such as tumor size reduction and patient's quality of life, would be the reward signal. The reinforcement learning algorithm would learn from the feedback of previous treatments to adjust the dosage levels in subsequent rounds, aiming to find the optimal dosage that maximizes the treatment benefits while minimizing the negative side effects. By utilizing reinforcement learning in cancer chemotherapy drug dosage, oncologists can personalize treatment strategies for individual patients based on their response to the treatment, ultimately leading to better outcomes and improved patient care.

This article is a review on the application of using Q-learning method, one of the reinforcement learning methods, in determining and controlling the dosage of chemotherapeutic drugs. In the following sections of this article, we will delve into a comprehensive examination of reinforcement learning concepts, particularly focusing on the Q-learning method.

This article is structured in 3 sections: materials and methods, Results and discussion and conclusions.

II. MATERIALS AND METHODS

This section outlines the mathematical model of depillis pharmacology, which is used to analyze the effectiveness of chemotherapy in treating cancer. It introduces the concept of reinforcement learning and describes how a controller is created using Q-learning to calculate and regulate the best dosage of medication for chemotherapy.

A. *Mathematical Model*

So far, a large number of mathematical models have been proposed for the growth of cancer cells, each of which has its advantages and disadvantages, and in fact, there is no correct answer as to which model is more realistic [7, 8]. Mathematical models serve as valuable instruments in grasping the underlying mechanics of dynamic processes within cancer and are essential for investigating a wide range of scientific inquiries. The human body can be represented by a mathematical model, which can efficiently simulate complex systems at low costs. These models are useful for predicting the growth and spread of cancer cells, understanding the immune system's response, evaluating the impact of different cancer treatments, and assessing drug toxicity on healthy tissues. They can also help in studying the interactions between various factors that contribute to tumor formation and predicting tumor size. By developing control models based on these mathematical models, we can improve drug prescription for cancer patients. A well-fitted mathematical model of cancer cell growth can provide valuable insights for analyzing the system accurately.

Mathematical modeling can be applied to different aspects of cancer research, including tumor growth, mutations, metastasis, treatment methods like chemotherapy and immunotherapy, and the diversity of tumors. This is typically done through the use of differential equations for analytical simulation and modeling purposes [18,19].

The depillis model is a mathematical model used in epidemiology to simulate the spread of infectious diseases within a population. This model is one of the most comprehensive models proposed in the field of chemotherapy; because the reason and importance of using this model is the addition and impact of the drug on the expression of immune cells. In depillis mathematical model, the dynamics of normal cells, tumor cells, immune cells and drug concentration can be represented by a system of differential equations [3].

Let $N(t)$ be the population of normal cells at time t, $T(t)$ be the population of tumor cells at time t, $I(t)$ be the population of immune cells at time t, and $D(t)$ be the concentration of drug at time t. The model can be described by the following equations:

$$\frac{dI}{dt}(t) = s + \frac{\rho I(t)T(t)}{\alpha + T(t)} - d_1 I(t) - c_1 I(t)T(t) - a_1(1 - e^{-D(t)})I(t)$$

$$\frac{dT}{dt}(t) = r_1 T(t)\big(1 - b_1 T(t)\big) - c_2 I(t)T(t) - c_3 N(t)T(t) - a_2(1 - e^{-D(t)})T(t) \qquad (1)$$

$$\frac{dN}{dt}(t) = r_2 N(t)\big(1 - b_2 N(t)\big) - c_4 N(t)T(t) - a_3(1 - e^{-D(t)})N(t)$$

$$\frac{dD}{dt}(t) = -d_U D(t) + u(t)$$

This model takes into account various factors such as the growth rate of the cancer cells, the effectiveness of the chemotherapy drugs, and the impact on the immune system. By varying the parameters in the model, researchers can predict how different treatment strategies will affect tumor growth and the overall outcome for the patient. The values of the parameters of this model are also shown in table 1.

Depillis' model has been used to study optimal drug dosing regimens, the development of drug resistance, and the potential for combination therapies to improve treatment outcomes. By incorporating mathematical modeling into cancer research, scientists can better understand the complex interactions between cancer cells, chemotherapy drugs, and the immune system, ultimately leading to more effective treatment options for patients.

B. *Reinforcement learning*

Reinforcement learning, an exciting concept in machine learning, is rapidly progressing and is set to be a major advancement in artificial intelligence in the coming years. Reinforcement learning involves a machine learning method where an agent learns to make decisions through receiving feedback from its actions within an environment. The schematic of reinforcement learning operation is shown in Fig. 1.

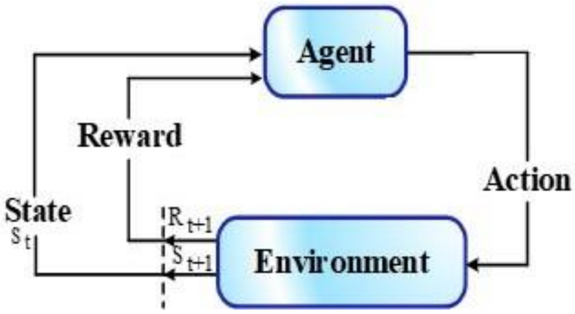

Fig. **1** Schematic of reinforcement learning operation.

The agent performs actions within the environment, receives either rewards or penalties as feedback, and adapts its behavior to maximize its rewards gradually. This process is rooted in the concept of trial-and-error learning, as the agent gains knowledge through practice and by engaging with its surroundings. This approach has shown promising results in various domains, such as game-playing, robotics, and autonomous driving [20,21]. By allowing agents to learn directly from interacting with their environment, reinforcement learning has the potential to create more autonomous and intelligent systems that can adapt to new situations and learn complex tasks without explicit programming.

Types of reinforcement learning methods include Value-based methods, Policy-based methods, Model-based methods, Model-free methods, Actor-critic methods, multi-agent reinforcement learning methods and Hierarchical reinforcement learning methods. The method proposed in this article is among value-based methods. These methods involve estimating the value of state-action pairs to make decisions on which actions to take. The value of an action is typically defined as the expected cumulative reward that an agent can achieve by taking that action and following a certain policy thereafter. Overall, value-based methods in reinforcement learning are powerful techniques for learning optimal policies in environments with discrete or continuous action spaces. They provide a fundamental framework for understanding the trade-offs between different actions and guiding the agent towards achieving its goals. An example of value-based methods used is Q-learning.

TABLE **1** PARAMETER VALUES OF THE DEPILLIS CHEMOTHERAPEUTIC MODEL [22].

Parameter	**Value**	**Description**
a_1	0.2	Fractional immune cell kill rate
a_2	0.3	Fractional tumor cell kill rate
a_3	0.1	Fractional normal cell kill rate
b_1	1	Reciprocal carrying capacity of tumor cells
b_2	1	Reciprocal carrying capacity of normal cells
c_1	1	Immune cell competition term (competition between tumor cells and immune cells)
c_2	0.5	Tumor cell competition term (competition between tumor cells and immune cells)
c_3	1	Tumor cell competition term (competition between normal cells and tumor cells)
c_4	1	Normal cell competition term (competition between normal cells and tumor cells)
r_1	1.5	Per unit growth rate of tumor cells
r_2	1	Per unit growth rate of normal cells
d_1	0.2	Immune cell death rate
dU	1	Decay rate of injected drug
s	0.33	Immune cell influx rate
ρ	0.01	Immune response rate
α	0.3	Immune threshold rate

C. *Q-learning*

In Q-learning, an agent learns the value of each action in each state by updating a Q-table with learned rewards from interactions with the environment. The agent then selects actions based on the values in the Q-table [23]. Some of the key features of the Q-learning method include:

1. Model-free: Q-learning is a model-free reinforcement learning algorithm, meaning that it does not require knowledge of the underlying dynamics of the environment. Instead, the agent learns through trial and error by interacting with the environment and updating its Q-values based on the rewards it receives.

2. Q-values: In Q-learning, the agent maintains a Q-table that stores the expected rewards for each action in each state. The Q-value for a

particular state-action pair represents the expected cumulative reward that the agent will receive if it takes that action in that state and follows the optimal policy thereafter.

3. Exploration vs exploitation: To balance exploration (trying new actions to discover the optimal policy) and exploitation (taking the best-known action to maximize rewards), Q-learning uses an epsilon-greedy strategy. This means that the agent will choose a random action with probability epsilon and the best-known action with probability 1-epsilon.
4. Bellman equation: Q-learning updates its Q-values using the Bellman equation, which states that the expected cumulative reward for a state-action pair should be equal to the immediate reward obtained by taking that action plus the expected cumulative reward of the next state-action pair.
5. Convergence: Q Learning is guaranteed to converge to the optimal policy under certain conditions, such as having a finite state and action space, and that the agent visits all state-action pairs infinitely often.
6. Off-policy: Q-learning is an off-policy algorithm, meaning that it can learn from any policy, not just the one it follows. This property allows the agent to learn from past experience and improve its policy over time.
7. Suitable for discrete actions: Q-learning is best suited for environments with a discrete action space, as it requires calculating Q-values for each possible action in each state. For continuous action spaces, techniques such as Deep Q-learning are typically used.

Overall, Q-learning is a versatile and effective reinforcement learning algorithm that has been successfully applied to a wide range of problems, including game playing, robotics, and autonomous driving [23].

In the Q-learning algorithm process, it learns the Q-value function $Q(s,a)$; meaning how to take action "a" in a specific state "s". The goal of the agent in Q-learning is to maximize the Q-value, ultimately leading to the most optimal decision-making process. The value of Q-learning is obtained using the Bellman equation. The Bellman equation is expressed as follows:

$$V(s) = \max\left[R(s,a) + \gamma \sum_{s'} P(s'|s,a)V(s')\right] \tag{2}$$

In Fig. 2, we have shown the steps of executing the Q-learning algorithm in the form of a flowchart:

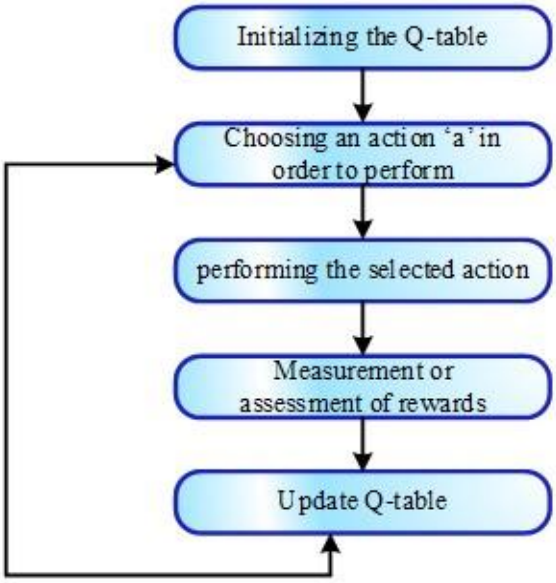

Fig. **2** Flowchart of the steps of implementing the Q-Learning algorithm.

Updating the Q-table is done by equation 3:

$$Q(s,a) = Q(s,a) + \alpha[R(s,a) + \gamma maxQ'(s',a')] \tag{3}$$

In the above equation, α is the learning rate, γ is the discount factor, and $maxQ'(s',a')$ represents the maximum Q value of the next state. Following the flowchart of the Q-learning algorithm in Fig. 3, in the second step, the agent must choose an action according to a policy that balances exploitation (using previously known information to maximize reward) and exploration (finding more information about the environment). This policy selection is done through two common methods: empirical search and random policy. Typically, the idea and method used in this algorithm are based on empirical search and the epsilon-greedy strategy; this is because the agent increases its confidence in finding the optimal solution by exploring the environment more. This method usually selects the action that is estimated to have the highest reward in most cases. In the next section, we investigate the design of a Q-learning-based controller for determining the optimum drug dosage in cancer and then present the relevant results.

D. *Depilis model review and controller design*

Understanding the dynamics of the model in order to determine the equilibrium points of the system and their stability is necessary; therefore, equilibrium points without tumor that are stable in the limited treatment time are defined as follows [17]:

$$(\frac{1}{b_2}, 0, \frac{s}{d_1}) \tag{4}$$

As it is evident, at this point, there are zero tumor cells and immune and normal cells present. The point achieved will be under our ultimate goal at the end of chemotherapy [17]:

$$(N, T, I) \rightarrow (1,0,1.65) \tag{5}$$

Using the dynamic model of depillis and with the help of the Q-learning algorithm, we design a controller to minimize or eliminate tumor cells (reduce tumor volume or eradicate it) and also maintain immune cells at a certain level.

Our environment is an optimal drug dosing control system in cancer patients, where tumor cells and immune cells are considered as system states, and the amount of prescribed drug dose is considered as the system action. The drug dose amount in the current research is specified in the range [0,1]. Therefore, our state space in this research is a two-dimensional state space. In the training stage for determining states, we define a range where this range is defined as 0+0.3×rand() for tumor cells and 0.15+(2-0.15)×rand() for immune cells; meaning that for tumor cells, a random number between 0 to 0.3 and for immune cells, a random number between 0.15 to 2 is chosen. Then, based on the division of state space for these two variables and the formation of a Q-table in each generation of current state values, one of the states in the table is selected. In order to evaluate the reward, the following method was used:

$$\begin{cases} if\ tumor\ cell = 0, r = 10, \\ \quad otherwise, r = 1. \end{cases} \tag{6}$$

In this way, in each iteration, the values of Q-table are completed and updated, and eventually, the complete table is obtained. After completing the table and also determining the specific initial states for normal, tumor, and immune cells, the training process continues until the end of the training, where the number of cancer cells reaches a minimum or zero and the immune and normal cells also reach a specified desired level.

Initial conditions are also defined for three normal, tumor, and immune cells as 1, 0.25, and 0.15, respectively. The values of Q-learning parameters are defined according to the table below:

Table **2** Reinforcement learning parameters.

Parameter	**Value**	**Description**
γ	0.8	Discount factor
η	0.2	Learning rate
ε	0.05	Greedy learning parameter

III. SIMULATION

For simulation purposes, we first examine the model without the impact of the drug; for this purpose, using the mathematical equations of the depillis model and also the parameters in Table 1, we observe the changes obtained in the absence of drug effect, and then by entering the drug, we focus on controlling and determining the optimal drug dose in the chemotherapy process for cancer patients using the Q-learning method. Therefore, in order to display the chart of the change, we first convert the depillis model equations according to the relationships

(1) to (4), which are continuous, to discrete. With high precision in discretization, the output results of the graph should be similar to the original model results [3]. The chart of changes in the discretized model in the absence of drug influence is shown in Fig. 3.

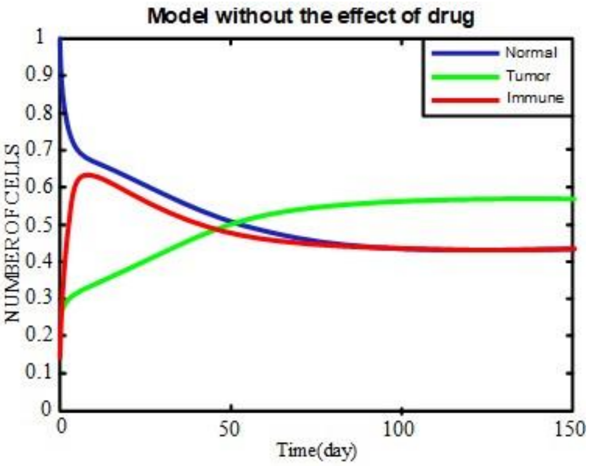

Fig. **3** Discretization model in the absence of drug effect.

As seen in Fig. 3, in the early stages of cancer cell growth in the patient's body, immune cells try to fight against cancer cells, but over time, due to the weakening of the immune cells, cancer cells grow and multiply more and more until they cover the entire surface of the curve and system; furthermore, immune and normal cells quickly reach their lowest vital limit and, in this situation, the patient will lose their life [22].

Now we need to simulate the model in the presence of drug input using the q-learning method. As mentioned earlier, we use the epsilon-greedy method to determine the optimal drug dose, in this method, due to the use of the rand() function, we will observe different results in the output. In this method, usually the experiment is conducted for 10 different scenarios and then the average of these 10 scenarios is calculated. However, the important point is that taking 10 runs and averaging the results is only valid under the assumption that we can fully complete table Q; whereas in implementation, with a higher number of training iterations (assuming a total of 10,000 episodes), there will be no need for multiple runs. When we want to use the learned Q-table for simulation, there is no longer a random state; this is because the Q-table has been ideally or close to ideally trained during the training phase. Therefore, the small difference observed in each execution of the program is the result of using the same ε-greedy method in the training phase. The following figures display various types of simulated charts using the Q-learning method:

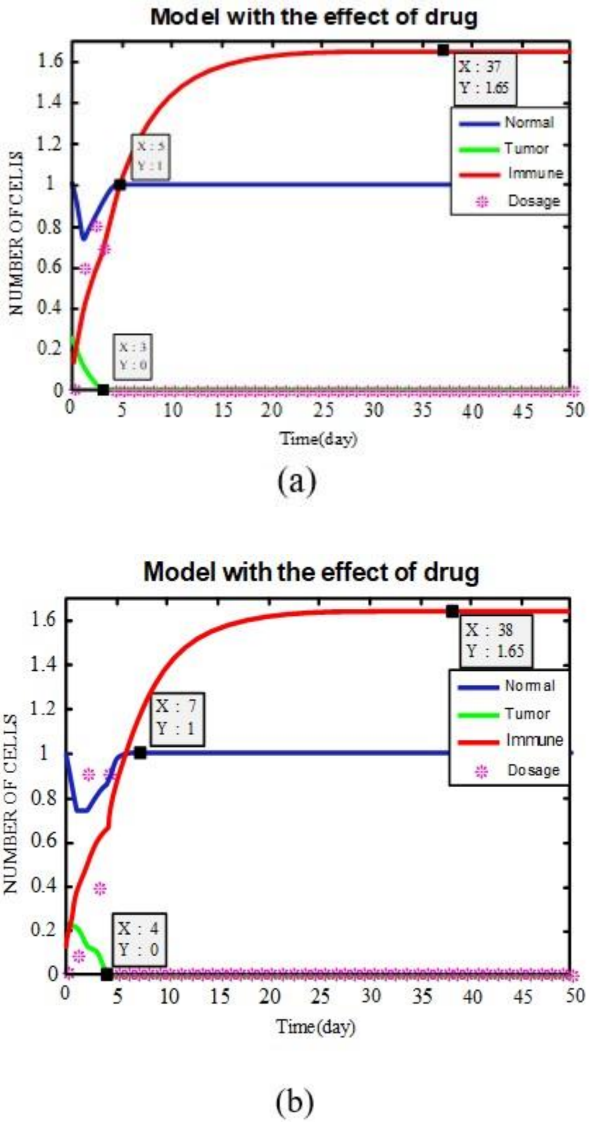

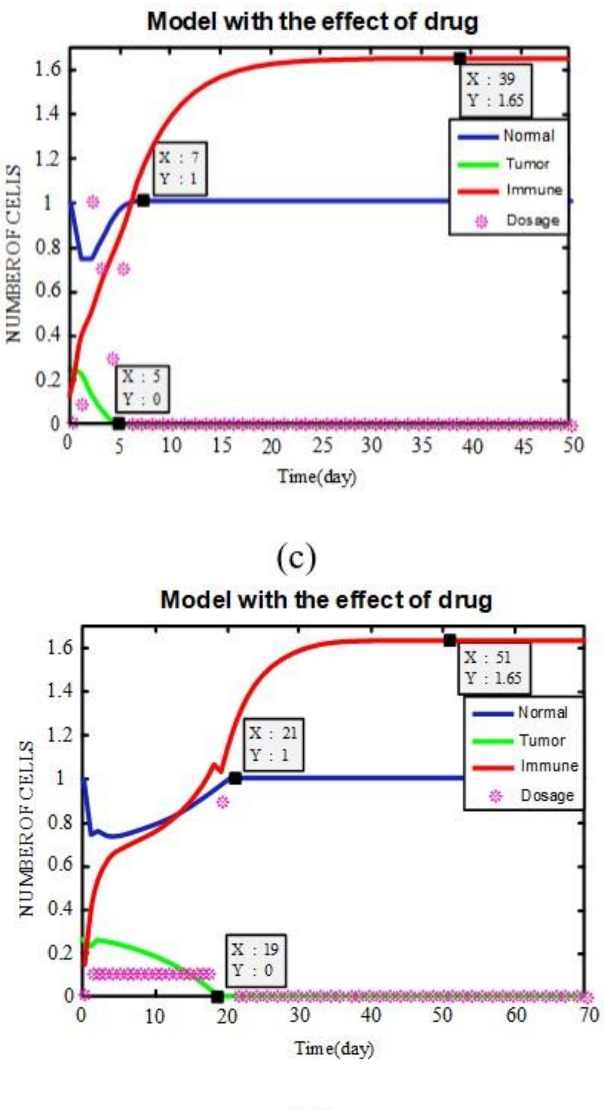

(c)

(d)

Fig. **4** (a,b,c,d) Optimal control of model with Q-learning algorithm in the presence of drug influence.

Figure 4 diagrams all represent optimal control of cancer drug dosage using the q-learning method; however, as it is evident, a slight difference in each execution can be seen in the diagrams, which is the effect of using the ε-greedy method in the training phase. Furthermore, changing the input range of tumor and immune cells at the beginning of forming the q-table also results in noticeable changes. It should also be noted that different values for the gamma variable do not lead to significant changes.

As you can see in Fig. 4(d), the tumor cells reach zero at a longer period, which is the 19th day. The reason for the change in the behavior of the graph, in this case, is that only data with very low tumor amounts have been given to the model, so the model does not see any data with higher tumor amounts to make decisions about cases with more tumors. For more details on the implementation of the Q-learning algorithm, refer to [3,24]. In the next section, we will examine the results of implementing this method to control the dosage of chemotherapeutic drugs and delve into the discussion.

IV. RESULT AND DISCUSSION

In this part, we provide examples with numbers to show how effective the suggested RL method is for controlling cancer chemotherapy drug doses in a closed-loop system. Researchers conducted three experiments on three groups of young patients, elderly patients, and pregnant women to investigate the proposed controller, here only two of them have been studied [3,17].

A. *Young patient*

When treating a young patient with cancer, an oncologist prioritizes reducing the number of cancer cells quickly to prevent metastasis, even though this may result in damage to normal cells and immune cells. The body's ability to regenerate normal cells, which may be decreased as a side effect of chemotherapy, is more robust in young patients [3]. The body of a young patient can eliminate tumor cells due to the strength of the immune system. Therefore, if we consider the parameter s to be 0.33 in the depillis model, the output graph would appear as shown in Fig. 4(a).

B. *Elderly patient*

If we consider an elderly patient with weak immune cells, meaning we assume the value of s to be 0.2, in this condition the output graph will be transformed into Fig. 5.

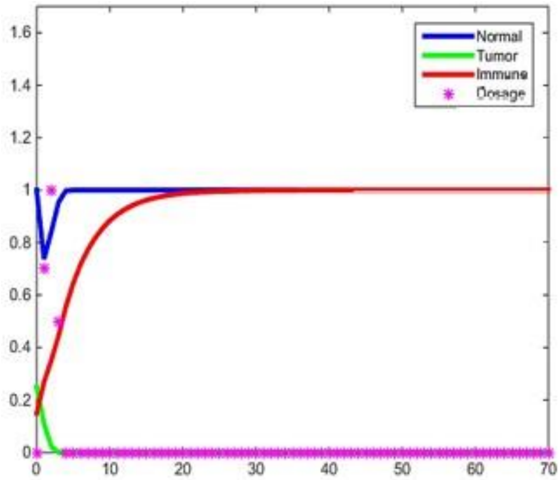

Fig. **5** Optimal control model for untreated elderly patient.

As can be seen, tumor cells have reached zero at the end of treatment, while the rate of immune cells has decreased to 1. In such conditions, to treat, immunotherapy should be used in addition to chemotherapy to improve these lost immune cells. The immunotherapy used is modeled by the equation below [17]:

$$\frac{ds}{dt}(t) = \mu_s v_v(t)(1 - \frac{s}{k_s}) \tag{7}$$

The therapeutic effect of immunotherapy with $v_v\ (t) \geq 0$ has been shown. The values of μ_s depend on the dynamics of the parameter s. This coefficient saturates to the final limit k_s, which is related to the biological constraints of body organs and the accumulation of external effects [17,25].

The output chart after chemotherapy treatment along with immunotherapy is shown using relationship 9 in Fig. 6.

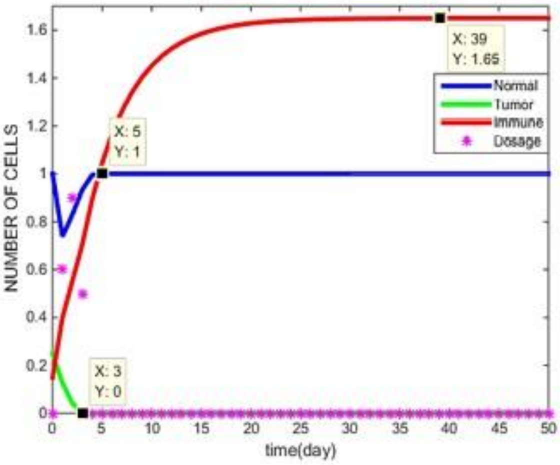

Fig. **6** Optimal control model for treated elderly patient.

Chemotherapy involves using drugs to kill cancer cells, while immunotherapy works by boosting the body's natural defenses to help the immune system recognize and attack cancer cells. When these two treatments are combined, they can have a synergistic effect and offer a more effective way to treat cancer. By combining chemotherapy with immunotherapy, doctors can potentially lower the dosage of chemotherapy drugs needed to achieve the desired effect, reducing the likelihood of side effects and toxicity. One way that doctors can control the optimal drug dosage when using a combination of chemotherapy and immunotherapy is through careful monitoring and adjustment of treatment plans.

The use of both chemotherapy and immunotherapy allows for a more personalized treatment plan for the elderly patient. Combining chemotherapy with immunotherapy can enhance the overall effectiveness of the treatment by targeting cancer cells through different mechanisms. This can potentially lead to better outcomes for the elderly patient. By carefully monitoring and controlling the dosage of each drug, doctors can potentially reduce the risk of side effects associated with chemotherapy and immunotherapy. This is especially important for elderly patients, who may be more susceptible to adverse reactions. Studies have shown that combining chemotherapy with immunotherapy can lead to improved survival rates for cancer patients, including elderly individuals. By controlling the optimal drug dosage, doctors can potentially increase the chances of successful treatment outcomes for elderly patients.

In this article, three scenarios were considered in order to investigate the effect of noise on the controller: the first scenario is adding noise only during the training phase, the second scenario is adding noise only during the simulation phase, and the third scenario is adding noise in both phases. Three values (0.25, 0.5, 1) were chosen for the percentage of noise. The noise is generated as a percentage of a randomly generated normal value that has been scaled to the desired variable value. The method of adding noise in the simulation stage was performed as follows:

After determining the initial state to start the simulation, a certain percentage of noise is added based on the range of the variable of interest, and the index of the Q-table is selected based on the noisy variable for updating. However, in the stage of obtaining the next state variables of the problem (calling the depillis model function), noise-free data is used. In this way, the added noise can be considered a measurement error in the simulation stage. (This means we have an error in measurement but in reality, the levels of different cells in the patient will change regardless of our measurement, so the noise-free value is given to the model).

Also, in the training phase, noise is added similar to the simulation phase, but with the difference that in the training phase, the current state is randomly selected in each iteration. The experiment conducted for different noise levels did not result in any significant difference in the performance of the model, and even when adding noise in both phases, a suitable and stable performance was observed.

In Figs. 7-9, charts related to adding noise to the model are shown

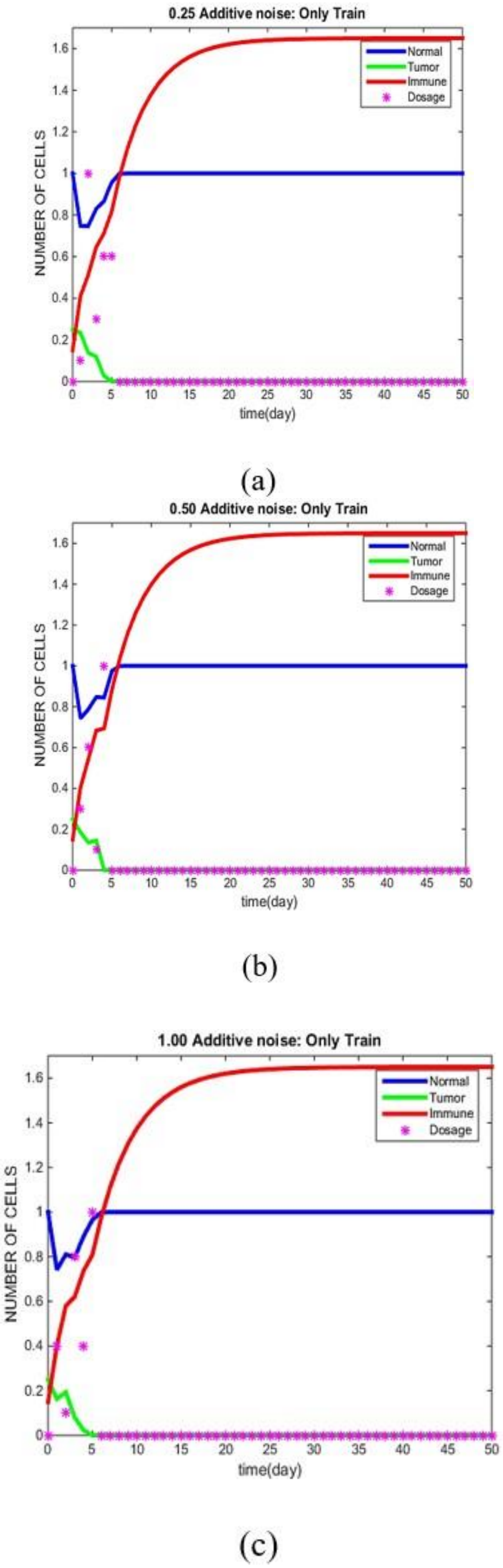

(a)

(b)

(c)

Fig. **7** Optimal control model in the presence of noise (only during the training phase).

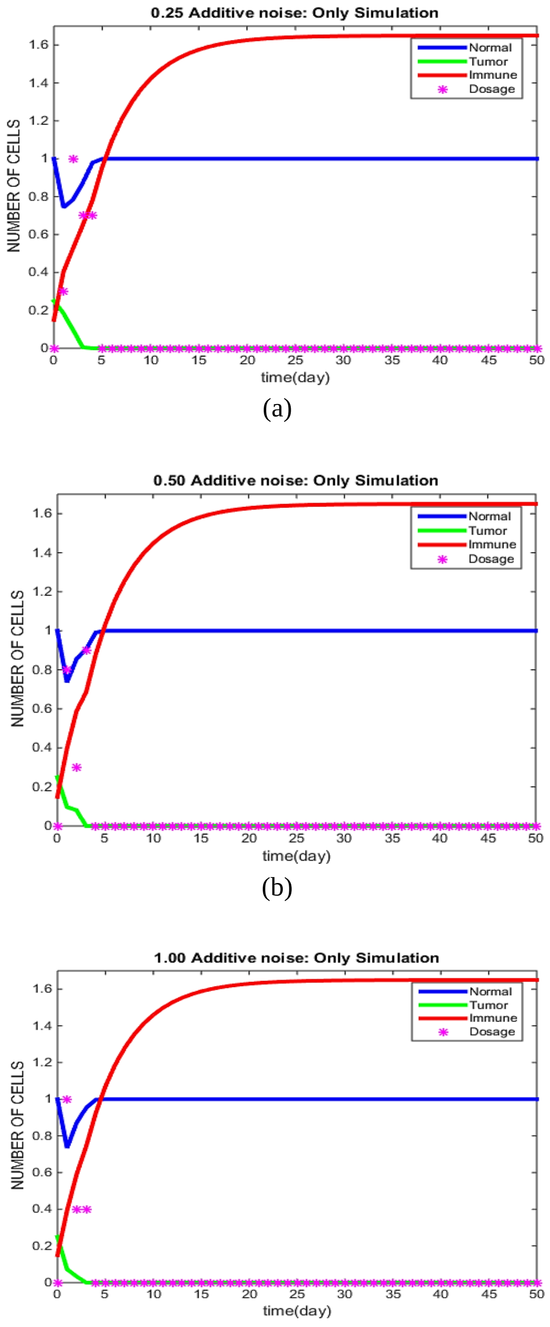

(a)

(b)

(c)

Fig. **8** Optimal control model in the presence of noise (only during the simulation phase).

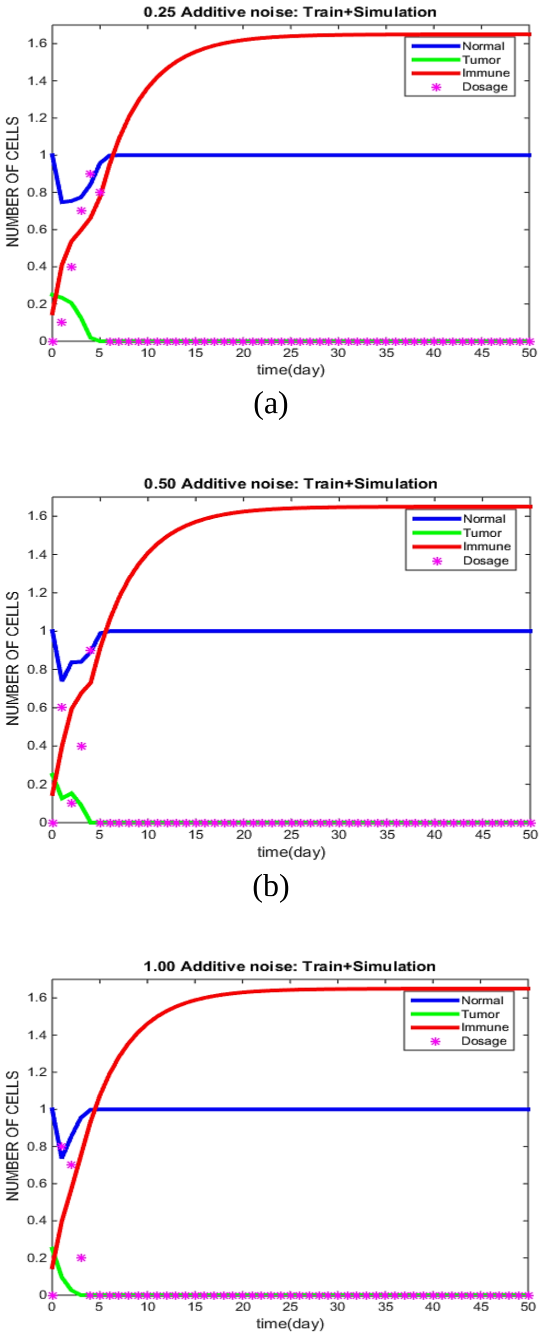

(a)

(b)

(c)

Fig. **9** Optimal control model in the presence of noise (In both stages of training and simulation).

Overall, the effect of adding noise to the Q-learning controller for determining cancer drug dosages will depend on the specific implementation and the balance struck between exploration and exploitation. Proper tuning and optimization of the noise parameters will be crucial in achieving the desired balance between exploration and exploitation while ensuring the safety and effectiveness of the treatment.

The benefit of the RL-based approach is its capability to develop a controller without the need for a system model.

Traditional chemotherapy dosage determination often relies on a trial-and-error approach, leading to suboptimal treatment outcomes and increased risk of side effects. Reinforcement learning-based controllers can expedite the dosage optimization process by continuously learning from patient responses and making data-driven decisions, reducing the need for trial-and-error approaches. Reinforcement learning algorithms can continuously learn and adapt to new information and patient responses, leading to ongoing improvements in treatment outcomes over time. This continuous learning process can help in refining the dosage regimen to achieve better long-term outcomes for cancer patients. When comparing our simulation findings to those reported in [3], we observe that both approaches yield very similar outcomes. In both instances, the tumor is eliminated through the use of optimal chemotherapy dosages, and the controllers prove to be resilient to changes in parameters. Simulation and differential equations described have been implemented using MATLAB software.

V. CONCLUSIONS AND FUTURE WORK

In this paper, the application and efficiency of a reinforcement learning-based controller in determining the optimal dosage of chemotherapy drugs were investigated. One of the primary goals of determining the dosage of chemotherapeutic drugs using Q-learning is to maximize the efficacy of the treatment. Another important goal is to minimize the toxicity of the treatment. Chemotherapeutic drugs can have significant side effects, so it is important to find the right dosage that will effectively treat the cancer while minimizing harm to the patient's healthy tissues. Q-learning can help doctors find the optimal balance between efficacy and toxicity. In the context of chemotherapy dosage optimization, the environment could be the patient's body, where the agent (in this case, the Q-learning algorithm) needs to determine the optimal dosage of the chemotherapeutic drug to administer based on factors such as the type of cancer, the patient's age and overall health, and the drug's pharmacokinetics. The reward in this case could be a combination of factors, such as the reduction in tumor size, the patient's overall health, and the absence of severe side effects. The Q-learning algorithm would learn from experience by iteratively adjusting the dosage of the chemotherapeutic drug based on the feedback it receives from the environment. Over time, the algorithm would converge on an optimal dosage that maximizes the reward while minimizing the side effects. In order to evaluate the RL-based method, noise was applied to the controller. One of the main advantages of RL-based controllers is their ability to learn and adapt to new environments and tasks without the need for extensive hand-coding or pre-programming. RL algorithms work by interacting with the environment and receiving feedback in the form of rewards, which allows them to learn optimal actions that maximize long-term rewards. This adaptability makes RL controllers well-suited for complex tasks or environments where traditional control methods may struggle to find a solution. Additionally, RL controllers can handle non-linear, high-dimensional, and uncertain systems, making them a versatile and powerful tool in the field of control systems.

RL-based controllers are trained on a specific dataset and may not generalize well to new or unseen data. This could lead to suboptimal dose determination in real-world scenarios. One of the future works could be to investigate the use of deep reinforcement learning algorithms for determining drug doses in clinical settings. This could involve developing more sophisticated Q-learning algorithms that can handle the complexities of individual patient responses and varying drug interactions. Examining the integration of reinforcement learning with other machine learning techniques, such as deep learning or natural language processing, to improve the accuracy and efficiency of drug dosage determination algorithms.

REFERENCES

[1] R.L. Siegel, K.D. Miller, and N.S. Wagle, "Cancer statistics," Ca Cancer J Clin, vol. 73, pp. 17-48, 2023.

[2] World Health Organization, *WHO report on cancer: setting priorities, investing wisely and providing care for all*, 2020.

[3] Padmanabhan, R., N. Meskin, and Wassim M. Haddad, "Reinforcement learning-based control of drug dosing for cancer chemotherapy treatment." Mathematical biosciences, vol. 293, pp. 11-20, 2017.

[4] C.Y. Yang, C. Shiranthika, C.Y. Wang, K.W. Chen, and S. Sumathipala, "Reinforcement learning strategies in cancer chemotherapy treatments: A review," Computer Methods and Programs in Biomedicine, vol. 229, pp.107280, 2023 .

[5] Perry MC, *The chemotherapy source book. Lippincott Williams & Wilkins*, 2008.

[6] P. Lecca, "Control theory and cancer chemotherapy: How they interact. Frontiers in Bioengineering and Biotechnology," vol. 14, pp.621269, 2021.

[7] R. Padmanabhan, N. Meskin, and AE. Al Moustafa, *Mathematical models of cancer and different therapies.* Singapore: Springer, 2021.

[8] Schättler H, and Ledzewicz U. *Optimal control for mathematical models of cancer therapies*, An application of geometric methods. 2015.

[9] Wu X, Liu Q, Zhang K, Cheng M, and Xin X. "Optimal switching control for drug therapy process in cancer chemotherapy," European Journal of Control. vol. 42, pp. 49-58, 2018.

[10] Padmanabhan R, Meskin N, and Haddad WM. "Optimal adaptive control of drug dosing using integral reinforcement learning," Mathematical biosciences. vol. 309, pp.131-142, 2019.

[11] Yazdjerdi P, Meskin N, Al-Naemi M, Al Moustafa AE, and Kovács L. "Reinforcement learning-based control of tumor growth under anti-angiogenic therapy," Computer methods and programs in biomedicine. vol. 173, pp. 15-26, 2019.

[12] Shiranthika C, Chen KW, Wang CY, Yang CY, Sudantha BH, and Li WF. "Supervised optimal chemotherapy regimen based on offline reinforcement learning," IEEE Journal of Biomedical and Health Informatics. vol.26, pp. 4763-4772, 2022.

[13] R. Padmanabhan, N. Meskin, and W.M. Haddad, "Reinforcement learning-based control of drug dosing with applications to anesthesia and cancer therapy," Control applications for biomedical engineering systems, Academic Press. vol.1, pp. 251-297, 2020.

[14] A.T. Azar, *Control Applications for Biomedical Engineering Systems*, Academic Press; 2020.

[15] Kalhor E, Noori A, and Saboori Rad S, "Sadrnia MA. Using Eligibility Traces Algorithm to Specify the Optimal Dosage for the Purpose of Cancer Cell Population Control in Melanoma Patients with a Consideration of the Side Effects," Journal of Soft Computing and Information Technology. vol.10, pp. 72-92, 2021.

[16] A. Noori, E. Kalhor, and S. Saboori Rad, "Controlling the Cancer Cells in a Nonlinear Model of Melanoma by Considering the Uncertainty Using Q-learning Algorithm Under the Case Based Reasoning Policy," Journal of Iranian Association of Electrical and Electronics Engineers, vol. 17, pp. 25-37, 2020.

[17] Mashayekhi H, and Nazari M. "Reinforcement learning based feedback control of tumor growth by limiting maximum chemo-drug dose using fuzzy logic," Journal of Control. vol. 15, pp. 13-23, 2022.

[18] H. Tourajizadeh, Z.G. Zarandi, Z. Farbodi, and E.S. Ghasemabadi, "Modelling and Control of Mutation Dynamics of the Cancer Cells Employing Chemotherapy," International Journal of Advanced Design & Manufacturing Technology. vol. 15, pp. 73-83, 2022.

[19] Z.G. Zarandi, H. Tourajizadeh, Z. Farbodei, E.S. Ghasemabad, "Dynamic Modeling of the Cancer Cell Mutation with the Capability of Control Using Chemotropic Injection," International Conference on Robotics and Mechatronics (ICRoM),vol. 26, pp. 1-8, 2020.

[20] Agarwal A, Jiang N, Kakade SM, and Sun W. "Reinforcement learning: Theory and algorithms," CS Dept. UW Seattle, Seattle, WA, USA, Tech. Rep. vol. 32, pp. 1-83, 2019.

[21] Winder P. *Reinforcement learning*, O'Reilly Media, 2020.

[22] De Pillis LG, and Radunskaya A. "The dynamics of an optimally controlled tumor model: A case study," Mathematical and computer modeling. Vol. 37, pp. 1221-1244, 2003.

[23] Clifton J, and Laber E. “Q-learning: Theory and applications,” Annual Review of Statistics and Its Application. vol. 7, pp. 279-301, 2020.

[24] Padmanabhan R, and Meskin N, “Haddad WM. Closed-loop control of anesthesia and mean arterial pressure using reinforcement learning. Biomedical Signal Processing and Control. Vol. 22, pp. 54-64, 2015.

[25] Nazari M, and Ghaffari A. “The effect of finite duration inputs on the dynamics of a system: Proposing a new approach for cancer treatment,” International Journal of Biomathematics. vol. 8, pp. 1550036, 2015.

THIS PAGE IS INTENTIONALLY LEFT BLANK.

IJBBE International Journal of Biophotonics & Biomedical Engineering Vol. 4, No. 1, Spring-Summer, 2024

Research Article

Treatment planning based dosimetric impact of Radiotherapy on Anxiety-Related Cognitive Impairment in Head, Neck and Brain Tumour Patients

M. Mohammadhashemia and Sh. Shahi*b

a Department of Biomedical Engineering, Isfahan (Khorasgan) branch, Islamic Azad University, Isfahan, Iran
b Department of Biomedical Engineering, Laser and Biophotonics in Biotechnologies Research Center, Isfahan (Khorasgan) branch, Islamic Azad University, Isfahan, Iran

***Corresponding author: shahilaser@khuisf.ac.ir**

DOI: 10.71498/ijbbe.2024.1128192

ABSTRACT

Received: Aug. 4, 2024, Revised: Dec. 17, 2024, Accepted: Dec. 29, 2024, Available Online: Jan. 26, 2025

Radiotherapy is a common method for treating cancer, but it can have unintended side effects such as cognitive impairment (anxiety). This study aims to investigate the dosimetry impact on cognitive impairment including anxiety caused by radiotherapy for head, neck, and brain tumors based on treatment planning systems. This analytical cross-sectional study was conducted in 2024 at the Isfahan Radiotherapy Center (Seyed al-Shohada Hospital). It involved 30 patients with head, neck, and brain tumors who underwent radiotherapy using treatment planning systems (Prowess Panther). The treatment planning system (TPS), Prowess Panther, accurately calculated the radiation doses to brain structures associated with cognitive functions like memory, which helped assess the link between radiation exposure and anxiety. The doses received by brain structures related to memory (amygdala) were calculated using the treatment planning systems (Prowess Panther) and compared with the incidence of cognitive impairment (anxiety). Data analysis was performed using SPSS-24 software and analyzed. Results indicated a significant correlation between the doses received by memory-related brain structures and the incidence of anxiety. Specifically, 23.3% of patients experienced mild or higher anxiety levels (score of 14 or more), with an average anxiety score of 8.63 (±3.56). The patient treatment outcomes showed that most of them well responded to radiotherapy. However, those receiving higher doses of memory-related brain structures experienced increased anxiety, which may affect long-term recovery. These patients had higher average, maximum, and minimum doses compared to those who did not experience anxiety after treatment. These findings suggest that precise dosimetry of memory-related brain structures in radiotherapy planning may help mitigate the risk of developing memory-related neurocognitive disorders, thereby improving patient outcomes.

KEYWORDS

Radiation therapy, Neurological memory disorder (anxiety), Treatment planning system.

I. INTRODUCTION

Cancer, a leading cause of death globally, accounted for approximately 10 million deaths in 2020 alone [1]., characterized by the rapid and uncontrolled growth of abnormal cells that can metastasize to other organs. [2,3]. This uncontrolled proliferation can result from minor disruptions in the regulatory signals governing normal cell growth, leading to significant health impacts, particularly in developing countries where cancer-related mortality is steadily increasing [4,5].

Radiotherapy is one of the primary treatment methods for cancer, and it is estimated that more than half of cancer patients will undergo radiotherapy during their treatment. In this method, high-energy rays such as X-rays, gamma rays, or electrons with controlled energy are used to destroy or shrink cancer cells. Radiotherapy can be used alone to treat certain types of cancer. It can also be used in conjunction with other treatment methods such as surgery or chemotherapy [6].

A brain tumor refers to an abnormal growth of cells within the brain or spinal canal. The growth of these tumors can lead to increased pressure inside the skull and spinal canal. The origin of the tumor can be from brain tissue itself or it can spread to the brain from elsewhere (metastasis). Generally, a brain tumor is an abnormal mass (neoplasm) inside the skull or spinal canal. Brain tumors are categorized into two types: benign (non-cancerous) and malignant (cancerous) [7,8].

Today, the choice of radiotherapy technique for brain tumors is usually between three-dimensional conformal radiotherapy (3-D CRT), intensity-modulated radiation therapy (IMRT) with fixed beam angles, or volumetric modulated arc therapy (VMAT). The selection of the appropriate method depends on various factors, such as the type and location of the tumor, the overall health of the patient, and the availability of equipment and treatment facilities [9].

Radiotherapy, a common cancer treatment, can have a range of side effects that vary depending on the treated area, radiation dose, and the patient's overall health [10]. When treating head and neck cancers, the brain often receives incidental doses of radiation, potentially causing neurocognitive changes and affecting the patient's quality of life [22,23].

Radiotherapy, a common method for cancer treatment, can damage not only cancerous cells but also healthy brain and nervous system cells. This damage can lead to various neurological disorders, including memory problems. One of the most common cognitive disorders associated with radiotherapy is memory impairment. It is estimated that 20 to 50 percent of patients undergoing radiotherapy for head and neck cancers or brain tumors experience varying degrees of memory impairment. Symptoms of memory impairment in radiotherapy patients may include [11]:

- **Difficulty Learning and Retaining New Information:** Patients may have trouble learning new things such as names, dates, or directions.

- **Difficulty Remembering Old Information:** Patients may struggle to recall information they previously knew, such as past events or personal details.

- **Difficulty with Concentration and Attention:** Patients may find it challenging to focus on a task or conversation for extended periods.

- **Difficulty Finding Words:** Patients may have trouble finding the right words to express their thoughts [12].

There is no definitive treatment for memory impairment in patients undergoing radiotherapy, but various methods can help manage this issue, including [13]:

- **Cognitive Strategies:** Patients can use various strategies such as making lists, using calendars, and setting reminders to assist with their memory.

There is no definitive treatment for memory impairment in patients undergoing radiotherapy, but various methods can help manage this issue, including [13]:

- **Cognitive Strategies:** Patients can use various strategies such as making lists, using calendars, and setting reminders to assist with their memory.

- **Cognitive Exercises:** Some studies have shown that cognitive exercises can help improve memory in patients undergoing radiotherapy.

- **Medications:** Certain medications, such as cholinesterase inhibitors, may help alleviate symptoms of memory impairment in some patients.

Anxiety is a natural and common reaction to stress or danger. It is an uncomfortable and nervous feeling or state associated with various physical and psychological symptoms [14].

Symptoms of anxiety include [15]:

- **Physical Symptoms:** Palpitations, sweating, trembling, rapid breathing, muscle pain, dry mouth, nausea, headache, dizziness, fatigue.

- **Psychological Symptoms:** Feelings of nervousness or agitation, difficulty concentrating, irritability, restlessness, trouble sleeping, feelings of fear or panic, negative thoughts.

This study aims to investigate the dosimetric impact of radiotherapy on cognitive impairment, specifically focusing on anxiety levels in patients with head, neck, and brain tumors. The study aims to derive the dosimetric data from the patient's plan created within the TPS. By assessing doses received by memory-related brain structures, especially the amygdala, the correlation between radiation exposure and the incidence of anxiety in this patient population was examined.

II. MATERIAL AND METHODS

In this study, data related to radiotherapy doses and clinical characteristics of patients undergoing radiotherapy for brain, head-and-neck tumors were collected over a two-month follow-up period. This information included the contouring of organs associated with neurological anxiety-related complications. The Prowess Panther is employed as a treatment planning system (TPS). In this study, 30 patients who followed inclusion and exclusion criteria and provided written consent were examined.

Using Equation 1 and the data from prior studies, an initial sample size of 25 was calculated to study neurological side effects from radiotherapy. Accounting for a 30% non-cooperation rate, the final sample size was adjusted to 30, with participants selected from the Isfahan radiotherapy center (Seyed al-shahada Hospital)

$$n = \frac{Z_{1-\alpha}^2 . p(1-p)}{d^2} \quad (1)$$

$$Z_{1-\alpha}^2 = (1.96)^2$$
$$p = 0.04$$
$$\alpha = 0.05$$
$$d = 0.10$$

Selection Criteria:

1. Adults (aged 18 and above) with a diagnosis of brain or head-and-neck tumors undergoing radiotherapy.

2. Patients who provided written informed consent to participate in the study.

3. Patients able to complete follow-up evaluations during the 2-month study period.

Exclusion Criteria:

1. Patients with pre-existing neurological disorders (such as epilepsy, dementia, or significant cognitive impairments) that could confound the study results.

2. Patients with metastatic brain tumors or tumors outside the scope of the study (i.e., non-head-and-neck regions).

3. Patients who experienced significant complications during treatment, such as severe infections or other conditions that required immediate medical intervention.

4. Patients unable or unwilling to complete the Beck Anxiety Inventory or follow-up assessments.

The aim of this study was to assess grade 1 toxicity related to cognitive neurological disorders (according to CTCAEv4.03), meaning that the patient should be able to maintain independence in performing daily activities. Patient follow-up was conducted in two stages: 1) before the start of radiotherapy and 2) 2 months after the completion of radiotherapy. At each stage, patients were asked to complete a questionnaire to collect clinical information.

In this study, information was collected in three stages:

A. *Treatment Planning and Contouring:*

During the treatment planning stage for patients with brain tumors, a three-dimensional conformal radiation therapy (3D-CRT) technique was utilized. Each patient's treatment plan included the careful contouring of organs at risk, with a specific focus on the amygdala due to its association with cognitive functions.

To reduce the risk of cognitive impairment associated with radiation exposure, the maximum dose to the amygdala was restricted to 20 Gy. Additionally, the mean dose was maintained below 12 Gy. This is recommended to minimize neurological side effects while effectively targeting the tumor [25,26].

B. *Data Extraction:*

Patient records were reviewed, and the necessary clinical and dosimetry information, including the prescribed dose for the mentioned organs, was extracted.

C. *Patient Follow-up:*

Patients were followed up for two months after the completion of radiotherapy to assess the occurrence of anxiety-related neurological side effects.

All patients were followed up for 2 months to assess potential neurological side effects of radiotherapy, including anxiety.

Anxiety is a natural bodily response to challenges and dangerous situations. This response is associated with symptoms such as palpitations, muscle tension, and mental worries. While anxiety can be beneficial at normal levels, it can sometimes escalate into uncontrollable and excessive fear and worries, causing disruptions in an individual's daily life.

The Beck Anxiety Inventory (BAI) is a tool designed to measure the level of anxiety in individuals. This questionnaire consists of 21 questions that are designed to be easily answered by people of all ages, including both adolescents and adults. As previously mentioned, individuals answer these questions based on their perceptions of their characteristics and traits. The questions cover a broad range of topics, including the following:

- Feeling hot
- Trembling legs
- Palpitations
- Fear of impending disaster
- Numbness and tingling
- Nervousness
- Panic
- Shaking hands
- Dizziness and confusion
- Feeling unsteady
- Fear of losing control
- Difficulty breathing
- Feeling weak
- Muscle tension
- Fear of death and oblivion
- Fainting and weakness
- Startling easily
- Indigestion
- Blushing and flushing
- Sweating

Each question is answered based on the severity of the symptoms experienced, and responses are scored from 0 to 3, with the total score ranging from 0 to 63. This inventory helps in evaluating the intensity of anxiety symptoms and can aid in understanding the impact of anxiety on daily functioning [16].

0 to 13: Mild or no symptoms of anxiety and depression

14 to 19: Mild anxiety and depression

20 to 28: Moderate anxiety and depression

29 to 63: Severe anxiety and depression

In this study, mild or higher anxiety and depression (a score of 14 or more) were considered as the endpoint. The questionnaires used in this study are included.

Besides, data were described using statistical measures such as mean, standard deviation, frequency, and percentage frequency. To compare two groups for significant differences, the Chi-square (χ^2) test with an alpha level of 0.05 was used. All statistical analyses were conducted using SPSS version 24, with a significance level of 5%.

For the analysis of the Beck questionnaire, descriptive statistics including mean, standard deviation, frequency, and percentage frequency were employed. To assess the normality of the distribution of errors in quantitative variables, the Kolmogorov-Smirnov test was used. For inferential statistics, the Mann-Whitney U test and the Kruskal-Wallis test were applied. All analyses were performed in SPSS version 24, with a significance level of 5%.

III. RESULT

In this study, the 30 patients with cancers of the head, neck, and brain tumors, who were treated at the Isfahan Radiotherapy Center (Seyed al-shahada Hospital) between 2023 and 2024, were examined. The average age of the patients was 44.6 years, with 70.0% of them being female. 66.7% of the patients received chemotherapy concurrently with radiotherapy, and 23.3% had a history of surgery. The oldest participant in this study was a 71-year-old woman, and the youngest was a 20-year-old woman. Eleven patients (36.7%) had a family history of cancer. The patients' body mass index (BMI) ranged from 18.5 to 24.9. (Table 1)

TABLE 1: THE CLINICAL CHARACTERISTICS OF PATIENTS

Frequency (Percentage)	Levels of Variable	Variable
7(23.3)	20-35	age
13(43.3)	36-50	
9(30.0)	51-70	
1(3.3)	>71	
21(70)	women	sex
9(30)	Men	
7(23.3)	Yes	Surgical History
23(76.7)	No	
11(36.7)	Yes	Underlying Disease
19(63.3)	No	
11(36.7)	Yes	Family History of Cancer
19(63.3)	No	
0(0.0)	>18.5	Body Mass Index (BMI)
15(50.0)	<18.5	
14(46.6)	24.9	
1(3.3)	>25	
0(0%)	>29.9	
0(0%)	<30	
0(0%)	39.9	
20(66.7)	Yes	Chemotherapy
10(33.3)	No	

Two months after the end of treatment, patients were examined for potential side effects. The findings of this examination are presented in Table 2 and illustrated in Fig. 1. As shown in Table 2 and Fig. 1, the average levels of anxiety were categorized as follows:

TABLE 2: MEAN ANXIETY SCORES BASED ON QUESTIONNAIRE DIMENSIONS

Dimension	Mean (Standard Deviation)	Frequently(percent)
Mild or No Depression (0 to 13)	2.13(0.75)	(76.6) 23
Mild Anxiety and Depression (14 to 19)	0	0 (0)
Moderate Anxiety and Depression (20 to 28)	22.75 (1.15)	4 (13.4)
Severe Anxiety and Depression (29 to 63)	39.66 (2.22)	3 (10.0)
Total Anxiety	8.63 (3.56)	7 (23.3)

As indicated, the overall anxiety levels among the patients revealed that 23.3% experienced anxiety (score of 14 or more), while the average anxiety score was 8.63 (±3.56).

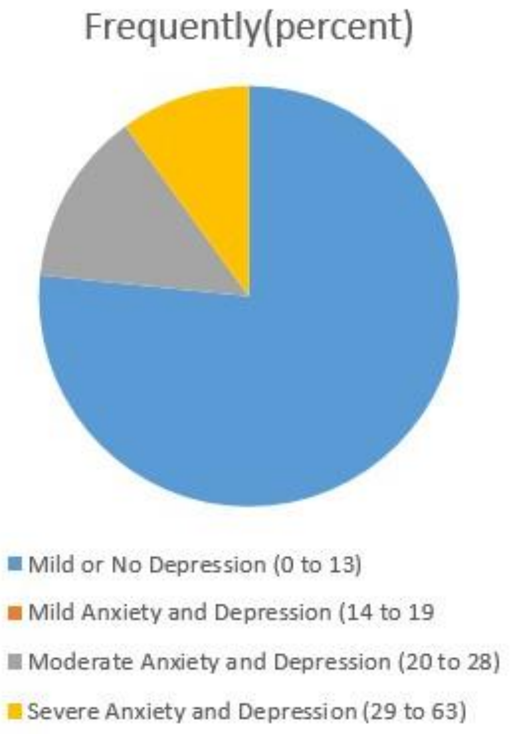

Fig. **1**: Mean Anxiety Scores Based on Questionnaire Dimensions

The frequency of responses from cancer patients undergoing radiotherapy to various items on the Beck Anxiety Inventory is presented in Table 3 and illustrated in Fig. 2. The items with the highest percentage of "Not at All" responses included "Dizziness and Lightheadedness," "Variable (Unstable) Mood," "Feeling of Suffocation," "Hand Tremors," and "Difficulty Breathing," each receiving 80.0% of responses.

TABLE 3: FREQUENCY OF RESPONSES TO VARIOUS ITEMS ON THE BECK ANXIETY INVENTORY

Item	Not at All (%)	Slightly (Didn’t bother me much) (%)	Moderately (Very unpleasant but I tolerated it) (%)	Severely (I couldn't tolerate it) (%)
1. Numbness and tingling	60.0	23.3	13.3	3.3
2. Feeling of warmth	56.7	26.7	13.3	3.3
3. Trembling in legs	63.3	23.3	13.3	0.0
4. Inability to relax	70.0	16.7	13.3	0.0
5. Fear of a bad event	70.0	20.0	13.3	0.0
6. Dizziness and lightheadedness	80.0	13.3	10.0	0.0
7. Palpitations and breathlessness	76.7	10.0	10.0	3.3
8. Variable (unstable) mood	80.0	10.0	10.0	0.0
9. Panic	76.7	10.0	13.3	0.0
10. Nervousness	76.7	13.3	10.0	0.0
11. Feeling of suffocation	80.0	13.3	6.7	0.0
12. Hand tremors	80.0	10.0	10.0	0.0
13. Body tremors	76.7	16.7	6.7	0.0
14. Fear of losing control	76.7	16.7	6.7	0.0
15. Difficulty breathing	80.0	10.0	10.0	0.0
16. Fear of dying	76.7	16.7	6.7	0.0
17. Fearful (state of fear)	70.0	20.0	6.7	3.3
18. Indigestion and stomach discomfort	70.0	23.3	6.7	0.0
19. Fainting	63.3	23.3	6.7	6.7
20. Blushing	53.3	33.3	10.0	3.3
21. Sweating (not due to heat)	56.7	26.7	13.3	3.3

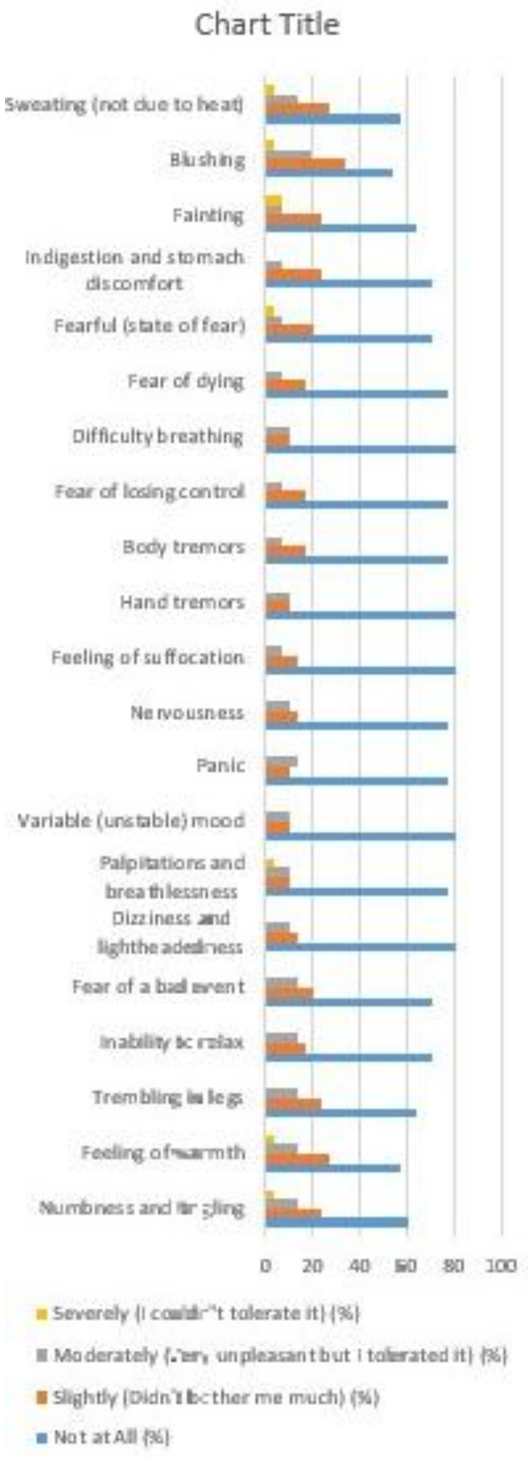

Fig. **2**: Frequency of Responses to Various Items on the Beck Anxiety Inventory.

A comparison of dosimetric data revealed that patients with anxiety complications received higher average, maximum, and minimum doses to the amygdala compared to those without complications. The average dose to the amygdala in patients with anxiety was 16.5 Gy (±3.2 Gy), while patients without anxiety had an average dose of 10.2 Gy (±2.8 Gy). The maximum dose recorded for the amygdala in the anxiety group was 24.0 Gy, while in the non-anxiety group, it was 15.0 Gy. These results indicate a significant correlation between radiation doses received by the amygdala and the incidence of anxiety in patients undergoing radiotherapy.

IV. DISCUSSION

Radiotherapy, as one of the three effective treatment methods for cancer, plays a key role in treating more than half of the patients. The main goal of radiotherapy is to inflict maximum damage to the tumor while causing the least damage to the surrounding healthy tissues. Therefore, in treatment planning, the priority is to apply the maximum dose to the tumor while considering dose limitations for the surrounding organs at risk (OAR). However, during radiotherapy, it is inevitable that doses also reach non-target tissues and organs also receive some level of radiation exposure, which can lead to side effects, both acute and long-term.

In patients undergoing treatment, while a considerable amount of research exists on the dosimetric aspects of radiotherapy and its immediate effects, there is limited literature exploring the psychological consequences, such as anxiety and depression. Furthermore, the role of these side effects on patients' quality of life is an area of growing concern. The present study contributes to this body of research by investigating the relationship between radiotherapy doses and the onset of anxiety in patients with head, neck, and brain tumors.

Studies conducted on dosimetry, anxiety, and depression in patients undergoing radiotherapy are very limited and mostly focus on the impact of these side effects on patients' quality of life. McDowell and colleagues conducted a study in 2018, the results of which were similar to the findings of the present study regarding the incidence of these side effects. In this study, most patients were treated with a dose of 2 Gy per fraction. Consequently, 25 percent of the patients exhibited symptoms of depression and 37 percent showed symptoms of anxiety, which had a significant impact on their quality of life [19]. These results are similar to the findings in our study, where 23.3% of patients experienced mild or higher levels of anxiety.

Jaspers and colleagues conducted a study in 2019 to investigate the impact of radiotherapy on the memory of patients with low-grade glioma. In this study, 29 patients were treated with DR-AVLT, and their memory was assessed before treatment and 18 months after treatment using the Auditory-Verbal Learning Test (AVLT). The results showed that 14 out of 29 patients (48%) experienced learning impairments after radiotherapy [20]. While cognitive impairments were not directly assessed in our study, the link between radiotherapy and cognitive dysfunction may also contribute to the psychological symptoms of anxiety.

Mr. Ma and colleagues, in a 2017 study titled "Prospective Evaluation of the Effects of Hippocampal Radiation Dose-Volume and Memory Deficits After Cranial Radiotherapy," examined the relationship between hippocampal radiation dose and memory loss in patients undergoing cranial radiotherapy. In this study, the HVLT/R test was used to assess patients' memory. The results indicated a direct relationship between the hippocampal radiation dose and memory decline across a wide range of doses. Specifically, receiving a 22 Gy dose to 50% of the hippocampus led to a 20% reduction in patients' memory [21]. Our findings also suggest a dose-dependent relationship between radiotherapy and psychological distress, specifically anxiety.

In the present study, as shown in the table from the previous section, the side effect of anxiety was examined 60 days after treatment. According to the results from the previous chapter, mild or higher levels of anxiety and depression (a score of 14 or more) were considered the final side effects. Overall, 7 patients experienced anxiety as a side effect. Additionally, the minimum, average, and maximum doses in patients with this side effect were significantly higher than in patients without the side effect.

V. CONCLUSION

In this study, the possibility of dosimetric comparison between patients with and without neuropsychological anxiety disorders undergoing treatment for head, neck, and brain tumors was investigated. The results showed that dosimetric factors were higher in patients with anxiety disorders compared to those without. However, to determine the impact of the dose per session on damage to the amygdala and other sensitive organs, more experimental studies and long-term patient follow-ups are needed to assess the effects and their relationship with dosimetric factors.

Additionally, the average anxiety scores in cancer patients undergoing radiotherapy showed significant differences across variables such as gender, family history of cancer, and chemotherapy.

OTHER RECOMMENDATIONS

This study commenced after receiving ethical approval from the research committee of Khorasgan Islamic Azad University. This study was conducted with the permission and support of Isfahan Islamic Azad University, Iran.

REFERENCES

[1] FERLAY, Jacques, et al. "Cancer statistics for the year 2020: An overview," International journal of cancer, vol. 149, pp. 778-789, 2021.

[2] GOMES and Barbara, "HIGGINSON, Irene J. Factors influencing death at home in terminally ill patients with cancer: systematic review," Bmj, vol. 332, pp. 515-521, 2006.

[3] VAN DEN BEUKEN-VAN, Marieke Hj, et al. "Update on prevalence of pain in patients with cancer: systematic review and meta-analysis," Journal of pain and symptom management, vol. 51, pp. 1070-1090. 2016.

[4] HENRIKSON N. B. et al. "Family history and the natural history of colorectal cancer:

systematic review," Genetics in medicine, vol. 17, pp. 702-712, 2015.

[5] PETTICREW M. BELL R. HUNTER D. "Influence of psychological coping on survival and recurrence in people with cancer: systematic review," Bmj, vol. 325, pp. 7372: 1066, 2002.

[6] ZHANG Z. et al. "Radiotherapy combined with immunotherapy: the dawn of cancer treatment," Signal transduction and targeted therapy, vol. 7, pp. 258, 2022.

[7] H. Damasio, Human brain anatomy in computerized images, Oxford university press, 2005.

[8] L.M. DeAngelis, "Brain tumors," New England journal of medicine, vol. 344, pp. 114-123, 2001.

[9] AFRIN, Kazi T. AHMAD, Salahuddin. "3D conformal, IMRT and VMAT for the treatment of head and neck cancer: a brief literature review," Journal of Radiotherapy in Practice, vol. 21, pp. 259-262, 2022.

[10] CHEN D. et al. "The efficacy of positioning stents in preventing Oral complications after head and neck radiotherapy: a systematic literature review," Radiation Oncology, vol. 15, pp. 1-7, 2020.

[11] CROSS N. E. and GLANTZ M. J. "Neurologic complications of radiation therapy," Neurologic clinics, vol. 21, pp. 249-277, 2003.

[12] GIGLIO P. GILBERT M. R. "Neurologic complications of cancer and its treatment," Current oncology reports, vol. 12, pp. 50-59, 2010.

[13] GIGLIO P. GILBERT M. R. "Neurologic complications of cancer and its treatment," Current oncology reports, vol. 12, pp. 50-59, 2010.

[14] GOGOU P. et al. "The impact of radiotherapy on symptoms, anxiety and QoL in patients with cancer," Anticancer research, vol. 35, pp. 1771-1775, 2015.

[15] CHEN Lee-Chen, et al. "Fifteen-minute music intervention reduces pre-radiotherapy anxiety in oncology patients," European Journal of Oncology Nursing, vol. 17, pp. 436-441, 2013.

[16] A.S. Kaufman, E.O. Lichtenberger, Assessing adolescent and adult intelligence, John Wiley & Sons; 2005 .

[17] BEHMADI M. et al. "Evaluation of breast cancer radiation therapy techniques in outfield organs of the rando phantom with thermoluminescence dosimeter," Journal of Biomedical Physics & Engineering, vol. 9, pp. 179, 2019.

[18] KHAN F. M. (ed.). The physics of radiation therapy. Lippincott Williams & Wilkins, 2010.

[19] MCDOWELL Lachlan J. et al. "Long-term late toxicity, quality of life, and emotional distress in patients with nasopharyngeal carcinoma treated with intensity modulated radiation therapy," International Journal of Radiation Oncology* Biology* Physics, vol. 102, pp. 340-352, 2018.

[20] JASPERS, Jaap, et al. "Evaluation of the hippocampal normal tissue complication model in a prospective cohort of low grade glioma patients—An analysis within the EORTC 22033 clinical trial," Frontiers in Oncology, vol. 9, pp. 991, 2019.

[21] M.A. Ting Martin, et al. "A prospective evaluation of hippocampal radiation dose volume effects and memory deficits following cranial irradiation," Radiotherapy and Oncology, vol. 125, pp. 234-240, 2017.

[22] Zsuzanna lyizoba-Ebozue, et al. "Neurocognitive function following (chemo) radiotherapy for nasopharyngeal cancer and other head and neck cancers: Asystematic review," Radiother Oncol, vol. 188, pp. 109863, 2023.

[23] K. Demos-Davies, J. Lawrence, and D. Seelig, "Cancer related cognitive impairment: a downside of cancer treatment," vol. 14, pp. 1-22, 2024.

[24] Y. Huang, H. Zhou, F. An, A. Zhao, J. Wu, M. Wang, and J. Luo, "The relevance of ototoxicity induced by radiotherapy," Radiation Oncology, vol. 18, pp. 1-17, 2023.

[25] T.M. Ma, J. Grimm, and R. McIntyre, et al. Prospective Evaluation of Hippocampal Dose-Volume and Memory Deficits After Cranial Radiotherapy, 2017.

[26] L.J. McDowell, J. Ringash, W. Xu, B. Chan, et al. Neurocognitive Function and Quality of Life After Cranial Radiation Therapy: Predictive Models and Dosimetric Thresholds, Elsevier, 2018.

THIS PAGE IS INTENTIONALLY LEFT BLANK.

IJBBE International Journal of Biophotonics & Biomedical Engineering Vol. 4, No. 1, Spring-Summer, 2024

Research Article

Comparative analysis of PET image characteristics using two types of crystals BGO and LYSO with GEANT4 simulation

M. Golshanipour [a] and Sh. Shahi *[b]

a Department of Biomedical Engineering, Isfahan (Khorasgan) branch Islamic Azad University, Isfahan, Iran.
b Department of Biomedical Engineering, Laser and Biophotonics in Biotechnologies Research Center, Isfahan (Khorasgan) branch, Islamic Azad University, Isfahan, Iran

***Corresponding author:** shahilaser@khuisf.ac.ir

DOI: 10.71498/ijbbe.2024.1128184

ABSTRACT

Received: Aug. 4, 2024, Revised: Jan. 3, 2025, Accepted: Jan. 4, 2025, Available Online: Jan. 27, 2025

Positron emission tomography is a nuclear imaging technique that uses radiotracers to observe the body's metabolic activities in real time. Key to PET systems are the scintillation crystals in detectors, which impact image quality. This study examines BGO and LYSO crystals, analyzing optical yield, decay time, energy resolution, and contrast using GEANT4 simulations. In this simulation, G4EmStandardPhysics was employed as the primary physics model Results show distinct performance patterns between the crystals that the BGO recorded an average of 499 energy deposition events, slightly higher than LYSO's 485.9. The BGO also achieved a higher patient dose score of 3.06126 versus 3.04326 for LYSO. Both crystals show similar behavior in energy depositions per crystal block, with BGO at 13.14 and LYSO at 13.02, but LYSO had a more concentrated energy distribution and better resolution. The findings indicate the BGO's strengths in interaction rates, cost, and durability, while the LYSO offers enhanced resolution due to more focused energy distribution. This study highlights the trade-offs between the BGO's affordability and higher interaction rate in comparison with the LYSO's superior image resolution based on specific imaging and priorities. This study, as an innovative approach and in contrast to previous studies, directly and simultaneously compared the characteristics of these two types of crystals. Enhancing the accuracy of disease diagnosis and improving the performance of PET systems are among the outcomes of this study.

KEYWORDS

PET imaging, GEANT4 simulation, BGO and LYSO crystals, Energy deposition, Dosimetry.

I. INTRODUCTION

PET is a nuclear medical imaging method used to study the metabolic and molecular functions of the human body. In this technique, positron-emitting radioisotopes, such as Fluorine-18, are used to label biologically active molecules. PET detectors identify these photons and record their positions. This information is then used to reconstruct three-dimensional images of the radioisotope distribution in the body [1,2]. Artificial intelligence and deep learning in enhancing positron emission tomography image reconstruction stating that these technologies significantly improve image quality and diagnostic performance compared to traditional methods [25,26,27].

Total-body imaging modalities provide advantages such as higher sensitivity and low-dose imaging, but high construction costs limit their global use [28].

This paper compares two widely used scintillation crystals, BGO and LYSO, which are essential components in PET imaging systems. Their distinct physical properties, including energy resolution, light yield, and decay time, affect their performance and are evaluated using GEANT4 simulations.

The choice of PET detector crystal type is a key factor in determining image quality. BGO and LYSO are two common crystals that are used in PET imaging, each with its advantages and disadvantages. BGO is less expensive and more durable, but it has lower image resolution compared to LYSO. LYSO offers higher image resolution but is more expensive and more prone to breakage [3,4].

GEANT4 simulation is a powerful tool for simulating PET systems. This tool can simulate the paths of particles and their interactions with matter. GEANT4 simulations can be used to compare the performance of BGO and LYSO in PET systems under different geometries and conditions [5].

PET detectors are key components of PET systems that are used to detect gamma photons emitted from radiopharmaceuticals. These photons are then used to generate three-dimensional images of the distribution of radiopharmaceuticals in the patient's body [6].

BGO is an inorganic crystal with the chemical formula Bi3Ge4O12. Due to its unique physical properties, BGO finds applications in a wide spectrum of uses including nuclear medical imaging, particle detection, and nonlinear optics [7].

With a density of 7.13 g/cm^3, BGO is known as one of the densest crystals. This high density makes BGO a highly efficient detector for ionizing radiation such as gamma rays and X-rays. BGO has a high light output capability, meaning it can produce a significant amount of light when stimulated by ionizing particles. This property makes BGO an ideal material for light detectors in nuclear medical imaging and particle detection. BGO has high thermal stability and can operate without degradation at high temperatures. This property makes BGO suitable for applications that require performance in harsh environments, such as particle detection in space. BGO is widely available and can be easily obtained in various shapes and sizes [8].

LYSO is a type of scintillator crystal that is increasingly used in PET imaging due to its superior physical properties compared to traditional crystals like BGO [9].

BGO and LYSO are two popular crystals used for photon detection in PET imaging. Each crystal has its advantages and disadvantages, which should be considered when selecting the appropriate crystal for a specific application.

Density: BGO has a density of 7.13 g/cm^3, while LYSO has a density of 7.1 g/cm^3. The higher density of BGO allows it to detect higher energy photons more effectively.

Attenuation Length: BGO has a shorter attenuation length for 511 keV (1cm) compared to LYSO (1.2 cm). This means that BGO more effectively absorbs the light produced by positron particles, resulting in PET images with better spatial resolution.

Light Yield: BGO has a higher light yield (30,000 photons/MeV) compared to LYSO (8,000–10,000 photons/MeV). This means that BGO produces more light for each detected positron particle, leading to PET images with less noise.

Dead Time: BGO has a longer dead time (300 ns) compared to LYSO (37–45 ns). This means that BGO requires more time to reset after detecting a positron particle before it can detect the next particle. This can affect the speed of PET imaging.

Durability: BGO is more durable compared to LYSO, making it more resistant to mechanical and chemical damage.

Sensitivity: BGO generally has higher sensitivity than LYSO due to its higher density, which allows it to absorb more photons.

Cost: LYSO is generally more expensive than BGO due to the rarer materials used in LYSO.

Applications: LYSO is popular for applications requiring high spatial resolution, such as imaging small tumors (Table 1).

Energy Deposition in Detector Materials:

Energy Deposition in Detector Materials is the process by which incoming particles, like gamma rays in PET imaging, transfer energy to a detector material (e.g., BGO or LYSO crystals). According to equation 1, the energy transfer produces light photons, which are converted into electrical signals for image reconstruction.

$$E_{dep}=E_{initial}\cdot e^{-\mu.x} \quad (1)$$

Where $E_{initial}$ is the initial photon energy, μ is the attenuation coefficient of the material, and x is the depth of interaction within the crystal. This relation can help quantify how material properties influence energy retention.

Spatial Resolution and Image Quality:

The resolution of PET images can be impacted by detector design and material. Equation 2 shows the spatial resolution based on detector size and geometry.

$$\text{Resolution}=\frac{K}{D} \quad (2)$$

Where k is a constant determined by detector properties, and D represents detector dimensions or separation distance

Detection Efficiency:

A formula 3 relating the detection efficiency to the crystal material and thickness could be helpful in the methodology section to show how these parameters affect sensitivity.

$$\eta=1-e^{-\mu.d} \quad (3)$$

Where η is the detection efficiency, μ the material's linear attenuation coefficient, and d the thickness of the crystal.

Noise and Signal-to-Noise Ratio (SNR):

The signal-to-noise ratio in terms of count rate and noise factors may help readers understand how different energy thresholds impact image clarity as shown in equation 4:

$$SNR=\frac{C}{\sqrt{C+N}} \quad (4)$$

Where C is the count rate (signal), and N is the noise or background counts.

Table 1 Comparison between the BGO and LYSO for PET Imaging [10].

Feature	BGO	LYSO
Density (g/cm³)	7.13	7.1
Attenuation Length for 511 keV (cm)	1	1.2 mm
Effective Atomic Number (Zeff)	74	60
Light Yield (photons MeV⁻¹)	30000	8000-10000
Dead Time (ns)	300	37-45
Peak Wavelength (nm)	480	420
Durability	High	Medium
Cost	Low	High

GEANT4 is an open-source software framework used for simulating the passage of particles through matter. GEANT4 is a complex tool that requires knowledge of programming and physics to use effectively. This powerful tool is utilized by physicists and engineers worldwide for simulating a wide range of applications [11].

Nuclear medicine systems utilize radioisotopes for both diagnosis and treatment of diseases.

Simulating these systems using tools like GEANT4 can lead to a better understanding of their performance, optimization of their design, and development of new therapeutic methods. In such simulations, various parameters can be studied, including absorbed dose in different tissue parts, dose distribution within tissues, distribution of alpha, beta, gamma, and neutron particles within tissues, production of radionuclides, and tracking their trajectories within the body, among others. This information enhances the understanding of radiation effects on cells and biological tissues, ultimately facilitating improvements in therapeutic methods. [12].

This research focused on several key performance parameters that influence the efficiency and precision of the crystals in PET systems. These include:

- Energy Deposition
- Decay Time
- Light Yield
- Energy Resolution
- Timing Resolution
- Detection Efficiency
- Photon Absorption and Light Yield Distribution

While energy deposition and decay time are essential in evaluating the basic performance of scintillation crystals, the inclusion of energy resolution, timing resolution, and detection efficiency allows for a more comprehensive comparison between BGO and LYSO

In this simulation, G4EmStandardPhysics was employed as the primary physics model to handle electromagnetic interactions, including processes such as ionization, excitation, and photon interactions. Additionally, G4DecayPhysics and G4RadioactiveDecayPhysics were utilized to accurately simulate particle decays, which are critical to this simulation due to the inclusion of decay processes.

The cutoff energy was set to the default value in Geant4, which corresponds to a range cutoff of 0.7 mm. This default cutoff ensures a balance between computational efficiency and the accuracy of the particle tracking.

II. MATERIAL AND METHODS

Both BGO and LYSO were modeled using the same simulation parameters (as shown in Table 2), where the homogeneous cylinder of brain tissue represented the patient. A total of 1000 events were simulated for each crystal type.

Table 2 Simulation specifications for the BGO and LYSO Crystals

Parameter	BGO $(Bi_4Ge_3O_{12})$	LYSO $(Lu_1.^8Yb_0.^2SiO_5)$
Dimensions	Length (dx) = 6 cm Width (dy) = 6 cm Thickness (dz) = 3 cm	Length (dx) = 6 cm Width (dy) = 6 cm Thickness (dz) = 3 cm
Number of Crystal Blocks	-	-
Density (g/cm^3)	7.13	7.1
Zeff	74	60
Decay Time (ns)	300	37-45
Patient Representation	Homogeneous cylinder of brain tissue	Homogeneous cylinder of brain tissue
Patient Position	Center of the complete detector	Center of the complete detector
Total Number of Simulated Events	1000	1000

The crystal_edep_event_Id chart examines the amount of energy deposited in each crystal for each simulated event. This chart facilitates the comparison of energy deposition patterns and distributions in PET images obtained with BGO and LYSO crystals. This information can be useful in improving the algorithms and methods for image reconstruction in PET imaging (Fig. 1 & Fig. 2).

The crystal_edep_event_cell chart shows the distribution of energy deposition in each crystal cell for each simulated event. This chart aids in identifying the points within each crystal that receive higher energy deposition. This information can be used to improve the accuracy and quality of PET images.

The crystal_edep_score chart assigns a score to each simulated event in the BGO and LYSO crystals based on specific criteria. These criteria can reflect the quality and performance of the crystals in PET imaging. The information obtained from this chart can be used to select the best crystal for use in PET imaging systems and to improve the quality and accuracy of the images.

III. RESULT

The results for the BGO and LYSO crystals have been obtained for 1000 events. These results include the following:

Crystal_edep_eventId shows the distribution of the number of energy depositions in the crystal based on the event ID (eventId). In other words, it indicates how many energy depositions occur in a particular crystal for different events.

For the LYSO crystal, the average number of events is 485.9 with a standard deviation of 287.7. This means that, on average, about 485.9 times energy is deposited in the LYSO crystal among various events, and this distribution has a relatively large spread with a standard deviation of 287.7.

Similarly, for the BGO crystal, the average number of events is 499.0 with a standard deviation of 288.1. This means that about 499.0 times energy is deposited in the BGO crystal among various events average, and this distribution also has a relatively large spread with a standard deviation of 288.1.

Based on these results, it can be concluded that the distribution of energy depositions in the BGO and LYSO crystals is on average close to each other. However, there are variations in their values which are reflected in their standard deviations.

Crystal_edep_cell indicates the distribution of the number of energy depositions in each individual crystal block within the PET detector crystal array. This chart visually shows which crystal blocks are more involved in the energy deposition process (Fig. 3 & Fig. 4).

For the BGO crystal, the average number of events in the crystal blocks is 13.14 with a standard deviation of 9.72. This means that for different blocks of the BGO crystal, on average, about 13.14 times energy is deposited in each block, and this distribution has a relatively large spread with a standard deviation of 9.72.

Similarly, for the LYSO crystal, the average number of events in the crystal blocks is 13.02 with a standard deviation of 9.873. This means that for different blocks of the LYSO crystal, on average, about 13.02 times energy is deposited in each block, and this distribution also has a relatively large spread with a standard deviation of 9.873.

Based on these results, it can be concluded that the distribution of energy depositions in the blocks of BGO and LYSO crystals is on average close to each other. However, there are variations in their values. This indicates that the energy deposition process in crystals is not random and depends on various factors such as crystal geometry, particle type, and energy.

Crystal_edep_score shows the distribution of energy deposition events based on energy levels (MeV). This chart indicates how many of the energy depositions have different energy levels (Fig. 5 & Fig. 6).

For the BGO crystal, the average number of energy deposition events is 0.3887 with a standard deviation of 0.1592. This means that for energy depositions in the BGO crystal, the average number of events is about 0.3887 times, and this distribution has a relatively large spread with a standard deviation of 0.1592.

Similarly, for the LYSO crystal, the average number of energy deposition events is 0.3929 with a standard deviation of 0.1578. This means that for energy depositions in the LYSO crystal, the average number of events is about 0.3929 times, and this distribution also has a relatively small spread with a standard deviation of 0.1578.

Based on these results, it can be concluded that the distribution of energy deposition in the BGO and LYSO crystals differs at various energy levels. Additionally, the LYSO crystal has less dispersion in the number of events compared to the BGO crystal, suggesting that its distribution is more concentrated and less scattered.

This table summarizes the findings from the GEANT4 simulation for LYSO over 1000 events (table 3 & table 4).

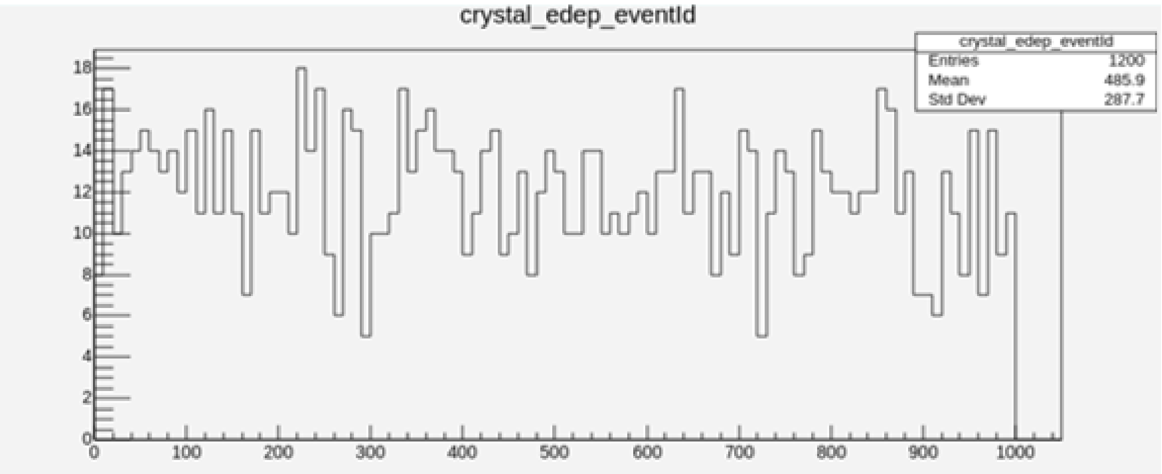

Fig. 1 Crystal_edep_eventId related to LYSO crystal

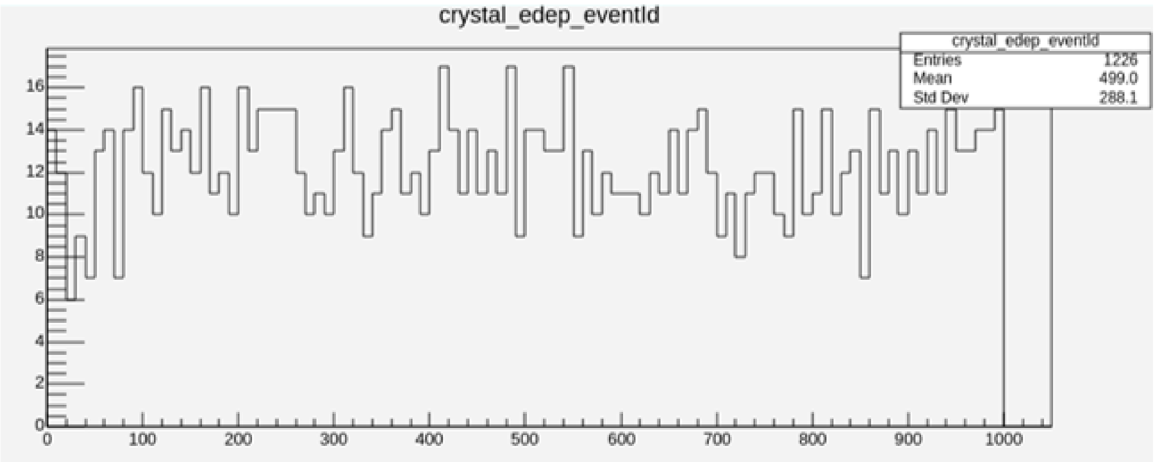

Fig. 2 Crystal_edep_eventId related to BGO crystal

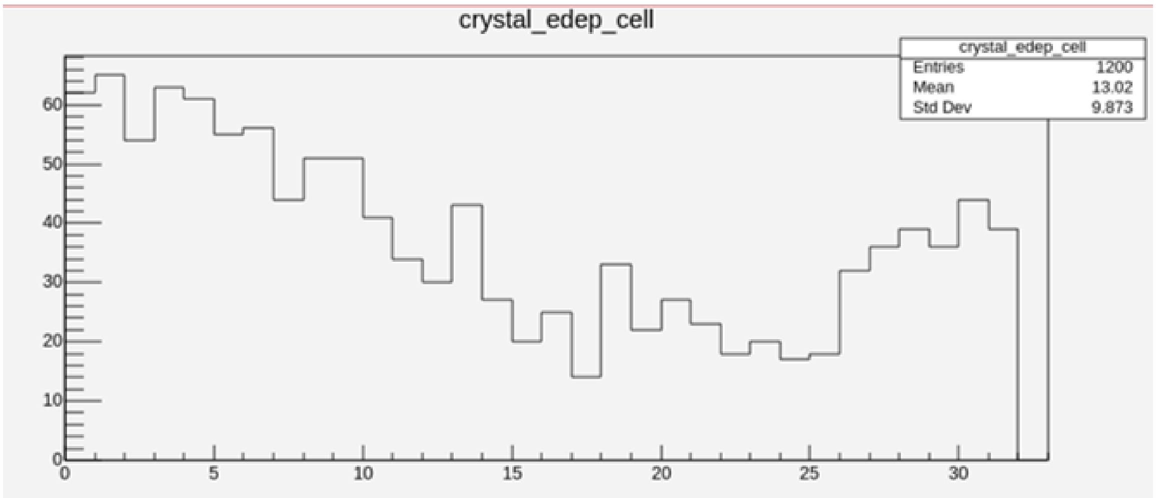

Fig. 3 Crystal_edep_ cell related to LYSO crystal

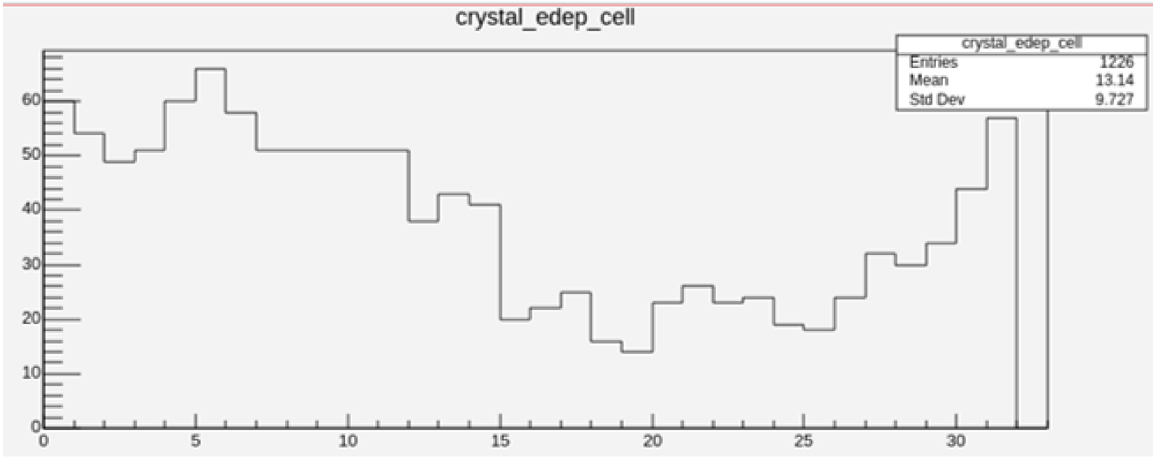

Fig. 4 Crystal_edep_ cell related to BGO crystal

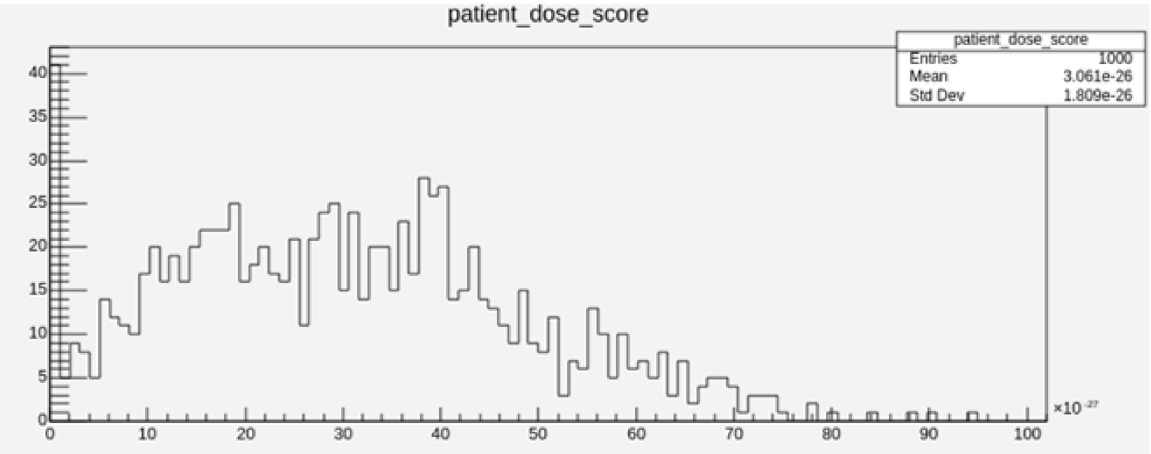

Fig. 5 Patient_dose_score related to BGO crystal

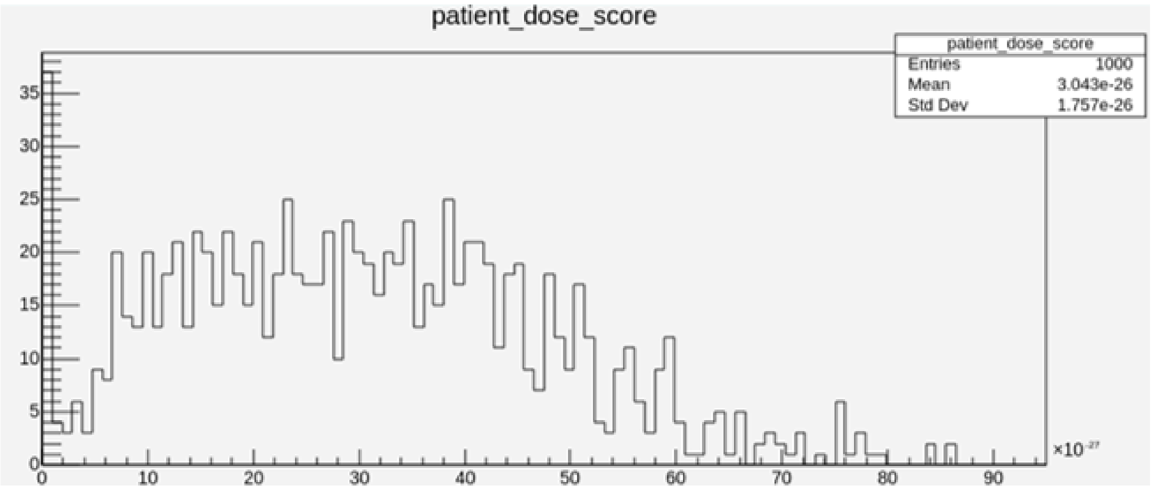

Fig. 6 Patient_dose_score related to LYSO crystal

TABLE 3 THE FINDINGS RESULT FROM THE GEANT4 SIMULATION FOR LYSO FOR 1000 EVENTS

LYSO	**Crystal_edep eventId**	
	Entries	1200
	Mean	485.9
	Std. Dev	287.7
	Crystal_edep cell	
	Entries	1200
	Mean	13.02
	Std. Dev	9.873
	Crystal_edep score	
	Entries	1200
	Mean	0.3929
	Std. Dev	0.1578
	Patient Dose_score	
	Entries	1000
	Mean	3.04326
	Std. Dev	1.75726

TABLE 4 THE FINDINGS RESULT FROM THE GEANT4 SIMULATION FOR BGO FOR 1000 EVENTS

BGO	**Crystal_edep eventId**	
	Entries	1226
	Mean	499
	Std. Dev	288.1
	Crystal_edep cell	
	Entries	1226
	Mean	13.14
	Std. Dev	9.727
	Crystal_edep score	
	Entries	1226
	Mean	0.3887
	Std. Dev	0.1592
	Patient Dose_score	
	Entries	1000
	Mean	3.06126
	Std. Dev	1.80926

IV. DISCUSSION

Several studies have discussed the benefits of using different crystals in detectors employed for radiation measurement. Additionally, some studies, due to the dependence of tomography on the characteristics of detector materials, are actively exploring the potential of innovative phosphors (scintillating materials). Therefore, it appears that most efforts are focused on the properties of materials with high density and high atomic number, such as their decay time.

However, some studies have failed to find useful experimental materials for PET phosphors [13]. Recently, some studies have discussed the modeling of materials for PET [14, 15], hoping that improving physical knowledge about scintillation processes can lead to the prediction of new phosphor material properties that may be useful for their modeling. Although the materials used for scintillation are slightly affected by temperature, they have wide applications in the field of radiation detection and protection in medicine [15, 16].

Moreover, some studies have combined known phosphors with new methods, such as phoswich detectors, which are made of two dissimilar phosphors in one detector to create new detectors [21]. Dahlbom and colleagues have researched LSO and NaI(Tl) layers for PET and SPECT, respectively [24]. The scintillation crystals used in PET are made of inorganic materials that can convert high-energy photon beams (511 keV) into a number of fluorescent photons [20]. In this study, the physical properties of two scintillation detectors, including BGO and LYSO, were examined using GEANT4 Monte Carlo simulation.

The comparison of BGO and LYSO in terms of energy deposition shows trade-offs between BGO's higher atomic number and LYSO’s superior energy resolution. While BGO absorbs more gamma-ray energy through the photoelectric effect, LYSO's improved resolution offers more precise energy measurements.

In this study, the performance of BGO and LYSO was compared by using GEANT4 simulations, focusing on key parameters such as energy deposition, decay time, energy resolution, and patient dose score. These findings indicate that although both crystals show similar energy deposition behaviors, they offer distinct advantages depending on the specific needs of the PET system.

Energy resolution was one of the key differences between the two crystals. LYSO outperformed BGO in energy resolution, as seen from its narrower distribution of energy deposition events. This improved resolution in LYSO is crucial for enhancing image quality and precision in PET imaging, making it an ideal choice for applications that require high spatial resolution, such as imaging small tumors or detecting fine details in the body.

BGO, on the other hand, demonstrated a higher energy deposition average, reflecting its higher light yield. This property makes BGO advantageous in terms of photon absorption and sensitivity, which can be useful for detecting weaker signals in high-energy environments. However, BGO's wider energy distribution resulted in a less clear distinction between energy levels, potentially leading to more noise in the resulting images compared to LYSO.

In GEANT4 simulations, which is a toolkit for modeling the passage of particles through matter, the number of events has a profound impact on the energy deposition in a PET system, reflecting real-world scenarios. GEANT4 facilitates the representation of particle interactions and energy deposition, where the number of events plays a pivotal role. In GEANT4 simulations for PET systems, the number of events is crucial in determining the accuracy, precision, and reliability of the simulated results. Increasing the number of events generally leads to more robust and informative simulations, which are essential for understanding system behavior and accurately interpreting simulated data.

V. CONCLUSION

This study compares the performance of BGO and LYSO scintillator crystals in PET imaging, using GEANT4 simulations. BGO showed higher energy deposition but lower energy resolution compared to LYSO. LYSO, with its better spatial resolution and shorter decay time, is advantageous for applications requiring high precision. The study's findings align with previous research, which has shown BGO's superior photon absorption but lower spatial resolution compared to LYSO. The choice between these crystals depends on the specific requirements of the PET system, including resolution, sensitivity, and cost. Further experimental studies are needed to validate these simulation results and optimize PET systems for improved diagnostic performance.

The PET system with LYSO shows effective performance, characterized by smoother shapes, a significant number of entries corresponding to the 511 keV energy level, and highly comparable absorbed dose values. However, BGO emerges as a stronger option, offering smoother shapes like LYSO, a notable distribution of interactions across different blocks, and clear superiority in terms of the number of interactions, mean values, and entries around 511 keV. Notably, BGO's superiority is further confirmed by its better performance in the number of entries, mean values, and interactions, indicating its potential as a more effective choice for PET imaging under simulated conditions

However, choosing between LYSO and BGO in PET systems involves trade-offs that encompass factors such as atomic number, density, decay time, light output, and cost. This decision depends on the unique needs of the PET system and takes into account factors such as energy resolution, sensitivity, cost, and overall performance. Evaluating priorities, whether emphasizing energy resolution, superior timing, cost-effectiveness, or other application-specific factors, is crucial. In practice, determining the "better" crystal involves aligning the choice with the specific needs and priorities of the PET system while considering the inherent strengths and trade-offs of each type of crystal.

ACKNOWLEDGMENT

This study does not involve any experiments or interventions on humans. Therefore, there is no need for informed consent from human participants. This study was conducted with the permission and support of Isfahan Islamic Azad University, Iran.

REFERENCES

[1] TOWNSEND D. W. et al. "Physical principles and technology of clinical PET imaging," Annals-Academy of Medicine Singapore, vol. 33, pp. 133-145, 2004.

[2] BASU Sandip, et al. "Fundamentals of PET and PET/CT imaging," Annals of the New York Academy of Sciences, vol. 1228, pp. 1-18, 2011.

[3] GUNDACKER S. et al. "Time resolution deterioration with increasing crystal length in a TOF-PET system," Nuclear Instruments and Methods in Physics Research Section A: Accelerators, Spectrometers, Detectors and Associated Equipment, vol. 737, pp. 92-100, 2014.

[4] MELCHER Charles L. "Scintillation crystals for PET," Journal of Nuclear Medicine, vol. 41, pp. 1051-1055, 2000.

[5] AHMED Abdella M., et al. "A validated Geant4 model of a whole-body PET scanner with four-layer DOI detectors," Physics in Medicine & Biology, vol. 65, pp. 235051, 2020.

[6] MARSDEN Paul K. "Detector technology challenges for nuclear medicine and PET," Nuclear Instruments and Methods in Physics Research Section A: Accelerators, Spectrometers, Detectors and Associated Equipment, vol. 513, pp. 1-7, 2003.

[7] TOWNSEND, David W., et al. A rotating PET scanner using BGO block detectors: design, performance and applications. Journal of Nuclear Medicine, 1993, 34.8: 1367-1376.

[8] TURKINGTON Timothy G. et al. "Performance of a BGO PET/CT with higher resolution PET detectors," In: IEEE Nuclear Science Symposium Conference Record, IEEE, vol. 4, pp.-1894, 2005.

[9] D.U. Junwei, et al. "Physical properties of LYSO scintillator for NN-PET detectors," In: 2009 2nd international conference on biomedical engineering and informatics. IEEE, pp. 1-5, 2009.

[10] D.U. Junwei, et al. "Performance comparison of dual-ended readout depth-encoding PET detectors based on BGO and LYSO crystals," Physics in Medicine & Biology, vol. 65, pp. 235030, 2020.

[11] BHATNAGAR Sonali, SIRISHAS. N. L. "GEANT4 & GAMOS—A particle implementation of high energy simulation toolkit to oncology therapy," In: Proceedings of the IEEE Students'

Technology Symposium. IEEE, pp. 25-30, 2014.

[12] MCNAMARA A. L. et al. "Towards optimal imaging with PET: an in silico feasibility study," Physics in Medicine & Biology, vol. 59, pp. 7587, 2014.

[13] STEINBERG Jeffrey. "MRI-Based Attenuation Correction for PET Reconstruction," PhD Thesis. The Ohio State University, 2008.

[14] ANDRIESSEN J. DORENBOS P. VAN EIJK C. W. E. "Calculation of energy levels of cerium in inorganic scintillator crystals," MRS Online Proceedings Library (OPL), vol. 348, pp. 355, 1994.

[15] DERENZO Stephen E. KLINTENBERG Mattias, WEBER Marvin J. "Ab-initio cluster calculations of hole formation and trapping in PbF/sub 2/and PbF/sub 4," In: 1998 IEEE Nuclear Science Symposium Conference Record. 1998 IEEE Nuclear Science Symposium and Medical Imaging Conference (Cat. No. 98CH36255). IEEE, pp. 163-167, 1998.

[16] ARIÑO-ESTRADA Gerard, et al. "Study of Čerenkov light emission in the semiconductors TlBr and TlCl for TOF-PET," IEEE transactions on radiation and plasma medical sciences, vol. 5, pp. 630-637, 2020.

[17] BERGER M. J. et al. "Stopping-power and range tables for electrons, protons, and helium ions, NIST Standard Reference Database 124," National Institute of Standards and Technology (NIST), Physical Measurement Laboratory (PML), 2017.

[18] BRUNNER S. E. SCHAART D. R. "BGO as a hybrid scintillator/Cherenkov radiator for cost-effective time-of-flight PET," Physics in Medicine & Biology, vol. 62, pp. 4421, 2017.

[19] CATES Joshua W. et al. "Improved single photon time resolution for analog SiPMs with front end readout that reduces influence of electronic noise," Physics in Medicine & Biology, vol. 63, pp. 185022, 2018.

[20] EFTHIMIOU Nikos, et al. "TOF-PET image reconstruction with multiple timing kernels applied on Cherenkov radiation in BGO," IEEE transactions on radiation and plasma medical sciences, vol. 5, pp. 703-711, 2020.

[21] PAGANO Fiammetta, et al. "Advances in heterostructured scintillators: toward a new generation of detectors for TOF-PET," Physics in Medicine & Biology, vol. 67, pp. 135010, 2022.

[22] ENOCH S. et al. "Design considerations for a new generation of SiPMs with unprecedented timing resolution," Journal of Instrumentation, vol. 16, pp. P02019, 2021.

[23] GOLA Alberto, et al. "NUV-sensitive silicon photomultiplier technologies developed at Fondazione Bruno Kessler," Sensors, vol. 19, pp. 308, 2019.

[24] KRATOCHWIL Nicolaus, GUNDACKER Stefan, AUFFRAY Etiennette," A roadmap for sole Cherenkov radiators with SiPMs in TOF-PET," Physics in Medicine & Biology, vol. 66, pp. 195001, 2021.

[25] Dirk Hellwig, N. C, S. B, et al. Artificial Intelligence and Deep learning for advance PET image reconstruction : state-of-the-art and future directions, 2023, 62.6:334-342

[26] Stephen Adler J.D, et al. "Advances in preclinical PET," vol. 52, pp. 308-402, 2022 .

[27] Fumio Hashimoto K.O , et al. 4D deep image prior: dynamic PET image denoising using an unsupervised four-dimensional branch convolutional neural network: vol. 66, pp. 015006, 2021.

[28] M.Dagar S.Parzych, et al. Comparative studies of sensitivities of space and full geometries of Total-Body PET scanners built from crystals and plastic scintillators, vol. 10 , pp 62, 2023.

THIS PAGE IS INTENTIONALLY LEFT BLANK.

IJBBE International Journal of Biophotonics & Biomedical Engineering Vol. 4, No. 1, Spring-Summer, 2024

Research Article

Optical Properties of Coupled Gold Nanoparticles: A Numerical Study for Photothermal Applications

V. Rajabpour [1] and R. Rasooli Saghai [1,] *

1 Faculty of Electrical and Computer Engineering, University of Tabriz, Tabriz, Iran

***Corresponding author: raharasouli98@gmail.com**

DOI: 10.71498/ijbbe/2024.1129191

ABSTRACT

Received: Aug. 15, 2024, Revised: Jan. 1, 2025, Accepted: Jan. 2, 2025, Available Online: Jan. 29, 2025

Photothermal therapy (PTT) using plasmonic nanoparticles, particularly gold, is a promising method for cancer cell ablation. However, optimizing the morphology and size of nanoparticles for efficient light absorption and heat conversion remains challenging. Plasmonic metamolecules, like gold nanodimers, demonstrate significant localized field enhancement and strong infrared light absorption. In this study, we investigate gold nanoparticles with spherical, rod, pyramid, and cubic morphologies in both monomeric and dimeric forms. For dimer structures, side-by-side and end-to-end couplings were considered. Our analysis includes parameters such as absorption cross-section, photothermal conversion efficiency (PCE), and field enhancement to compare the optical properties of these nanostructures within the first biological window. Our findings suggest that gold nanopyramids, with their suitable PCE, intermediate peak wavelength spacing in side-by-side and end-to-end dimers, and significant local field enhancement, are more controllable candidates for photothermal applications.

KEYWORDS

Photothermal Therapy, Localized Surface Plasmon Resonance, Gold Nanodimers, Nanorod, Nanopyramid, Nanocube, Field Enhancement.

I. INTRODUCTION

Photothermal therapy (PTT) has emerged as a promising minimally invasive technique for cancer treatment, leveraging the conversion of light energy into heat to ablate tumor cells [1, 2]. This method offers several advantages, including precise targeting and minimal damage to surrounding healthy tissues [3]. The unique properties of nanoparticles, particularly gold nanoparticles (AuNPs), have made them ideal candidates for enhancing the efficacy of PTT [4]. One of the key phenomena that underpin the effectiveness of AuNPs in PTT is localized surface plasmon resonance (LSPR), which occurs when conduction electrons on the nanoparticle surface oscillate in resonance with incident light [5]. The LSPR effect in metallic nanoparticles, such as gold, is highly sensitive to several parameters, including particle size, shape, and the dielectric environment [6]. These parameters significantly influence the absorption and scattering properties of the nanoparticles, thereby affecting their photothermal conversion efficiency (PCE) [7].

In the context of biomedical applications, the concept of biological windows is crucial [6]. These windows refer to specific wavelength ranges (typically in the near-infrared region) where biological tissues exhibit minimal absorption and scattering, allowing deeper light penetration [8]. This characteristic is essential for effective PTT, as it ensures that the therapeutic light can reach deeper-seated tumors [9]. The coupling of gold nanoparticles can further modify their optical properties, leading to enhanced LSPR effects and improved photothermal performance [10]. Coupled nanoparticles exhibit collective oscillations that can result in stronger electromagnetic fields and increased heat generation [11]. This phenomenon is particularly beneficial for PTT, as it can lead to more efficient tumor ablation with lower light doses.

Understanding the impact of nanoparticle coupling on their optical behavior is essential for optimizing their design for PTT applications [12]. The arrangement and distance between coupled nanoparticles can significantly influence their LSPR response, thereby affecting their overall photothermal efficiency [13]. Researchers have been investigating various configurations and materials to maximize the therapeutic potential of these nanoparticles. Several studies have explored the simulation and experimental validation of coupled gold nanoparticles to elucidate their enhanced optical properties. For instance, In [14], the authors demonstrated the superior photothermal efficiency of coupled AuNPs compared to isolated particles. In another work, Sahu et al. [12] highlighted the role of interparticle distance and arrangement in tuning the LSPR response of coupled nanoparticles. Several other studies have also investigated the optical behavior of coupled gold nanoparticles in the form of dimers and trimers [11, 15-18]. These studies underscore the potential of coupled gold nanoparticles in advancing photothermal therapy and other biomedical applications.

In this study, the optical behavior of gold nanoparticles in both monomer and dimer forms was investigated using the finite element method. Initially, the optical properties of monomeric gold nanoparticles with spherical, rod, cubic, and pyramidal morphologies, all having the same volume, were examined. The dimer structures were then formed such that the total volume of the two nanoparticles in the dimer was equal to that of the corresponding monomer. Subsequently, the optical behavior of these gold nanoparticle dimers was studied. Maintaining the same volume for both monomers and dimers helps in assessing the effect of nanoparticle concentration in photothermal applications. Additionally, examining various morphologies, which have not been extensively studied in previous research, can provide valuable insights into the field enhancement capabilities of these nanoparticles.

II. METODS

This study examines the optical behavior of gold nanoparticles with various morphologies in both monomer and dimer states within the first biological window (650-950 nm). The morphologies of spheres, rods, cubes, and pyramids were all designed with equal volumes, including the dimers, to provide a comparative perspective on the effect of nanoparticle concentration in photothermal applications. The radius of the monomeric gold nanosphere was set at 20 nm, and the geometric specifications of the other nanoparticles, including the length and diameter of the nanorod, the side lengths of the cube, and the tetrahedral pyramid, were chosen to have a volume equal to that of the sphere. The aspect ratio of the nanorod was set to 3 to ensure that the LSPR wavelength of the nanorod falls within the first biological window [19]. Numerous studies have reported the synthesis of gold nanoparticles with these morphologies [20-26]. Figure 1 shows the nanoparticles studied in this research. As shown in the figure, the distance between nanoparticles in the dimer structure was set to 1 nm to achieve the maximum field enhancement. Additionally, nanoparticles other than the nanosphere were arranged in two configurations to examine the effect of coupling (Figure 1a, second and third rows)

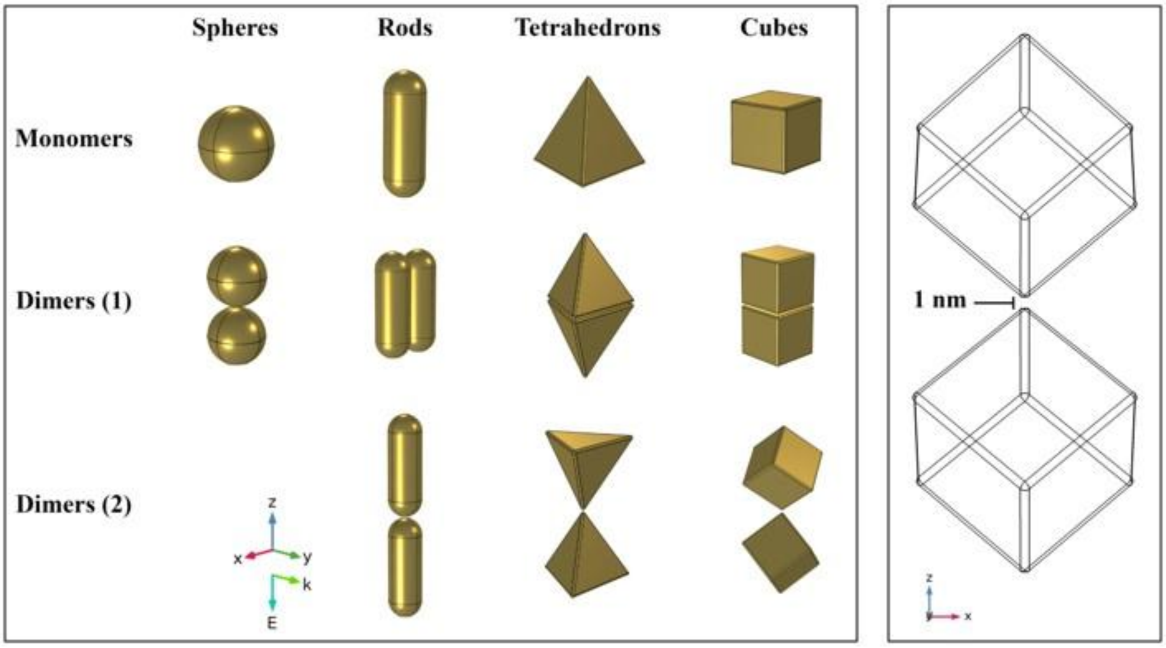

(a) (b)

Fig **1. a**) Gold nanoparticles with morphologies of sphere, rod, pyramid, and cube in two structures: monomer (first row) and dimer (second and third rows), **b**) The arrangement of gold Nanocubes in the “dimers (2)” structure with a distance of 1 nm.

A numerical framework employing the Finite Element Method (FEM), known as COMSOL Multiphysics [27, 28], was used to solve the wave equation within the frequency domain of biological windows.

$$\nabla \times \left(\frac{1}{\mu_r}\nabla \times E_{sca}\right) - k_0^2\left(\varepsilon_r - j\frac{\sigma}{\omega\varepsilon_0}\right)E_{sca} = 0, \qquad (1)$$

In equation (1), μ_r, ε_r, and σ represent the relative permeability, relative permittivity, and electrical conductivity of the materials, respectively. This equation provides the solution for the scattered field in terms of the local scattered electric field, E_{sca}. The total electric field, E, is the sum of the scattered electric field, E_{sca}, and the incident electric field, E_{inc}, around the nanoparticles. A spherical computational domain of water was created with the nanoparticle at its center. To prevent reflections from the water boundary, a perfectly matched layer (PML) with a thickness of 200 nanometers was applied to the outer edge of the water domain.

The solution for the scattered field was utilized to determine the optical cross-sections. The absorption, and scattering cross-sections (σ_{abs}, and σ_{sca}) for a nanoparticle are defined by the following equations.

$$\sigma_{abs} = \frac{W_{abs}}{I}, \qquad (2)$$

$$\sigma_{sca} = \frac{W_{sca}}{I}, \qquad (3)$$

Here, W_{abs} and W_{sca} represent the energies absorbed and scattered per unit time by the nanoparticle, respectively, while I indicates the intensity of the incident light.

$$I = \frac{1}{2} c\varepsilon |E_{inc}|^2, \tag{4}$$

Based on commonly referenced values in the literature [10], light intensity of 1 mW/µm^{-2} was selected. These values were applied uniformly to all samples to evaluate the performance of the nanostructures under identical conditions.

The numerical solutions are utilized to calculate the absorbed and scattered powers in equations (2) and (3) as shown in the following adjusted equations.

$$W_{abs} = \frac{1}{2} \iiint\limits_{V} Re[(\sigma E + j\omega D).E^{*} + j\omega B.H^{*}]\, dV, \tag{5}$$

$$W_{sca} = \frac{1}{2} \oiint_{S} Re[E_{sca} \times E_{sca}^{*}].ndS \tag{6}$$

In the equation, the symbols $*$ and D denote the complex conjugate and the electric displacement field, respectively. Equation (5) requires integration over the volume of the nanoparticle, while equation (6) involves a surface integral over a virtual boundary surrounding the nanoparticle. The calculations were performed using the built-in functions of COMSOL Multiphysics. The Drude model was applied to determine the standard dispersive permittivity of gold [29]. The refractive index of the surrounding medium, which was water in this case, was maintained at a constant value of 1.33.

III. RESULTS & DISCUSSION

A. *Absorption & Scattering Cross-sections*

The dimer structure of nanoparticles is designed so that the nanoparticles have the highest (dimer1) and lowest (dimer2) adjacent surface areas. Additionally, the volume of each dimer was equal to the volume of the corresponding monomer to compare the optical properties of coupled nanoparticles against single nanoparticles at the same concentration. Figure 2 shows the absorption and scattering cross-sections of monomer and dimer gold nanoparticles. As seen in the figure, the absorption cross-sections related to the nanorod morphology are the highest, while the lowest absorption cross-sections are for nanospheres. However, coupled gold nanospheres exhibit a larger absorption cross-section compared to monomeric nanospheres of the same volume. Additionally, this coupling results in a 142 nm shift in the LSPR peak wavelength.

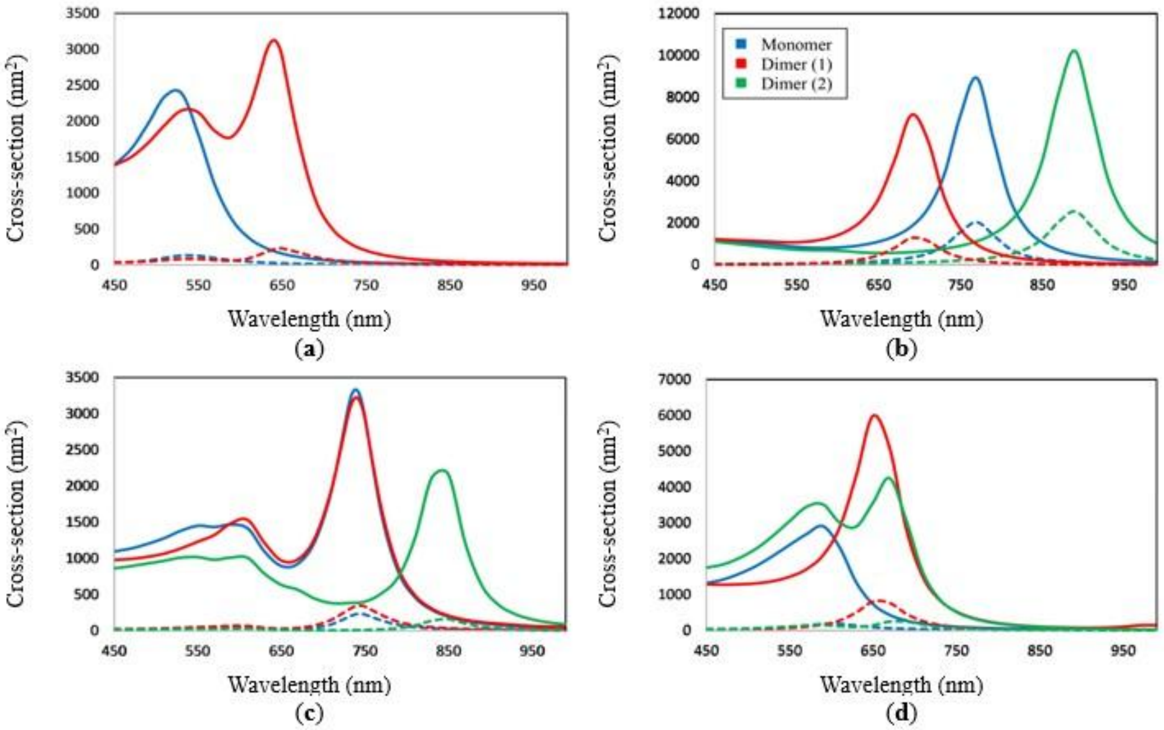

Fig **2.** Absorption and scattering cross-sections of monomer and dimer gold nanospheres (**a**), Nanorods (**b**), Nanopyramids (**c**), and Nanocubes (**d**). Solid lines and dashed lines indicate absorption cross-sections and scattering cross-sections, respectively.

In Figure 2b, it is notable that the side-by-side coupling of gold nanorods results in a lower LSPR than the same volume monomer and also reduces the LSPR peak wavelength. In contrast, end-to-end coupling of these nanoparticles increases the absorption and scattering cross-sections and the LSPR peak wavelength. It is observed that the difference in LSPR peak wavelength between the two coupled structures is about 200 nm. This difference will increase for Nanorods with Aspect Raito (AR) 4 and larger, such that the LSPR peak wavelength reaches the second biological window.

Considering the LSPR shifts in coupled nanorod structures and the specific laser wavelength for photothermal applications, maximum absorption by these nanoparticles may not occur, significantly reducing their efficiency.

The results of coupling nanopyramids are shown in Figure 2c. According to the figure, when coupled side-by-side, these gold nanoparticles exhibit optical behavior similar to that of a monomer nanoparticle of the same volume, such that there is no significant shift in the LSPR peak wavelength, nor a noticeable increase or decrease in the absorption cross-section. On the other hand, end-to-end coupling decreases the absorption cross-section but with an increase in the LSPR peak wavelength. The difference in LSPR peak wavelength between the two coupled structures in these nanoparticles is about 100 nm. This means that coupling nanopyramids is more controllable than coupling gold Nanorods and the LSPR of nanopyramids can be better tuned to the desired laser wavelength.

Coupling Nanocubes also increases the absorption cross-section (Figure 2d). As shown in the figure, side-by-side and end-to-end coupling of Nanocubes enhances the absorption cross-section by approximately 2 and 1.5 times, respectively, with the LSPR peak wavelength changes being around 10 nm, the smallest change among the nanoparticles studied in this work. However, the notable point is the LSPR range of these nanostructures, which is at the beginning of the first biological window. Given the LSPR peak wavelength of the monomer Nanocube, which is outside the first biological window range (590 nm), a dispersion of these Nanocubes may not show maximum absorption, making them unsuitable for photothermal applications. Nevertheless, Nanocubes have a larger cross-section compared to nanopyramids.

One of the other parameters for comparing the optical behavior of nanoparticles is the PCE value. This value is obtained by dividing the absorption cross-section of nanoparticles by the sum of their absorption and scattering cross-sections ($^{\sigma_{abs}}/_{\sigma_{abs}+\sigma_{sca}}$) [30]. Table 1 presents the results obtained from the simulations of this study for a better comparison of the optical properties of nanoparticles. As it is clear, dimer (2) gold Nanocubes have a higher PCE compared to other nanoparticles. In contrast, although gold nanorods have a larger absorption cross-section, they have a lower PCE.

TABLE1. OPTICAL PROPERTIES OF MONOMER AND DIMER GOLD NANOPARTICLES

Morphology	**Monomer**			**Dimer (1)**			**Dimer (2)**		
	LSPR peak wavelength (nm)	σ_{abs} (nm^2)	PCE (%)	LSPR peak wavelength (nm)	σ_{abs} (nm^2)	PCE (%)	LSPR peak wavelength (nm)	σ_{abs} (nm^2)	PCE (%)
Sphere	530	2386	94.8	642	3118.4	93.3	-	-	-
Rod	765	9013.4	81.3	694	7257.4	84.6	886	10301	79.9
Pyramid	739	3336.5	93.6	740	3213.7	90.2	841	2133.6	93.6
Cube	590	2894.4	94.3	654	6054.2	88	664	4302.8	95.1

Figure 3 illustrates the comparison of the LSPR peak wavelength and the absorption cross-section of gold Nanorod, Nanopyramid, and Nanocube dimers. According to this figure, as mentioned, the widest range of LSPR peak wavelength variations pertains to nanorod dimers. In contrast, the narrowest range of this wavelength variation is observed in Nanocube dimers, although the wavelengths related to these nanoparticles fall at the beginning of the biological window. This comparison can provide insight into how significant variations in the LSPR peak wavelength due to nanoparticle coupling can lead to the overall LSPR peak wavelength of all nanoparticles in a system deviating from the selected laser wavelength. Ultimately, this can reduce the system's efficiency in absorbing light and converting it into heat.

Figure 3 also shows the range of absorption cross-section variations of coupled nanoparticles. It is observed that the highest and lowest absorption cross-sections, as well as the widest and narrowest ranges of absorption cross-section variations, correspond to coupled Nanorods and Nanopyramids, respectively.

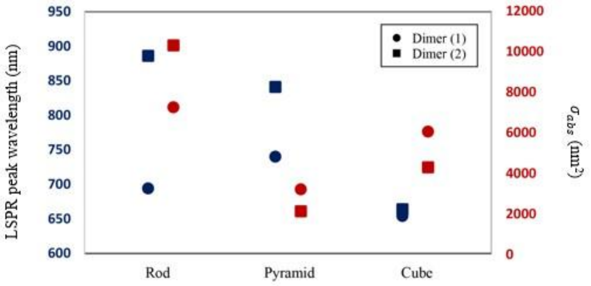

Fig **3.** Variation ranges of LSPR peak wavelength and absorption cross-section of coupled gold nanoparticles.

The variation ranges of LSPR peak wavelengths (indicated by blue symbols) and absorption cross-sections (shown by red symbols) for coupled gold nanoparticles are discussed. Dimeric Nanospheres display the most significant variation in LSPR peak wavelength, approximately 200 nm. In contrast, the coupling method for Nano-cubes shows little impact on their LSPR peak wavelength. Additionally, the changes in the absorption cross-section of dimeric Nanorods are more pronounced compared to those of other Nano-dimers. This suggests that the optical properties of rod-shaped gold nanoparticles are especially sensitive to the chosen coupling method.

B. *Localized Field Enhancement*

Another important feature in comparing the performance of plasmonic nanoparticles in photothermal applications is their ability to enhance the local field near them. This field enhancement can be utilized in applications such as imaging, Surface-Enhanced Raman Spectroscopy (SERS), biosensors, nonlinear optics, and controlled drug delivery. Figure 4 shows the improvement of the local field at the LSPR peak wavelength of the nanostructures studied in this work. As observed, side-by-side coupling results in a slight reduction in the field around the nanoparticles. In contrast, end-to-end coupling significantly enhances the field in the gap between the nanoparticles by several folds. This enhancement reaches over 30 times for gold nanospheres, about 15 times for nanorods, over 1.5 times for nanopyramids, and over 5 times for Nano-cubes. This comparison is more evident in Figure 5. According to the figure, gold nanopyramids, whether in monomer or dimer structures, improve the field around them more than other nanoparticles.

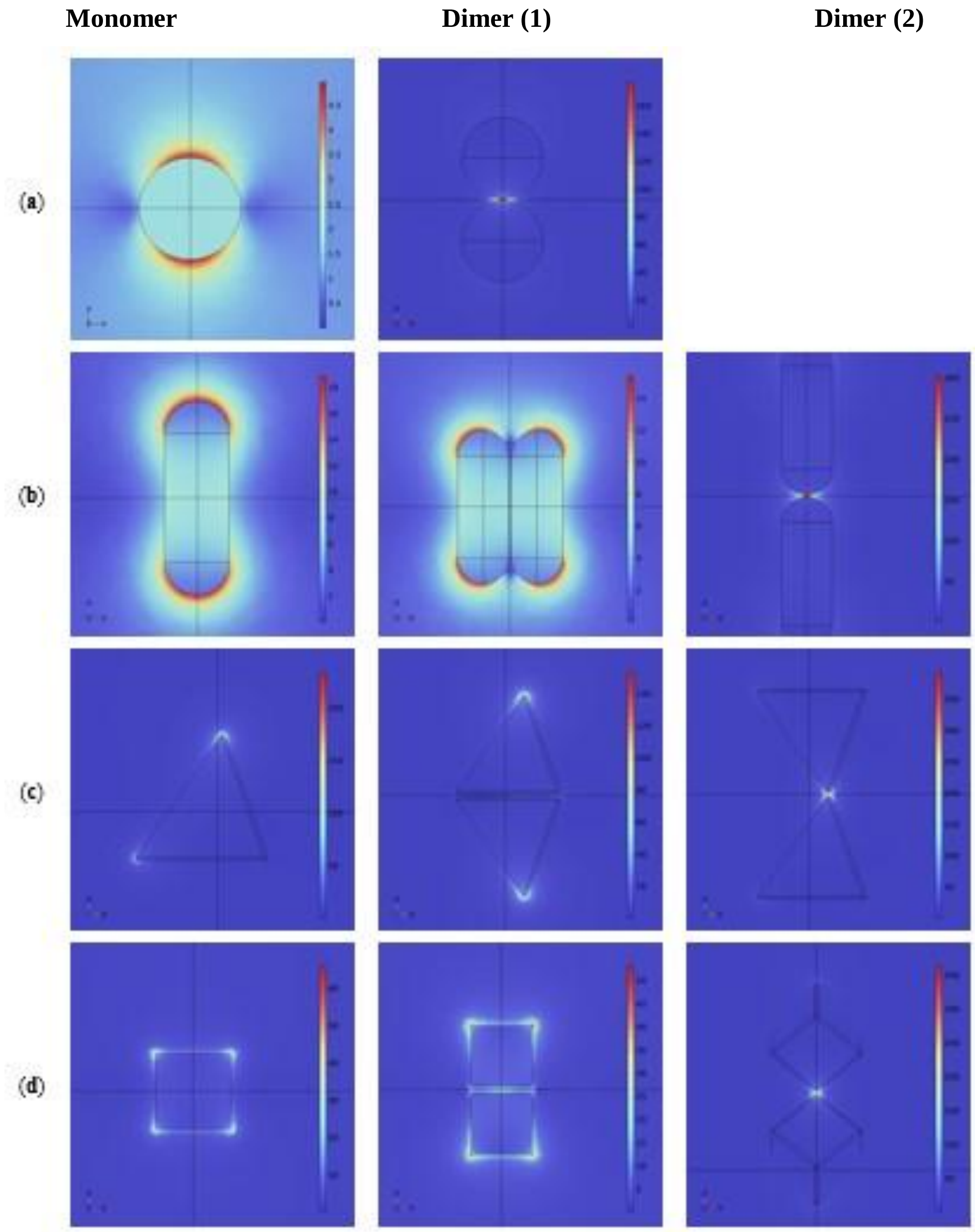

Fig **4.** Local field enhancement at the LSPR peak wavelength for gold Nanospheres (**a**), Nano-rods (**b**), Nano-pyramids (**c**) and Nano-cubes (**d**) in monomer and dimer configurations

(Note: all legends indicate the value of $|E/E_0|$.)

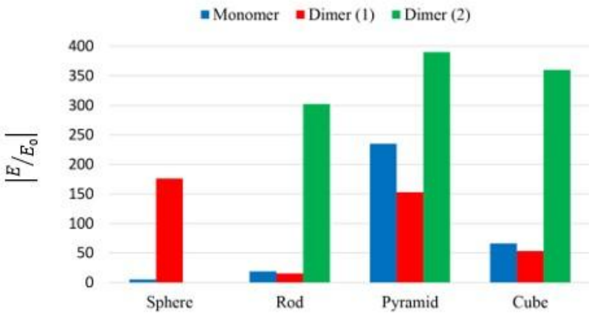

Fig **5.** Comparison of local field enhancement in gold monomer and dimeric nanostructures.

IV. CONCLUSION

In this study, we numerically investigated the optical behavior of gold nanoparticles with spherical, rod, pyramid (tetrahedral), and cubic morphologies in both monomer and dimer configurations for photothermal applications. The total volume of the dimer nanoparticles was kept equal to that of the monomer nanoparticles to provide insight into the effect of their concentration. Gold nanospheres, both as monomers and dimers, exhibited high PCE, but their LSPR peak wavelengths did not reach the first biological window. Gold nanorods, both as monomers and dimers, had the highest absorption cross-section but the lowest PCE. The LSPR peak wavelengths of coupled nanorods in side-by-side and end-to-end configurations were significantly different, making tuning the LSPR of these nanoparticles to the laser wavelength challenging. Gold nanopyramids showed the highest local field enhancement. Gold Nano-cubes also had high PCE values. When coupled, these nanoparticles had very close LSPR peak wavelengths, indicating that they can be tuned to the desired laser wavelength in either configuration. However, the LSPR peak wavelength of gold Nano-cube dimers was at the beginning of the first biological window, which could be a challenge for photothermal applications. Based on the results, gold tetrahedral nanopyramids can be considered the best candidates for photothermal applications due to their suitable PCE and their LSPR being in the first biological window. Additionally, there is a moderate difference in the LSPR peak wavelengths of these nanoparticles in side-by-side and end-to-end configurations. They also experience the highest field enhancement, especially in the end-to-end configuration.

Considering that the use of smaller nanoparticles increases the chance of their coupling, it can be said that these coupled nanoparticles exhibit significant optical properties compared to their monomer counterparts of the same volume. This includes the enhancement of the local field by dimer nanoparticles, which is several times greater than that of monomer nanoparticles. Additionally, the heat generated by these nanostructures can be calculated for further investigation.

REFERENCES

[1] Zhao L. Zhang X. Wang X. Guan X. Zhang W. and Ma J. "Recent advances in selective photothermal therapy of tumor," Journal of Nanobiotechnology, vol. 19, pp. 1-15, 2021.

[2] Zhang L. Oudeng G. Wen F. and Liao G. "Recent advances in near-infrared-II hollow nanoplatforms for photothermal-based cancer treatment," Biomaterials Research, vol. 26, pp. 61, 2022.

[3] Yu S. Xia G. Yang N. Yuan L. Li J. Wang Q. Li D. Ding L. Fan Z. and Li J. "Noble Metal Nanoparticle-Based Photothermal Therapy: Development and Application in Effective Cancer Therapy," International Journal of Molecular Sciences, vol. 25, pp. 5632, 2024.

[4] Dykman L. and Khlebtsov N. "Gold nanoparticles in biomedical applications: recent advances and perspectives," Chemical Society Reviews, vol. 41, pp. 2256-2282, 2012.

[5] Amendola V. Pilot R. Frasconi M. Maragò O. M. Iatì, and M. A. "Surface plasmon resonance in gold nanoparticles: a review," Journal of Physics: Condensed matter, vol. 29, pp. 203002, 2017.

[6] Lv Z. He S. Wang Y. and Zhu X. "Noble metal nanomaterials for NIR- triggered photothermal therapy in cancer," Advanced Healthcare Materials, vol. 10, pp. 2001806, 2021.

[7] Breitenborn H. Dong J. Piccoli R. Bruhacs A. Besteiro L. Skripka A. Wang Z. Govorov A. Razzari L. and Vetrone F. "Quantifying the photothermal conversion efficiency of plasmonic nanoparticles by means of terahertz radiation," Apl Photonics, vol. 4, 2019.

[8] Smith A. M. Mancini M. C. and Nie S. "Second window for in vivo imaging," Nature Nanotechnology, vol. 4, pp. 710-711, 2009.

[9] Wu X. Suo Y. Shi H. Liu R. Wu F. Wang T. Ma L. Liu H. and Cheng Z. "Deep-tissue photothermal therapy using laser illumination at NIR-IIa window," Nano-Micro Letters, 12, pp.1-13, 2020.

[10] Baffou G. and Quidant R. "García de Abajo, F. J., Nanoscale control of optical heating in complex plasmonic systems," ACS nano, vol. 4, pp. 709-716, 2010.

[11] Farooq S. Rativa D. and de Araujo R. E. "Quantitative analysis of high performance plasmonic metamolecules for targeted deep tissues applications," Plasmonics, vol. 18, pp. 2475-2482, 2023.

[12] Sahu A. K. and Raj S. "Understanding the Coupling Mechanism of Gold Nanostructures by Finite-Difference Time-Domain Method," International Journal of Nanoscience 2022, vol. 21, pp. 2250007, 2023.

[13] Pratap D. Shah R. K. Khandekar S. and Soni S. "Photothermal effects in small gold nanorod aggregates for therapeutic applications," Applied Nanoscience, vol. 12, pp. 2045-2058, 2022.

[14] Sahu A. K. and Raj S. "Effect of plasmonic coupling in different assembly of gold nanorods studied by FDTD," Gold Bulletin, vol. 55, pp. 19-29, 2022.

[15] Pal S. K. Chatterjee H. and Ghosh S. K., "Manipulating the confinement of electromagnetic field in size-specific gold nanoparticles dimers and trimers," RSC advances, vol. 9, pp. 42145-42154, 2019.

[16] Khoury C. G. Norton S. J. and Vo-Dinh T. "Plasmonics of 3-D nanoshell dimers using multipole expansion and finite element method," Acs Nano, vol. 3, pp. 2776-2788, 2009.

[17] Lipchus E. J. FEM Simulations of Plasmon Field Enhancement in Gold Nanoparticle Dimers and Gold Nanoparticle-Nanorod Dimers, University of Massachusetts Boston, 2023.

[18] Mencarelli E. Fanò L. Tarpani L. and Latterini L. "Modelling the optical properties of metal nanoparticles: analytical vs finite elements simulation," Materials Today: Proceedings, vol. 2, pp. 161-170, 2015.

[19] Rajabpour V. Abbasian K. and Ertugrul M. "Core-Shell Plasmonic Nanostructures for Hyperthermia of Cancer and Tumor Cells," Plasmonics, pp. 1-13, 2024.

[20] Sun M. Cheng Z. Chen W. and Jones M. "Understanding symmetry breaking at the single-particle level via the growth of tetrahedron-shaped nanocrystals from higher-symmetry precursors," ACS nano, vol. 15, pp. 15953-15961, 2021.

[21] Pérez-Juste J. Pastoriza-Santos I. Liz-Marzán L. M. and Mulvaney P. "Gold nanorods: synthesis, characterization and applications," Coordination chemistry reviews, vol. 249, pp. 1870-1901, 2005.

[22] Wang Y. Chen J. Zhong Y. Jeong S. Li R. and Ye X. "Structural diversity in dimension-controlled assemblies of tetrahedral gold nanocrystals," Journal of the American Chemical Society, vol. 144, pp.13538-13546, 2022.

[23] Yoo S. Youn G. Lee H. Kwon J. S. Lee Y. and Lee S. "Synthesis of ultra- small gold nanorods: Effect of reducing agent on reaction rate control," Bulletin of the Korean Chemical Society, vol. 44, pp. 648-652, 2023.

[24] Huang C.-J. Wang Y.-H. Chiu P.-H. Shih M.-C. and Meen T.-H. "Electrochemical synthesis of gold nanocubes," Materials Letters, vol. 60, pp. 1896-1900, 2006.

[25] Khan A. W. Lali N. S. Sabei F. Y. Irfan M. I. Naeem-ul-Hassan M. Sher M. Safhi A. Y. Alsalhi A. Albariqi A. H. ans Kamli F.

"Sunlight-assisted green synthesis of gold nanocubes using horsetail leaf extract: A highly selective colorimetric sensor for Pb2+, photocatalytic and antimicrobial agent," Journal of Environmental Chemical Engineering, vol. 12, pp. 112576, 2024.

[26] Schwartzberg A. M. Olson T. Y. Talley C. E. and Zhang J. Z. "Synthesis characterization, and tunable optical properties of hollow gold nanospheres," The Journal of Physical Chemistry B, vol. 110, pp. 19935-19944, 2006.

[27] Multiphysics C. *Introduction to comsol multiphysics®.* COMSOL Multiphysics, Burlington, MA, accessed 1998**.**

[28] Pryor, R. W., Multiphysics modeling using COMSOL®: a first principles approach. Jones & Bartlett Publishers: 2009.

[29] Johnson P. B. and Christy R.-W. "Optical constants of the noble metals," Physical Review B, vol 6, pp. 4370, 1972.

[30] Liu, Y. Kangas J. Wang Y. Khosla K. Pasek-Allen J. Saunders A. Oldenburg S. and Bischof J. "Photothermal conversion of gold nanoparticles for uniform pulsed laser warming of vitrified biomaterials," Nanoscale, vol. 12, pp. 12346-12356, 2020.

IJBBE *International Journal of Biophotonics& Biomedical Engineering* *Vol. 4, No. 1, Spring-Summer, 2024*

Research Article

Tumor interactional equation with biological and drug environment

R. Kian[a,b*], M. S. Zakerhamidi[a], N. Ebrahimpour[b]

[a] *Faculty of Physics, University of Tabriz, Tabriz, Iran*
[b] *Department of Chemical Industry, National University of Skills (NUS), Tehran, Iran*

***Corresponding author:** roshanak_kian@yahoo.com**

DOI: 10.71498/ijbbe.2024.1190438

ABSTRACT

Received: Nov. 13, 2024, Revised: Dec. 18, 2024, Accepted: Dec. 23, 2024, Available Online: Jan. 29, 2025

Today, chemotherapy is an aggressive form of chemical drug therapy meant to destroy cancerous tumors in the human body. Since the human body system can be considered as a solvent/biological environment, by obtaining effective interactional equations in anticancer drugs, real behavior interactional of these drugs in the body environment can be predicted. To this end, the spectroscopic technique is a promising investigative and diagnostic tool that can assist in uncovering the interactional equation of cancerous tumors and provide quantifiable molecular information for diagnosis and treatment evaluation. To investigate the interactional equation of cancerous tissues and the type of their interactional behavior, samples were taken from these tissues, and the mathematical model of cancerous tissue interaction was presented using Kamlet–Taft polarity parameters. This equation probes anticancer drug molecular interactional reactions with cancerous tumors in a sample to obtain information on their effective coefficient in the body and/or inter/intra molecular interactions. These interactions contain detailed information about the behavior of drugs used in cancer treatment and cancer tissues, which can be very useful for choosing treatment methods.

KEYWORDS

Spectroscopy, Biological environment, Cancerous tumor, Kamlet–Taft, Molecular interactions

I.INTRODUCTION

Cancer is the second-leading cause of death in the world and its genesis and progression are extremely complex. Cancer can be treated or stopped by chemotherapy, radiotherapy, and surgery procedures alone or in combination. Meanwhile, chemotherapy is a more effective and common treatment approach for cancer treatment, prevention of slow growth, and tumor reduction. The basics of chemotherapy include the use of drugs alone or in combination to inhibit cell proliferation and tumor growth [1],[2]. However, the emergence of new drugs and their drug resistance has turned the focus of scientists towards natural products including fruits, vegetables, teas, spices, and soy-based foods. Chalcone and its analogs are one of the privileged groups of natural compounds that are widely found in various plants. Chalcones (Fig.1) contain two aromatic rings (ring A and ring B) and α, β–unsaturated carbonyl group.

They have a delocalized π-electron-containing order in their aromatic rings. Chalcones are highly attractive molecules due to their broad biological activities with clinical potential against various diseases, especially for their anti-tumor activity. In addition, being inexpensive, available, and having low toxicity are a few advantages of chalcones, in comparison to other alternative medicinal compounds [3]–[5]. Many studies have shown anticancer activity of these compounds against various tumor cells. It has been found that the incorporation of different substituent groups on their two aromatic rings increases the anticancer and other activities [6]–[10].

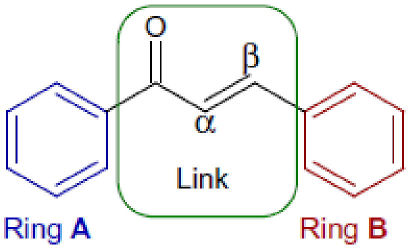

Fig. **1** Chalcone scaffold

Since the human body can be considered as a solvent/biological environment, by obtaining effective interactional equations in chalcone antitumor drugs, their real interactional behavior in the body environment can be predicted. When a drug is dissolved in various solvent environments, the solvatochromic effect occurs, and the spectrum of the substance changes. These spectral changes are due to drug-solvent interactions. Based on the studies, drug-solvent interactions could be non-specific, such as electrostatic, and/or specific in nature, such as electron donor-acceptor interactions or hydrogen bonding interactions [11]–[23]. To characterize these drug-solvent interactions, multiple regression analysis has been used, as proposed by Kamlet–Taft [24].

$$X = X_0 + a\alpha + b\beta + s\pi^* \qquad (1)$$

The Kamlet–Abboud–Taft (KAT) solvent polarity parameters consist of the solvent's dipolarity/polarizability (π^*) [25], solvent basicity (β) [26], and, solvent acidity (α) [27], X_0 is the regression intercept corresponding to the reference solvent or gaseous phase, and the coefficients *a*, *b*, and *s*, respectively, reflect the degree of regression for the interactions between the solvent's dipolarity/polarizability, solvent's basicity, and solvent's acidity.

In this experimental work, KAT polarity parameters (π^*, β, and α) of breast and brain tumors were reported with the solvatochromic method, using the DR_{II} and coumarin 504 standard probe. Moreover, interactional behavior of six different chemical structures of chalcone drug with these tumors was investigated. This behavior probes chalcone antitumor drug molecular interactional reactions with cancerous tumors in a sample to obtain information on their effective coefficient in the body and/or inter/intra-molecular interactions. These interactions contain detailed information about the behavior of chalcone drugs used in cancer treatment and cancer tissues, which can be very useful for choosing treatment methods.

II. EXPERIMENTAL SECTION

A. *Materials*

Synthesis and purification of the studied chalcones (Fig.2) were carried out as described in reference [28] and were used as solutes. Spectroscopy-grade solvent-sensitive standard dyes and coumarin 504 (Table 1) were obtained from Sigma Aldrich (Taufkirchen, Germany) and used without further purification. Disperse azo dye (DR_{II}) was synthesized and purified according to the common procedure in our laboratory and used as a probe.

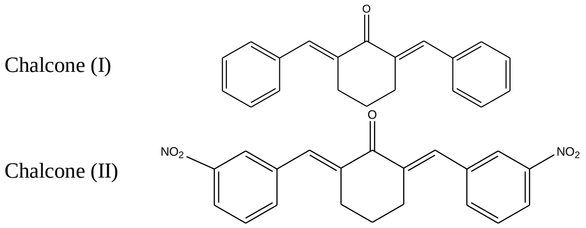

Chalcone (III)

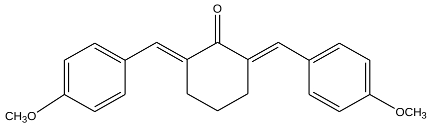

Chalcone (IV)

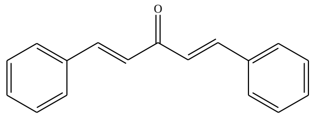

Chalcone (V)

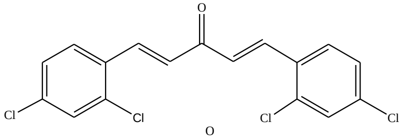

Chalcone (VI)

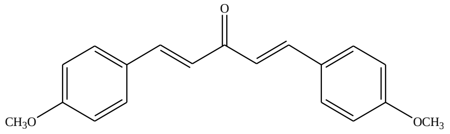

Fig.**2** Chemical structure of chalcones

TABLE 1: SOLVATOCHROMIC INDICATORS AND DYES USED

Dyes	Chemical structure
N, *N*-dimethyl-*4*-nitro aniline	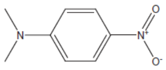
4-nitro aniline	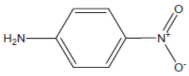
Reichardt's betaine dye 2,6-Diphenyl-4-(2,4,6-triphenyl-1-pyridinio) phenolate	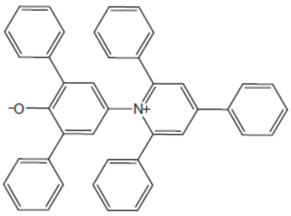
Coumarin 504 2,3,5,6-1*H*,4*H*-Tetrahydro-9-cabethoxyquinolizino-[9,9a,1-*gh*]coumarin	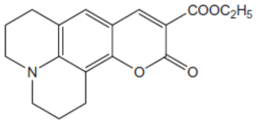
DR$_{II}$ 4-nitro-4-(*N*-ethyl, *N*-(2-(3-chloropropanoyloxy)ethyl azobenzene	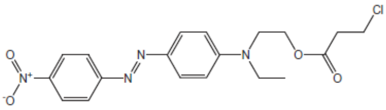

B. *Absorption spectroscopy*

After making an extremely dilute solution of polarity indicator dye, (10^{-5}M), the absorption spectra of 300–800 nm were recorded via a double beam Shimadzu UV-2450 Scan UV–visible spectrophotometer.

C. *Determination of the solvent polarity parameters via the solvatochromic method*

The solvatochromism technique was employed to define the KAT parameters with the wavenumber of the maximum absorption of each indicator expressed in kK (1000 cm^{-1}). To this end, we used all solvatochromic indicators listed in Table 1. After starting the experiment and recording the initial spectra, due to the fact that the absorption spectrum of two dyes, *4*-nitroaniline, and *N*, *N*-diethyl-*4*-nitroaniline, is located in the ultraviolet region and it is not possible to continue working with these dyes, it is necessary to use an alternative dye with a suitable regression coefficient. Moreover, in some cases, Richard's dye was not dissolved in tissues. Therefore, suitable substitute dyes were used. For this reason, a study was conducted on the dyes of the azo and coumarin family. Azo family dyes are an important group of dyes that have attracted the attention of many researchers due to their linear structure, color stability, and interchangeable spatial forms [29],[30]. *DR$_{II}$* dye to replace *4*-nitroaniline and *N*, *N*-diethyl-*4*-nitroaniline, and Coumarin 504 dye to replace Richard's dye were investigated. Coumarin 504 has a good linear relationship with Richard's dye, making it possible to measure α and *E$_T$*(30) parameters with high accuracy. The obtained results are given in Figs.2, 3 and 4.

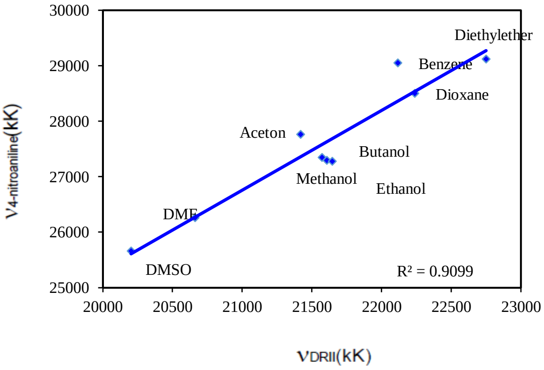

Fig.**3** Wavenumber of *4*-nitroaniline versus wavenumber of *DR$_{II}$*

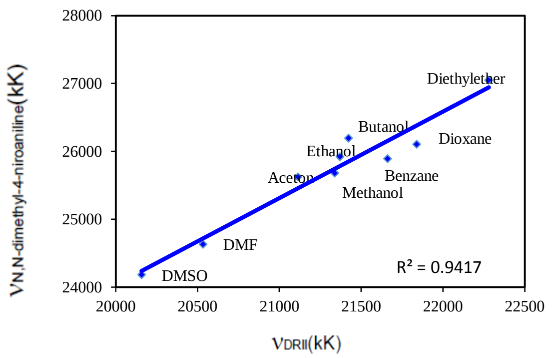

Fig.**4** Wavenumber of *N*, *N*-diethyl-*4*-nitroaniline versus wavenumber of *DR*$_{II}$

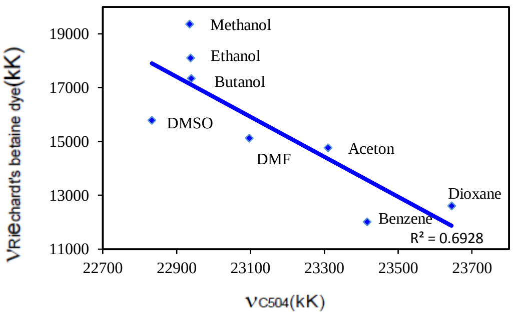

Fig.**5** Wavenumber of *N*, *N*-diethyl-*4*-nitroaniline versus wavenumber of *DR*$_{II}$

KAT parameters are calculated using the maximum absorption in the obtained absorption spectrum. In this case, the obtained maximum absorption wavelength from the recorded spectra is used as a wavenumber in cm^{-1} of 1000. The obtained relations from the above diagrams are respectively:

$$v_{(4-nitroaniline)} = 1.68v_{(DRII)} - 8402.40 = 0.95 \tag{2}$$

$$v_{(N,N-Dimethyl-4-nitroaniline)} = 1.19v_{(DRII)} + 594.39R = 0.98 \tag{3}$$

$$v_{(\mathrm{Reichardt-betaine-dye})} = -7.48v_{(C504)} + 188778R = 0.90 \tag{4}$$

After determining the wavenumber of the standard probe in each of the chalcone samples and tissues, the KAT and Reichardt parameters are calculated via the following relationships [29], [30]:

$$E_T(30) = \frac{28591.5}{\lambda_{\max(\mathrm{Reichardt})}} \tag{5}$$

$$E_T^N = \frac{E_T(30)_{Solvent} - 30.7}{32.4} \tag{6}$$

$$\pi^* = \frac{v_{(N,N-\mathrm{dimethyl}-4-nitroaniline)} - 28.18}{-3.52} \tag{7}$$

$$\beta = \frac{0.98v_{(N,N-\mathrm{dimethyl}-4-nitroaniline)} - v_{(4-nitroaniline)} + 3.49}{2.75} \tag{8}$$

$$\alpha = \frac{E_T(30) - 14.6\pi^* - 30.31}{16.5} \tag{9}$$

III. RESULTS AND DISCUSSION

A. *Preparation of tissue samples*

First, samples of cancer tissues that were removed from the patient's body during surgery were prepared. On the other hand, these tissues can have various contaminations, and at the same time, to make the tissues similar to the original structure, the conventional methods of cutting these materials in layers were avoided. On the other hand, it was not possible to confirm the cellular structure of the desired tissue due to the effect on the test process, and instead, the sample taken out of the patient's body was immediately washed completely with saline solution and a cut was made from its central part. Next, the extra parts, i.e. the surface parts of this tissue, were cut and removed with a microtome device. Then the sample was placed inside the standard dye solution. After one hour, a slice of the desired tissue that had absorbed the dye was obtained using a cutting method with a sharp blade and placing the sample inside the unolith. It should be noted that in absorption spectroscopy, the non-uniformity of the sample surface has no effect on the spectroscopic results. Therefore, there was no need for very high precision in uniform cutting. Furthermore, the samples should be transparent against the light transmission, and the examined samples have relatively good transparency in the wavelength range of 420 nm. As a result, the standard dyes that have absorption lower than this wavelength were replaced by using the linear comparison method with other reference dyes (C504 and DR_{II} dyes). The prepared slice with a diameter of about 1 mm and length and width of 3 and 1 cm, respectively was placed on the quartz cells and immediately the absorption spectrum of the sample was recorded in the range of 350 to 800 nm. Since the absorbed dyes have absorption between 450 and 650 nm, this wavelength range was chosen. The entire process was carried out in less than 10 minutes and each experiment was repeated eight times, and its average was reported.

B. ***Investigation of interactional behavior of cancerous tissues***

After obtaining the wavenumber of the used dyes in this experiment, these numbers were converted to the wavenumber of solvent polarity dyes to be used in the KAT equations. Using these wavenumbers the KAT equations of solvent polarity parameters for breast and brain tissues were calculated and the results are given in Tables 2 and 3.

TABLE2. SOLVATOCHROMIC POLARITY OF BREAST TUMOR AT ROOM TEMPERATURE

Breast Tumor	α	β	π^*	$E_T(30)$	E_T^N
1	0.26	0.54	0.55	42.69	0.37
2	0.33	0.55	0.56	43.66	0.40
3	0.29	0.58	0.62	44.31	0.42
4	0.35	0.68	0.81	48.20	0.54
5	0.49	0.49	0.46	45.44	0.46
6	0.36	0.57	0.61	45.39	0.45
7	0.27	0.50	0.48	42.15	0.35
8	0.28	0.52	0.50	42.21	0.35
Average	0.33	0.55	0.57	44.25	0.37

TABLE3. SOLVATOCHROMIC POLARITY OF A BRAIN TUMOR AT ROOM TEMPERATURE

Brain Tumor	α	β	π^*	$E_T(30)$	E_T^N
1	0.80	0.86	0.09	43.52	0.39
2	1.44	0.73	0.89	67.04	1.12
3	1.66	0.69	0.82	69.65	1.20
4	1.56	0.64	0.73	66.65	1.11
5	0.72	0.63	0.04	41.56	0.33
6	0.56	0.55	0.08	41.80	0.34
7	0.63	0.59	0.07	41.50	0.33
8	0.87	0.72	0.16	40.35	0.30
Average	0.95	0.57	0.36	51.50	0.64

As expected, the obtained values for breast tumors show that β and π^* values are higher than α values (Table 2). On the other hand, according to our previous research [4] the effective coefficients of β and π^* in chalcones I, II, and III (*b* and *s*) are higher than the other chalcones. Therefore, the absorption of these chalcones (I, II and III) is more than others, and hence it is better absorption in the breast tissue. Therefore, the interactional equation for breast tissue is:

$$X = 31240 - 130\alpha - 390\beta - 750\pi^* \tag{9}$$

In contrast, the obtained values for brain tumors have different trends. They show that α and β values are higher than π^*values (Table 3). Based on our previous research [5] the effective coefficients of α and β in chalcones IV, V, and VI (*a* and *b*) are higher than the others. As a result, the absorption of these chalcones (IV, V, and VI) is greater than other chalcones. Meaning that they have better drug effectiveness. Therefore, the interactional equation for brain tissue is:

$$X = 31598 - 476\alpha - 328\beta - 747\pi^* \tag{10}$$

IV.CONCLUSION

Chalcone is well known in the medicinal fields as an important antitumor drug. The presence of different functional groups in the chemical structure of chalcones leads to their different biological, medicinal, and therapeutic characteristics. In this experimental work, KAT polarity parameters (π^*, β, and α) of breast and brain tumors were obtained through the solvatochromic method using the DR_{II} and coumarin 504 standard probe. In addition, interactional behaviors of six chalcones with different substituent groups in their chemical structures with these tumors were investigated. Our results indicate the interesting properties of chalcone antitumor drugs and their performance based on different substituent groups can be modified in different biological environments. Consequently, chalcone with its unique structures can be used as a good candidate for treating different tumor tissues.

REFERENCES

[1] R.L.Siegel, A.N. Giaquinto, A. Jemal, “Cancer statistics,” CA: a cancer journal for clinicians. CA Cancer J Clin.; Vol.74, pp.12–49, 2024.

[2] D.T.Debela, S.G.Muzazu, K.D.Heraro, M.T.Ndalama, B.W.Mesele, D.C.Haile, S.K.Kitui, and T.Manyazewal, “New approaches and procedures for cancer treatment: Current perspectives,” SAGE open medicine, Vol.9, pp. 20503121211034366, 2021.

[3] N.A.Elkanzi, H.Hrichi, R.A.Alolayan, W.Derafa, F.M.Zahou, and R.B.Bakr, “Synthesis of chalcones derivatives and their biological activities: a review,” ACS omega, Vol 7, pp. 27769–27786, 2022.

[4] R. Kian, M.S. Zakerhamidi, A. N. Shamkhali, E. Kashani, and N.N. Pesyan, “Investigation of interactional behavior and relative photo-physical properties in a group of bioactive compounds,” Journal of Photochemistry and Photobiology A: Chemistry, Vol. 381, pp.111873, 2019.

[5] R. Kian, M.S. Zakerhamidi, A. N. Shamkhali, E. Kashani, “Study of the variation of intra/intermolecular interactions and configuration of a group of Enone anticancer drugs as a result of solvation,” Journal of Molecular Liquids, Vol. 274, pp.1–14. 2019.

[6] A.A. WalyEldeen, S. Sabet, H.M. El-Shorbagy, I.A. Abdelhamid, and S.A. Ibrahim, “Chalcones: Promising therapeutic agents targeting key players and signaling pathways regulating the hallmarks of cancer,” Chemico-Biological Interactions, Vol. 369, pp.110297, 2023.

[7] H.M.Abosalim, M.A.Nael, and T.F. El-Moselhy, “Design, synthesis and molecular docking of chalcone derivatives as potential anticancer agents,” ChemistrySelect, Vol. 6, pp.888–895, 2021.

[8] A.A.WalyEldeen, S.Sabet, H.M. El-Shorbagy, I.A.Abdelhamid, and S.A.Ibrahim, “Chalcones: Promising therapeutic agents targeting key players and signaling pathways regulating the hallmarks of cancer,” Chemico-Biological Interactions, Vol. 369, pp.110297, 2023.

[9] S. Shukla, A. K. Sood, K. Goyal, A. Singh, V. Sharma, N. Guliya, S. Gulati, and S. Kumar, “Chalcone scaffolds as anticancer drugs: a review on molecular insight in action of mechanisms and anticancer properties,” Anti-Cancer Agents in Medicinal Chemistry (Formerly Current Medicinal Chemistry-Anti-Cancer Agents), Vol. 21, pp.1650–1670, 2021.

[10] Y. Ouyang, J. Li, X. Chen, X. Fu, S. Sun, and Q. Wu, “Chalcone derivatives: role in anticancer therapy,” Biomolecules, Vol. 11, pp.894, 2021.

[11] P. Mehnati, H. Khoshsima, M.S.Zakerhamidi, R.Kian, M.Sahrai, “Solution environment effects on the photo-physical behavior of Daunorubicin and Mitoxantrone: Anthraquinone-based drugs,” Journal of Molecular Structure, Vol. 1310, pp.138317, 2024.

[12] H.Sahrai, R. Kian, A.N. Shamkhali, R. Kheradmand, M. S. Zakerhamidi, “Evaluation of solvent effect on the effective interactions of Isotretinoin and Tretinoin: Isomeric forms of vitamin A,” Heliyon, Vol. 10. pp.e25174, 2024.

[13] A.Moayedniya, A.G.Gilani, M.S Zakerhamidi, H.Dezhampanah, and R.Kian, “Investigation of the effective interactions of two bioactive compounds in different media,” J.Mol. Struct. Vol. 1274, pp.134534, 2023.

[14] R. Kian, M.S. Zakerhamidi, S. A. Kandjani, and M.Dadashzadeh, “The effective interactions of Fuchsine and Pararosaniline as two bioactive compounds in different solvent media: A comparative study,” J. Mol. Struct, Vol. 1264, pp. 133285, 2022.

[15] R.Kian, M.S.Zakerhamidi, A.N.Shamkhali, and E.Kashani, “Study of the variation of intra/intermolecular interactions and configuration of a group of Enone anticancer drugs as a result of solvation,” J. Mol. Liq. Vol. 274 , pp. 1–14, 2019.

[16] R.Kian, M.S.Zakerhamidi, A.N.Shamkhali, E.Kashani, and N.N.Pesyan, “Investigation of interactional behavior and relative photo-physical properties in a group of bioactive compounds,” J Photochem Photobiol A Chem, Vol.381, pp.111873, 2019.

[17] R.Kian, M.S.Zakerhamidi, A.N.Shamkhali, and P.Nesari, “The interactional behaviors and photo-physical properties of two triarylmethane drugs in solvent media," J. Mol. Liq. Vol. 225, pp.653–661, 2017.

[18] R.Kian, M.S.Zakerhamidi, A.N. Shamkhali, R.Teimuri–Mofrad, and K.Rahimpour, "Media and solute–solvent interaction effects on the photo–physical behavior of some drugs of 4H–Pyran derivatives," J. Mol. Liq, Vol. 238, pp. 508–517, 2017.

[19] İ.Sıdır, Y.G. Sıdır, H.Berber, and G.Türkoğlu, "Specific and non-specific interaction effect on the solvatochromism of some symmetric (2-hydroxybenzilydeamino) phenoxy Schiff base derivatives," J. Mol. Liq. Vol.215, pp. 691–703, 2016.

[20] R.Kian, M.S.Zakerhamidi, S.M. Seyed Ahmadian, and Gh. Babaie, "Photo-Physical Response of Two Triazole Compounds Against Solvent Polarity," Z. Phys. Chem, Vol. 230, pp.1575–1589, 2016.

[21] İ.Sıdır, Y.G. Sıdır, S.M.Berber, and F.Demiray, "Emerging ground and excited state dipole moments and external electric field effect on electronic structure. A solvatochromism and theoretical study on 2-((phenylimino) methyl) phenol derivatives," J. Mol. Liq. Vol. 206, pp. 56–67, 2015.

[22] R.Kian, S.M.Seyed Ahmadian, and M.S.Zakerhamidi, "Photo-physical properties of different types of vitamin A in solvent media," J. Mol. Struct. Vol.1080, pp 8–13, 2015.

[23] M. S. Zakerhamidi, M. Johari-Ahar, S.S. Ahmadian, and R. Kian, "Photo-physical behavior of some antitumor anthracycline in solvent media with different polarity," Spectrochimica Acta Part A: Molecular and Biomolecular Spectroscopy, Vol. 130, pp.257–262, 2014.

[24] C. Reichardt, *Solvents and Solvent Effects in Organic Chemistry*, 3rd ed, WILEYVCH, Weinheim, 2003.

[25] J. M. Abboud, M.J.Kamlet, and R.W.Taft, "Regarding a generalized scale of solvent polarities," J. Am. Chem. Soc, Vol. 99 , pp 8325–8327, 1977.

[26] M.J.Kamlet and R.W.Taft, "The solvatochromic comparison method. I. The .beta.-scale of solvent hydrogen-bond acceptor (HBA) basicities," J. Am. Chem. Soc, Vol. 98, pp. 377–383, 1976.

[27] M.J.Kamlet and R.W.Taft, "Linear solvation energy relationships. Part 3. Some reinterpretations of solvent effects based on correlations with solvent π* and α values," J. Chem. Soc. Perkin Trans.2, Vol. 3, pp. 349–356, 1979.

[28] N.N. Pesyan, S. Noori, S. Poorhassan and E. Şahin, "New spiro (thio) barbiturates based on cyclohexanone and bicyclo [3.1. 1] heptan-6-one by nonconcerted [1+ 5] cycloaddition reaction and their conformational structures," Bull. Chem. Soc. Ethiop. Vol.28, pp.423–440, 2014.

[29] M.S.Zakerhamidi, S.S. Ahmadian, and R. Kian, "The specific and nonspecific solvatochromic behavior of Sudan dyes in different solvents," Canadian Journal of Chemistry, Vol. 93(6), pp.639-647, 2015.

[30] M.S.Zakerhamidi and Sh. Shahrabi, "Solvatochromic solvent polarity parameters for the characterisation of some cyanobiphenyl nematic liquid crystals," Liquid Crystals 40, Vol.9, pp.1195–1201, 2013.

[31] M.S.Zakerhamidi and Sh. Shahrabi, "Determination of solvatochromic solvent polarity parameters for the characterization of some nematic liquid crystal in anisotropic and isotropic phases", Liquid Crystals 40, Vol.1 pp.22–30, 2013.

THIS PAGE IS INTENTIONALLY LEFT BLANK.

IJBBE International Journal of Biophotonics & Biomedical Engineering Vol. 4, No. 1, Spring-Summer, 2024

Research Article

Modeling Skin Tissue Scattering using the Henyey-Greenstein Method: A Study of Skin Conditions

M. Ranjbaran [a,*], Sh. Zokab [a], and Z. Farsi [a]

[a] *Department of Physics, Central Tehran Branch, Islamic Azad University, Tehran, Iran*

***Corresponding Author Email:** ma.ranjbaran@iau.ac.ir

DOI: 10.71498/ijbbe.2024.1190503

ABSTRACT

Received: Nov. 14, 2024, Revised: Dec. 26, 2024, Accepted: Dec. 29, 2024, Available Online: Jan. 29, 2025

Spectral reflectance from layered skin tissue as a function of wavelength can provide valuable information about the skin's optical properties for diagnosing skin conditions. Monte Carlo and Henyey-Greenstein (HG) are two methods to model scattering in skin layers. However, the HG method is a simpler and widely used technique that assumes a single parameter to characterize the scattering phase function. In this study, we conducted simulations of scattering in six-layered skin tissue using Zemax software based on the HG method. Our observations revealed increased penetration depth and back-scattered reflectance as the wavelength increased. We investigated reflectance patterns in different skin conditions by simulating mild solar damage, mild chronic dermatitis, and Mild solar damage with chronic inflammation. We recorded differences in the maximum intensity of reflected light in each condition. Additionally, we compared the backscattered reflections produced by incoherent and coherent light sources. The results of our HD simulation-based studies suggest that incoherent sources at infrared wavelengths could be advantageous for the analysis of skin disorders.

KEYWORD

Back-scattering, Henyey-Greenstein, Skin conditions, Spectral reflectance, Zemax software.

I. INTRODUCTION

Spectral reflectance analysis holds significant potential for diagnosing skin disorders, including melanoma detection, skin cancer diagnosis, and monitoring treatment response. When light interacts with skin tissue, it is both absorbed by chromophores like melanin and hemoglobin and scattered by cells and tissue [1]. This complex interplay between absorption and scattering is key to understanding skin properties. The skin's upper layers have a complex structure with unevenly distributed components like blood vessels and pigments. This makes it difficult to accurately measure the amount of these components using light, as the reflected light signal is a mixture of contributions from different components. Despite this challenge, reflectance spectroscopy is the most common method for analyzing the skin with light [2].

Two methods are used for the optical modeling of spectral reflectance from biological tissues:

the Monte Carlo method and the Henyey–Greenstein (HG) phase function. The Monte Carlo method simulates the individual paths of photons as they travel through the tissue. It tracks each photon's interactions with the tissue, including absorption, scattering, and reflection [3, 4]. This method is highly accurate but computationally expensive, especially for complex tissue structures. However, the Henyey–Greenstein (HG) Phase Function method treats the tissue as a whole scattering body, simplifying the modeling process. It uses an analytical formula (the HG phase function) to describe the overall scattering properties of the tissue, instead of tracking each photon individually [5, 6]. This approach is much faster but sacrifices some accuracy.

C. Ash and colleagues employed Monte Carlo modeling and found that penetration depth increases with wavelength, but larger spot sizes do not significantly increase penetration beyond a certain point, highlighting the importance of understanding light-tissue interactions for optimizing therapeutic techniques [7]. O. Kim and team utilized a stochastic photon transport model and reflectance spectroscopy to study normal and bruised skin. By simulating and comparing reflectance spectra, the model accurately predicts skin changes during bruise development, including peak concentrations of bilirubin and blood volume fraction [8]. H. Funamizu and collaborators used ray-tracing software and a GPU-based Monte Carlo method to simulate light propagation in human skin, capturing its complex structure [9]. Another study demonstrated that utilizing the stable HG phase function can significantly accelerate the calculation speed of light propagation through highly scattering materials by leveraging existing a priori knowledge on interaction processes [10]. Melnikova and colleagues applied the HG phase function to estimate the reflection function of a semi-infinite and conservative scattered layer, suitable for both direct and inverse problems in atmospheric optics assuming a plane atmosphere [11]. Also, error analysis using the HG phase function through multiple scattering was carried out by Zhao and colleagues [12].

This paper presents a novel approach to modeling spectral reflectance in skin tissue, leveraging the Henyey-Greenstein (HG) phase function. This function provides a robust approximation of light scattering in biological tissues, describing the probability of light deflection after each scattering event [5]. By focusing on the HG phase function, we aim to accurately quantify the wavelength-dependent scattering of spectral reflectance. To achieve this, we have developed a comprehensive simulation using Zemax software's Non-Sequential (NSC) data editor. Our model incorporated six distinct layers representative of skin tissue. By varying the wavelength of incident light, we have simulated its penetration depth and calculated the resulting reflectance using a rectangular detector.

Also, the skin properties of mild solar damage, mild chronic dermatitis, and mild solar damage with chronic inflammation were simulated, and maximum scattering intensity was obtained. Furthermore, the simulations were compared using incoherent and coherent light sources. This detailed analysis provides a thorough understanding of how light interacts with skin at different light wavelengths, and different skin tissue conditions, ultimately informing the development of more precise and effective diagnostic tools.

II. MATERIALS AND METHODS

The HG model offers a powerful tool for understanding light scattering in turbid media like biological tissues. This model utilizes a function that can predict various scattering patterns, ranging from backscattering to forward scattering, by adjusting one parameter, the anisotropy factor g, within the range $-1 \leq g \leq 1$. The angular distribution of scattered light is mathematically described as [5, 13]:

$$(\theta) = \frac{1}{4\pi}\frac{1-g^2}{[1+g^2-2g\cos(\theta)]^{3/2}} \qquad (1)$$

Where p(θ) represents a probability density function and θ ranges from 0 to π radians, indicating the angle between the photon's pre- and post-scattering directions. A value of θ = 0 rad denotes that the photon continues in its original direction post-collision.

TABLE 1. LENS DATA EDITOR OF SIMULATION

	Object Type	**Comment**	**Ref Object**	**Z Position**		**Z Length**	**Material (refractive index)**	**X Half Width**
1	Source File	AVAG-QSM-01-	0	-1.000		0.100	1.34	100
2	Rectangular Volume	Epidermis	1	0.000		0.100	1.4	10.000
3	Rectangular Volume	Papillary dermis	2	0.100	p	0.150	1.39	10.000
4	Rectangular Volume	Upper blood net dermis	3	0.150	P	0.100	1.4	10.000
5	Rectangular Volume	Reticular dermis	4	0.100	P	1.500	1.39	10.000
6	Rectangular Volume	Deep blood net dermis	5	1.500	P	0.100	1.44	10.000
7	Rectangular Volume	Subcutaneous fat	6	0.100	p	6.000	1.34	10.000
8	Detector	Small sensor	0	-0.200		100	ABSORB	5.000

TABLE 2. OPTICAL PROPERTIES OF HUMAN SKIN [4].

Wavelength(nm)	**Skin layer**	**Thickness(mm)**	**g**	**n**	$\mu_a(cm^{-1})$	$\mu_s(cm^{-1})$
600	Epidermis	0.1	0.85	1.34	0.015	40
	Papillary dermis	0.1	0.8	1.4	0.07	30
	Upper blood net dermis	0.15	0.9	1.39	0.1	35
	Reticular dermis	0.1	0.76	1.4	0.07	20
	Deep blood net dermis	0.1	0.95	1.39	0.1	35
	Subcutaneous fat	6	0.8	1.44	0.03	15

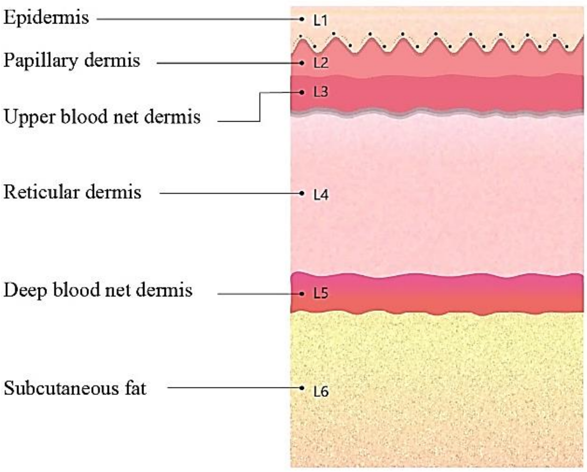

Fig. **1**. The model of six-layered skin tissue.

An isotropic medium is characterized by g = 0, indicating an equal likelihood for the photon to travel in any direction. Therefore, the outcome is influenced by the anisotropy factor g, which is denoted as g=⟨cos(θ)⟩ [14].

In the context of human skin, the HG model represents the skin as six distinct layers: the epidermis, papillary dermis, upper blood net dermis, reticular dermis, deep blood net dermis, and subcutaneous fat. These layers are modeled as rectangular volumes with no distance between them, effectively treating each layer as a continuation of the previous one (as shown in Fig. 1).

To simulate light scattering within the skin, the refractive index, thickness, and position of each skin layer as listed in Table 1, were inputted into the Lens data editor of Zemax software. Initial parameters within the "bulk scatter" module were then adjusted to model wavelength-dependent scattering. These parameters include: g, Mean path, and Transmission fraction. The mean path and transmission coefficients were calculated using the following equations [3]:

$$Mean\ path = \frac{1}{\mu_a + \mu_s} \tag{2}$$

$$Transmission = \frac{\mu_s}{\mu_a + \mu_s} \tag{3}$$

Where the absorption coefficient (μ_a) and scattering coefficient (μ_s) are fundamental parameters in light propagation through biological tissues. μ_a quantifies the absorption of light energy by the tissue, representing the conversion of photons into other forms of energy within the cells. Conversely, μ_s describes the scattering of light, characterized by the change in the direction of photons as they interact with tissue components. Table 2 presents the specific values of these coefficients used in a 6-layer skin model for a wavelength of 600 nm [15].

To determine the spectral reflectance, a rectangular detector with a 180° field of view, 5 mm in length, and 10^4 pixels was positioned 0.1 mm along the skin surface.

The modeling was performed in the non-sequential data editor of the Zemax simulation software. In the bulk scatter section of each layer's properties, based on Henyey-Greenstein-bulk.DLL, mean path and transmission values can be calculated based on substituting μ_a and μ_s in equations 2 and 3. By applying the coefficients g and n for each layer, representing the anisotropy factor and refractive index respectively, scattering within the skin layers for each wavelength can be observed by referring to ray tracing in the analysis section.

The coefficients g and n are dependent on the input wavelength. Simulations were conducted for wavelengths of 337, 442, 575, 600, 633, and 940 nm [15, 16]. The resulting spectral diagram illustrates the scattering intensity at each wavelength.

In every skin condition, changes in the thickness of skin layers lead to alterations in the structure of skin tissues, which are manifested in the scattering coefficients. To simulate the skin conditions, the thickness of each skin layer is altered in response to conditions like mild solar damage, mild chronic dermatitis, and mild solar damage with chronic inflammation [17]. Then the maximum back-scattering intensity was compared with normal skin.

III. RESULTS AND DISCUSSIONS

The angular distribution of HG-based scattered rays in the multilayered skin tissue is presented in Fig. 2. The NSC 3D layout shows the layered skin tissue including living epidermis, papillary dermis, upper blood net dermis, reticular dermis, deep blood net dermis, and subcutaneous fat.

The irradiation may undergo repeated scattering events within the skin tissue, with the scattered rays potentially traversing multiple times through the medium before being absorbed or emerging on the other side. As can be seen, the reflectance is obviously dependent on the wavelength of the irradiation source. The 337 nm irradiation reaches the epidermis skin layer, while the 633 nm irradiation penetrates the deeper layers, skin subcutaneous tissue [18].

To detect the back-scattered reflection, we incorporated a rectangular detector into the simulation. The detector was positioned at a small distance, 0.1 mm, from the skin's surface. The profile and intensity of back-scattered rays for incoherent irradiance at 337 nm, and 940 nm can be seen in Fig. 3. The concentrated light with higher intensity was detected at higher wavelength.

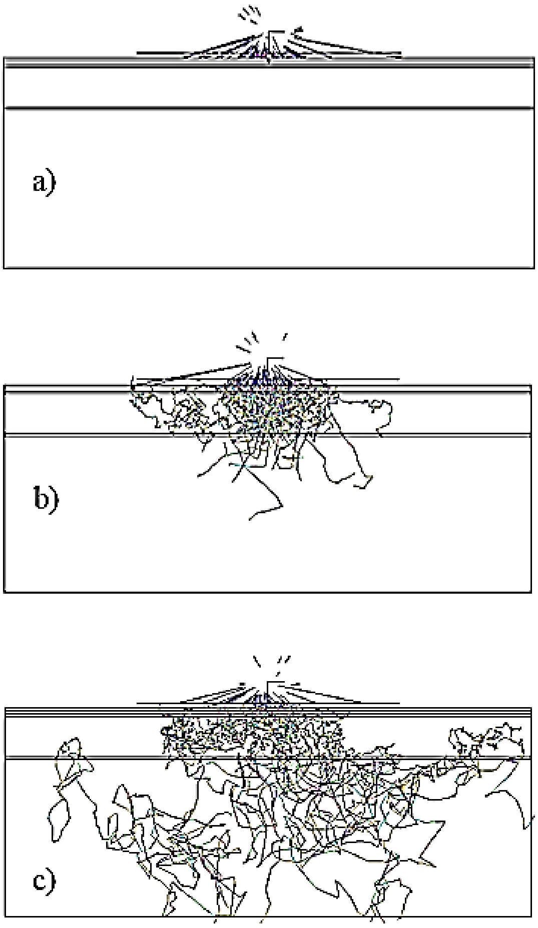

Fig. **2**. 3D layout of multilayered skin tissue at wavelength of a) 337 nm, b) 575 nm, and c) 633 nm.

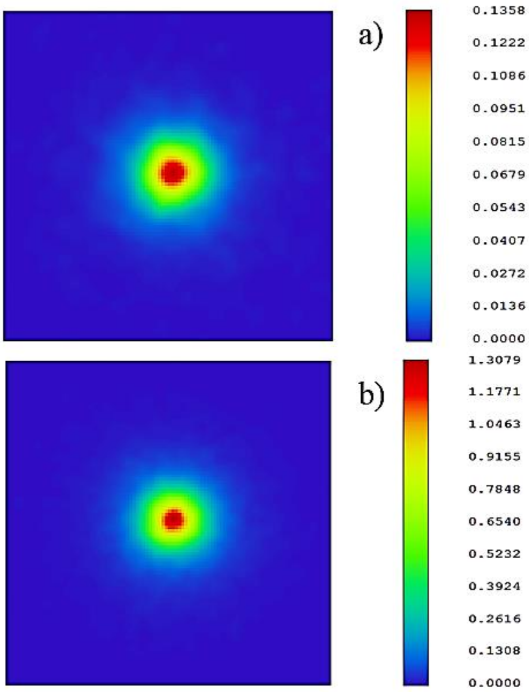

Fig. **3**. Detector view at wavelengths of a) 337 nm, and b) 940 nm.

To obtain the spectral reflectance from multilayered skin tissue, the incoherent irradiation sources at various wavelengths, λ, 337, 442, 575, 600, 633, and 940 nm were considered. We input the specific optical properties of each skin layer, $\mu_a(\lambda)$, $\mu_s(\lambda)$, g(λ), and n(λ), corresponding to each wavelength, into the Zemax software for simulation. The cross-section row of the detector viewer at each wavelength is depicted in Fig.4. It is obvious that the reflectance increased with increasing wavelength.

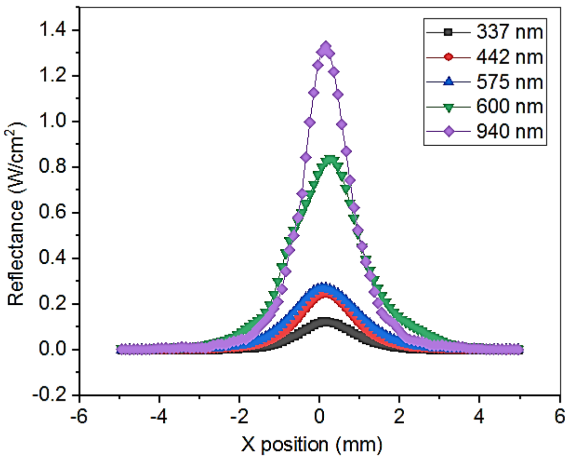

Fig. **4**. The back-scattered light profile at different wavelengths.

Fig.5 shows the peak intensity of the reflected light in the wavelength range of 337 to 940 nm. This figure shows an increase of around 600 nm due to more scattering by skin structures [3, 18]. While, at shorter wavelengths, light is more likely to be absorbed by melanin, Hemoglobin, and other chromophores in the skin, leading to reduced reflectance [20, 21]. This trend is significant because the interaction of light with these chromophores can provide insights into the skin's physiological conditions and overall health.

TABLE. 3. VARIATION OF SKIN LAYERS THICKNESS IN DIFFERENT SKIN CONDITIONS AND ASSOCIATED BACK-SCATTERING INTENSITY.

Skin conditions	**Thickness(mm)**					**Max back-scattering intensity**
	Epidermis	**Papillary dermis**	**blood net dermis**	**Reticular dermis**	**Deep blood net dermis**	
Normal skin	0.1	0.15	0.1	1.5	0.1	1.56
Mild solar damage	0.03	0.016	0.01	0.162	0.01	1.35
Mild chronic dermatitis	0.09	0.024	0.016	0.240	0.016	1.47
Mild solar damage, chronic inflammation	0.05	0.016	0.01	0.162	0.01	1.40

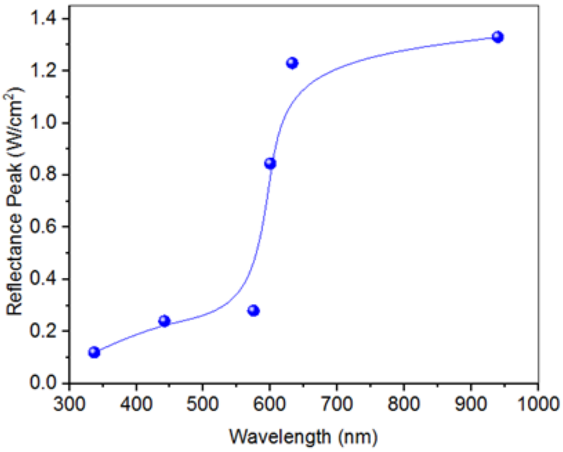

Fig. **5**. Reflectance peak as a function of wavelength.

As the penetration depth and the reflectance in the near IR regime (940 nm) were more, it was selected for more analysis. To analyze the reflectance in different skin conditions, in accordance with Table 3, the mild solar damage, mild chronic dermatitis, and mild solar damage with chronic inflammation were simulated and the maximum intensity of reflection was recorded. As can be seen, the thinner the layers become, the less reflection occurs [22]. Understanding these variations is crucial for developing non-invasive diagnostic tools that employ optical methods for skin analysis. Additionally, external factors such as illumination conditions, can also influence the peak intensity of reflected light. In Fig. 6, a comparison was made between the back-scattered reflections produced by incoherent irradiance (e.g., LED) and coherent irradiance (e.g., laser) at 940 nm. It is evident that while the peak intensity of back-scattered light is lower when using incoherent irradiance, it tends to be more isotropic, meaning the light is scattered uniformly in various directions.

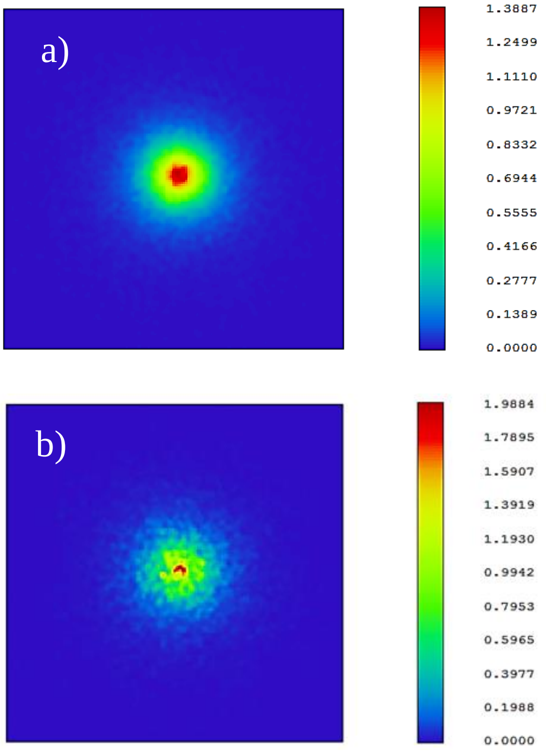

Fig. **6**. Detector view at wavelengths of 940 nm using a) incoherent irradiance, and b) coherent irradiance.

The backscattered laser light exhibited speckle patterns (fluctuations in intensity) due to the coherent nature of laser light. Variations in path length, resulting from multiple scattering and differing refractive indices within tissue layers, introduced phase shifts to the light waves. This phenomenon caused constructive and destructive interference between multiple scattered light waves, creating bright and dark spots [23, 24]. Furthermore, minor cellular movements or refractive index changes alter the interference pattern, causing observable speckle pattern fluctuations [25]. The speckles pattern could be utilized in the Laser speckle contrast imaging technique to monitor the dynamics of skin tissue [26].

Also, Fig. 7 illustrates a comparison of the cross-sectional row of backscattered reflections obtained using both incoherent (LED) and coherent (laser diode) illumination. This comparison reveals that employing a laser diode as the light source resulted in higher sensitivity compared to using an LED [27]. However, the laser diode illumination resulted in a non-uniform cross-sectional profile. Therefore, LEDs could be advantageous in the diagnosis and treatment of skin conditions [28].

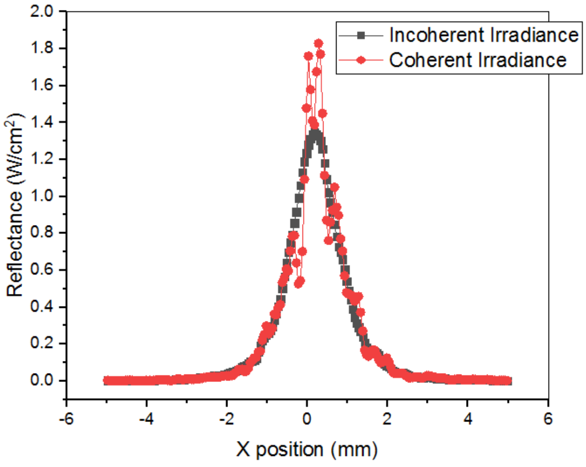

Fig. **7**. Cross section row of back-scattered reflection using incoherent irradiance, and coherent irradiance.

IV. CONCLUSION

Simulation allows researchers to study the optical properties of skin tissue in different conditions. Monte Carlo and Henyey-Greenstein methods are two alternative approaches to model scattering in skin layers. However, HG is a good alternative when complexity is not necessary. In this paper, based on the simulation of the skin layer's parameters in the HG method, the back-scattered reflectance was obtained at different wavelengths. Our results highlight the potential for using longer wavelengths to enhance light delivery and detection in the skin.

Also, different skin conditions such as mild solar damage, mild chronic dermatitis, and mild solar damage with chronic inflammation were simulated and the back-scattered reflectance intensity was recorded at the detector. The findings demonstrated that decreasing layer thickness led to a reduction in reflected light. Furthermore, when comparing coherent and incoherent light sources, we observed that coherent light resulted in a more intense reflection, but this reflection was distributed non-uniformly. Our results suggest that the HG method can be a valuable tool for optimizing light-based applications such as dermatological imaging, skin diagnostics, and phototherapy.

REFERENCES

[1] N. Kollias, G. Zonios, and G. N. Stamatas, "Fluorescence spectroscopy of skin. Vibrational Spectroscopy," Vol. 28, pp. 17-23, 2002.

[2] I. V. Meglinskii, "Monte Carlo simulation of reflection spectra of random multilayer media strongly scattering and absorbing light," Quantum Electronics, Vol. 31, pp. 1101, 2001.

[3] I. T. Maeda and N. Arakawa, M. Takahashi, & Y. Aizu, "Monte Carlo simulation of spectral reflectance using a multilayered skin tissue model," Optical review, Vol. 17, pp. 223-229. 2010.

[4] I. V. Meglinski and S. J. Matcher, "Computer simulation of the skin reflectance spectra,"Computer methods and programs in biomedicine, Vol. 70, pp. 179-186, 2003.

[5] T. Binzoni, T. S. Leung, A. H. Gandjbakhche, D. Ruefenacht, and D. T. Delpy, "The use of the Henyey–Greenstein phase function in Monte Carlo simulations in biomedical optics," Physics in Medicine & Biology, Vol. 51, pp. N313, 2006.

[6] L. G. Henyey and J. L. Greenstein, "Diffuse radiation in the galaxy. Astrophysical Journal," Vol. 93, pp. 70-83, 1941.

[7] C. Ash, M. Dubec, K. Donne, & T. Bashford, "Effect of wavelength and beam width on penetration in light-tissue interaction using computational methods," Lasers in medical science, Vol. 32, pp. 1909-1918, 2017.

[8] O. Kim, J. McMurdy, C. Lines, S. Duffy, G. Crawford, and M. Alber, "Reflectance spectrometry of normal and bruised human skins: experiments and modeling. Physiological measurement," Vol. 33, pp. 159-175, 2012.

[9] H. Funamizu, T. Maeda, S. Sasaki, I. Nishidate and Y. Aizu, "Simulation of spectral reflectances in human skin tissue using ray tracing and GPU-based Monte Carlo method," Optical Review, Vol. 21, pp. 359-363, 2014.

[10] V. M. Petnikova, E. V. Tret'yakov and V. V. Shuvalov, "Stability of the Henyey—Greenstein phase function and fast path integration under conditions of multiple light scattering," Quantum Electronics, Vol. 36, pp. 1039, 2006.

[11] I. N. Melnikova, Z. M. Dlugach, T. Nakajima, K. Kawamoto, "Calculation of the reflection function of an optically thick scattering layer for a Henyey–Greenstein phase function". Applied optics, Vol. 39(24), pp. 4195-4204. 2000.

[12] Zhao, G., & Sun, X. "Error analysis of using henyey-greensterin in Monte Carlo radiative transfer simulations," In Progress in Electromagnetics Research Symposium, pp. 1424-1427, 2010.

[13] Petnikova, V. M., Shuvalov, V. V., & Tret'akov, E. V. "Multiple-scattering Henyey-Greenstein phase function and fast path-integration," ICONO 2007: Nonlinear Laser Spectroscopy and High-Precision Measurements; and Fundamentals of Laser Chemistry and Biophotonics, SPIE. Vol. 6727, pp. 311-316, 2007.

[14] N. S. Żołek, S. Wojtkiewicz and A. Liebert, "Correction of anisotropy coefficient in original Henyey Greenstein phase function for Monte Carlo simulations of light transport in tissue," Biocybernetics and Biomedical Engineering, Vol. 28, pp. 59-73, 2008.

[15] A. P. Popov, A. V. Priezzhev, and R. Myllyla, "Effect of spectral width on short laser pulse propagation through upper layers of human skin: Monte Carlo simulations," Proc. SPIE 5319, Laser Interaction with Tissue and Cells XV, (1 July 2004).

[16] V. Tuchin, "Tissue Optics: Light Scattering Methods and Instruments for Medical Diagnosis," SPIE Press, Washington, 2000.

[17] T. L. Troy and S. N. Thennadil, "Optical properties of human skin in the near infrared wavelength range of 1000 to 2200 nm," Journal of biomedical optics, Vol. 6, pp. 167-176, 2001.

[18] M. D. Francisco, W. F. Chen, C. T. Pan, M. C. Lin, Z. H. Wen, C. F. Liao, & Y. L. Shiue, "Competitive real-time near infrared (NIR) vein finder imaging device to improve peripheral subcutaneous vein selection in venipuncture for clinical laboratory testing. Micromachines," Vol. 12, pp. 373-1-21, 2021.

[19] G. Zonios and A. Dimou, "Light scattering spectroscopy of human skin in vivo," Optics Express, 17, 1256-1267, 2009.

[20] S. H. Tseng, P. Bargo, A. Durkin, and N. Kollias, "Chromophore concentrations, absorption and scattering properties of human skin in-vivo," Optics express, Vol. 17, pp. 14599-14617, 2009.

[21] V. Mircheva, E. Borisova, T. Genova, P. Troyanova, L. Avramov and A. Markovski, "Diagnosis of skin lesions through prototype clinical device with diffuse reflectance spectroscopy," Journal of Physics: Conference Series, Vol. 2487, pp. 012026 (1-5), 2023.

[22] P. Hanrahan and W. Krueger, "Reflection from layered surfaces due to subsurface scattering," In Seminal Graphics Papers: Pushing the Boundaries, Vol. 2, pp. 279-288, 2023.

[23] G. R. Ge, J. P. Rolland and K. J. Parker, "Speckle statistics of biological tissues in optical coherence tomography," Biomedical Optics Express, Vol. 12, pp. 4179-4191, 2021.

[24] Y. Zhang, C. Wang, S. Tong and P. Miao, "Separating single-and multiple-scattering components in laser speckle contrast imaging of tissue blood flow," Biomedical Optics Express, Vol. 13, pp. 2881-2895, 2022.

[25] N. N. Boustany, S. A. Boppart, and V. Backman, "Microscopic imaging and spectroscopy with scattered light," Annual review of biomedical engineering, Vol. 12, pp. 285-314, 2010.

[26] S. Zheng and J. Mertz, "Direct characterization of tissue dynamics with laser speckle contrast imaging," Biomedical Optics Express, Vol. 13, pp. 4118-4133, 2022.

[27] N. S. Hanasil, R. K. R. Ibrahim, F. H. Mustafa, F. K. C. Harun, and A. A. Tan, "Evaluation of NIR LED and laser diode as a light source in diffuse reflectance spectroscopy system for intravenous fluid infiltration detection under dermis layer of skin phantom," Measurement, Vol. 223, pp. 113707-1-6, 2023.

[28] M. A. Dall Agnol, R. A. Nicolau, C. J. de Lima, and E. Munin, "Comparative analysis of coherent light action (laser) versus non-coherent light (light-emitting diode) for tissue repair in diabetic rats," Lasers in medical science, Vol. 24, pp. 909-916, 2009.

THIS PAGE IS INTENTIONALLY LEFT BLANK.